UNIVERSITY OF SOUTHAMPTON

FACULTY OF ENGINEERING, SCIENCE AND MATHEMATICS

School of Physics and Astronomy

Non-ideal Exchange Springs in $DyFe_2/YFe_2$ Superlattices

by

Daowei Wang

Thesis for the degree of Doctor of Philosophy

November 2009

UNIVERSITY OF SOUTHAMPTON

ABSTRACT

FACULTY OF ENGINEERING, SCIENCE AND MATHEMATICS
School of Physics and Astronomy

Doctor of Philosophy

NON-IDEAL EXCHANGE SPRINGS IN $DYFE_2/YFE_2$ SUPERLATTICES

by Daowei Wang

Magnetic exchange spring systems have potential applications in (i) the next generation of permanent magnets and (ii) storage elements in information systems. However any practical realization of this potential will involve a study of non-ideal exchange spring behaviour. Within the context of molecular-beam-epitaxy(MBE)-grown $DyFe_2/YFe_2$ superlattices, two non-ideal processes are examined in this work. The first involves the anisotropy of the so-called hard pinning $DyFe_2$ layer. At room temperature, the anisotropy of the Dy pinning ions is reduced substantially, and approaches that of the so-called soft YFe_2 layers, which is usually neglected. In this regime, the magnetic switching process becomes more complicated. The latter has been studied experimentally using the magneto-optic Kerr effect (MOKE), at room temperature. This work was also complimented by 1D computer simulations, involving numerical solution of the Landau-Lifshitz-Gilbert equations. In contrast to the well accepted low-temperature behaviour, both the MOKE and computer simulations show that the anisotropy of the soft YFe_2 layers now plays a significant role in determining the coercive/switching field, even though exchange-springs are formed in the YFe_2 layers. Thus the well established bending field relationship $B_B \propto 1/t_s^2$ found at low temperatures, is not obeyed.

The second non-ideal exchange process studied involved the deliberate insertion of a few hard $DyFe_2$ layers, directly into the middle of the soft YFe_2 layers. This inevitably injects anisotropy into the 'soft' YFe_2 layers, which should give rise to irreversible processes as the exchange springs wind-up and unwind. At low temperatures, irreversible exchange spring processes were observed for fields applied along both the $[00\bar{1}]$ and $[\bar{1}10]$ axes of MBE-grown (110) $DyFe_2/YFe_2$ multilayer samples. For fields applied along the $[00\bar{1}]$, vibrating sample measurements reveal that there are two irreversible exchange processes. The experimental results are complemented by 1D Object Oriented Micromagnetic Framework (OOMMF) simulations. It is shown that deliberate doping of the magnetically soft layers, with one or two hard mono-layers, can modify exchange spring behaviour, substantially. Similar behaviour was observed in a superlattice sample with soft YFe_2 layers doped with $DyFe_2$.

Contents

DECLARATION OF AUTHORSHIP

I, Daowei Wang,

declare that the thesis entitled

Non-ideal Exchange Springs in $DyFe_2/YFe_2$ Superlattices

and the work presented in the thesis are both my own, and have been generated by me as the result of my own original research. I confirm that:

- this work was done wholly or mainly while in candidature for a research degree at this University;
- where any part of this thesis has previously been submitted for a degree or any other qualification at this University or any other institution, this has been clearly stated;
- where I have consulted the published work of others, this is always clearly attributed;
- where I have quoted from the work of others, the source is always given. With the exception of such quotations, this thesis is entirely my own work;
- I have acknowledged all main sources of help;
- where the thesis is based on work done by myself jointly with others, I have made clear exactly what was done by others and what I have contributed myself;
- parts of this work have been published as:
    1. Room temperature magneto optic exchange springs in $DyFe_2/YFe_2$ superlattices, D. Wang, C.G. Morrison, A.R. Buckingham, G.J. Bowden, R.C.C. Ward and P.A.J. de Groot, J. Magn. Magn. Mater. 321, 586 (2009).
    2. Irreversible magnetic exchange-spring processes in antiferromagnetic exchange-coupled bilayer systems, G. Guo, G. Zhang, S. Song, D.W. Wang, G.J. Bowden and P.A.J. de Groot, Appl. Phys. Lett. 93, 102505 (2008).

Signed:
Date:

Acknowledgements

Firstly, I would like to thank my supervisor Prof. Peter de Groot for giving me the opportunity to pursue my PhD in his group. I would also like to thank my advisor Prof. Pavlos Lagoudakis for useful discussions and suggestions. I need to thank Prof. Graham Bowden for his help on micromagnetic simulation and Prof. Alan Fox for his help on x-ray and EDX measurements. I have to thank Jürgen Zimmermann for helping me on OOMMF and related softwares. I am indebted to Sasha Zhukov and Ke Wang for showing me how to use our MOKE setup. I wish to thank Chris Morrison for his help and guidance on transport and VSM measurements, in particular for his stimulating comments during our point contact Andreev reflection measurements. I would like to thank all former and current members of our group, Kevin Martin, Roger Buckingham and Charlotte Hobbs, especially Roger for inspiring questions and discussions. They have made my life at Southampton happier and our group vivid. I would also like to express my gratitude to Denis Torkington and Colin Miles for help on cryogenic liquids and Zondy Webber for training and help in the clean room. I have to thank my colleagues in China, Prof. Jianmin Yuan, Prof. Mingqiu Huang and Prof. Chenglin Tian, for their tireless support and providing me the chance to study in the UK. Financially, I gratefully acknowledge the support from the China and UK Governments, under the Scholarships for Excellence scheme. Finally, I would like to thank my parents Dajian Wang and Güifeng Lu for their understanding and support, in whatever I choose to do.

List of symbols

γ_D	Depolarization constant
P_0	Incident power
η	Efficiency
$\Delta\nu$	Band width
f_L	Laser intensity noise fraction
R	Resistance
T	Temperature
B_B (H_B)	Bending field
t_s (t_h)	Soft (hard) layer thickness
M_s (M_h)	Soft (hard) magnetization
A_s (A_h)	Soft (hard) exchange constant
K_s (K_h)	Soft (hard) anisotropy constant
A_i	Interface exchange constant
δ_s (δ_h)	Soft (hard) domain wall width
H_N (B_N)	Nucleation field
H_C (B_C)	Coercivity
M_r	Remanence magnetization
$\tilde{K}_4$, $\tilde{K}_6$, $\tilde{K}_8$	Multipolar anisotropy constants
α_x, α_y, α_z	Direction cosines
γ	Gyromagnetic ratio
T_1 (T_2)	Longitudinal (transverse) relaxation time
α	Damping constant
$\mathbf{m}$	Normalized magnetization vector

I	Light intensity
E_p (E_s)	P (s) electric component
θ_K (ϵ_K)	Kerr rotation angle (ellipticity)
δ	Analyzer angle
$\bar{I}$ (ΔI)	Average (difference) of I
λ	Wave length
$\mathbf{q}$	Magneto optical constant
A (P)	Boundary (propagation) matrix
F	Gibbs free energy density
G	Sensitivity function

Chapter 1

Introduction and background

The concept of ferromagnetic (FM) exchange-spring magnet was first proposed to increase the energy product $(BH)_{max}$, the figure of merit, of a permanent magnet. Later, it was found that exchange-spring magnets could also provide a potential solution to the superparamagnetic limit problem in information technology. Here, molecular beam epitaxy (MBE) grown antiferromagnetically (AFM) coupled $DyFe_2/YFe_2$ bilayers are used to examine non-ideal characteristics in exchange-spring systems. Material parameters, needed to interpret the experimental data, are also given in this chapter. Finally, magnetization dynamics and domain walls are discussed, briefly, to facilitate the understanding about the exchange-spring formation process.

1.1 Introduction of exchange-spring systems

Before the era of high-density information technology, the most important application of magnetic materials centred on their ability to store energy as permanent magnets. Conventionally they have found applications in motors, generators and actuators. Later, following the development of computers, magnetic storage in the form of hard magnetic disks, has become of paramount importance. However, common to all applications, the energy product $(BH)_{max}$ is still used as the figure of merit. This is illustrated schematically in Fig. 1.1, which shows a B-H loop for an ideal uniaxial magnet. Hence the product BH is a maximum at the coercivity H_c, as in the case shown in Fig. 1.1. For this statement to be true, we have assumed that the coercivity is less than half of the remanent magnetization value ($H_c < M_r/2$).

There are two ways to increase the energy product: One is to increase the coercivity, and the other is to increase the remanence magnetization at the coercivity, B_c. Due to the strong exchange interaction in 3d transition metals and high density of magnetic ions, the magnetization value is very high. But transition metals are usually

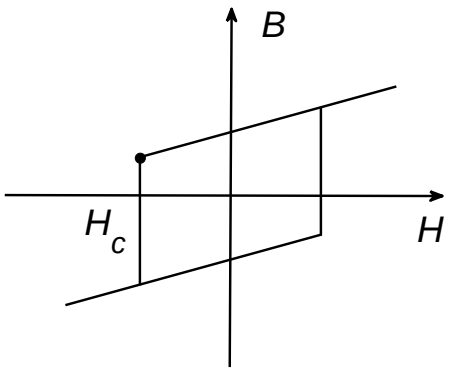

Figure 1.1: Definition of the energy product, $(BH)_{max}$. The black dot shows schematically where $(BH)_{max}$ is achieved. An ideal easy-axis hysteresis loop with uniaxial anisotropy is assumed.

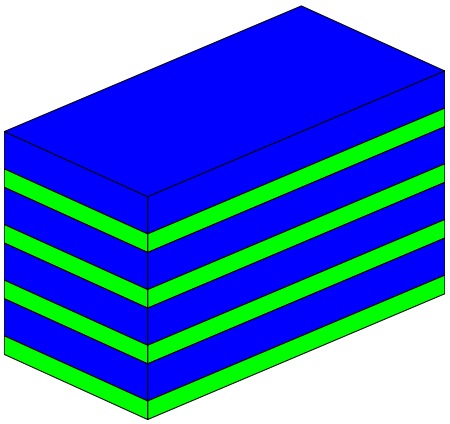

Figure 1.2: The multilayer structure used to optimize the energy product. The hard layers are colored in green and the soft layers in blue.

characterized by negligible coercivity. On the other hand, the coercivity of rare-earth transition-metal (RE-TM) intermetallic compounds is very high, due to the strong crystal field at the rare-earth sites. However, their magnetization values tend to be smaller than, say, Fe, due to (i) the cancelation between the orbit and the spin moments for the first half of the 4f series and (ii) the AFM coupling between the rare-earth elements and the transition metals for the second half. To overcome this dilemma, the concept of exchange spring was put forward [1]: Here, one can hope to utilize the high magnetization of transition metals and the high coercivity of RE-TM intermetallic compounds by forming a exchange-coupled, alternating, hard/soft composite planar structure, as shown in Fig. 1.2.

For FM exchange coupling, the moments of both the hard and the soft layers are parallel at remanence. But an applied negative field will create deviation from the perfect aligned state in the soft phase first. In general, the hard phase will pin the soft layer through exchange coupling, thus increasing the coercivity. The natural result of this gradual rotation of the soft magnetization, i.e. the setup of an exchange spring (see Fig. 1.3) in the soft phase, will result in a decrease in energy product, due to the reduction in remanent magnetization. The field corresponding to the first appearance of exchange springs is defined as the bending field, B_B. Mathematically, for an ideal, uniaxial exchange spring ferromagnet, B_B corresponds to the transition field from uniform to nonuniform spin configurations. This transition can be determined unambiguously by inspecting the susceptibility $\chi = dM/dH$, where H is the applied

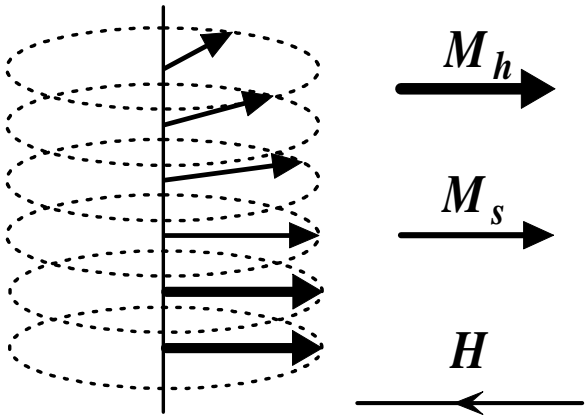

Figure 1.3: Illustration of an exchange spring configuration in an FM coupled hard/soft magnetic bilayer structure. The thicker and the thinner arrows represent the hard and the soft magnetic moments, respectively. H is the applied, negative magnetic field.

magnetic field and M is the magnetization component along H. If the distribution of magnetization remains uniform, $\chi = 0$. B_B is given by the field value where non-zero susceptibility $\chi \neq 0$ first appears [1]. Of course, except for infinitely large anisotropy for the hard phase, there is also deviation from perfect alignment in the hard phase. But usually it is very small, so can be neglected. This picture of exchange-spring formation is only valid if the thickness of the soft phase, t_s, is greater than the domain wall (see Section 1.5) width of the hard phase $\delta_h = \pi\sqrt{A_h/K_h}$, $t_s > \delta_h$, where A_h and K_h are the exchange coupling and uniaxial anisotropy constants, respectively [3, 4, 5]. When $t_s < \delta_h$, the whole system acts as an exchange-coupled rigid magnet, and switches at the nucleation field H_N. If there is no other pinning centers present, the coercivity H_c can be approximated as H_N. This configuration is suitable for the aim of maximizing the energy product, because there is no reduction of magnetization caused by the setup of exchange springs for fields up to the nucleation field. Theoretically, an energy product as high as 1 MJ/m^3 has been predicted for a $Sm_2Fe_{17}N_3/Fe_{65}Co_{35}$ superlattice with $t_h =$ 2.4 nm and $t_s = 9.0$ nm [3, 4], using an analytical model similar to that given in Chapter 3. An even higher $(BH)_{max}$ of 1.09 MJ/m^3 [3, 4] is predicted for a uniform distribution of $Fe_{65}Co_{35}$ spherical nano-particles embedded in the hard $Sm_2Fe_{17}N_3$ matrix.

To obtain this result, perturbation theory has been employed. In this approach, the diameter of the spheres has to be less than $\sim \delta_h$, which is about 3 nm for $Sm_2Fe_{17}N_3$, to guarantee the simultaneous nucleation of the two phases. If this condition is satisfied, perturbation theory gives the remanent magnetization as [3]

$$M_r = f_h M_h + f_s M_s, \tag{1.1}$$

[1] Practically, due to the roundup of magnetic hysteresis loops, the method used by Beaujour [2] is employed to determine the experimental bending field.

where f_h and $f_s = 1 - f_h$ are the volume fractions of the hard and the soft phases, respectively. The predicted nucleation field, within the Stoner-Wolhfarth model, is given by [3]

$$\mu_0 H_N = 2\frac{t_h K_h + t_s K_s}{t_h M_h + t_s M_s}. \tag{1.2}$$

The resulted hysteresis loop for this configuration is square, with remanence M_r and coercivity $H_c = H_N$. The product

$$BH = \mu_0 H(M_r - H) = -\mu_0(H - M_r/2)^2 + \mu_0 M_r^2/4. \tag{1.3}$$

From the corresponding parabola curve, we can see the energy product $(BH)_{max}$ is given by $M_r^2/4$ if $H_N > M_r/2$. If $H_N < M_r/2$, then

$$BH = H(M_r - H) \leq H_N(M_r - H_N) \leq \mu_0 H_N M_r/2 = (BH)_{max}. \tag{1.4}$$

The maximum of $(BH)_{max}$ is given by the condition $H_N = M_r/2$, which can be simplified to

$$\frac{\mu_0 M_s^2}{4K_h}\left(1 - \frac{M_s - M_h}{M_s} f_h\right)^2 = f_h \tag{1.5}$$

for an ideally soft phase ($K_s = 0$). Assuming the fraction volume of the hard phase and the ratio $(M_s - M_h)/M_s$ are small, in first order approximation the solution is very simple [3],

$$f_h = \frac{\mu_0 M_s^2}{4K_h}. \tag{1.6}$$

Substituting in the relevant parameters for the soft and hard phases, the above given optimal energy product can be obtained. The Sm content in this case is only about 5% in weight. However, the implementation of such a structure may be difficult in practice. It is worth noting that the theoretical limit for the energy product is $\mu_0 M_s^2/4$, which is 1.10 MJ/m^3 for $Fe_{65}Co_{35}$ [3, 4]. From this limit, we can see the effectiveness of the concept of exchange-spring magnets on increasing the energy product. The micromagnetic approach used for the above discussion does not take account of thermal fluctuations of the free energy. In real applications, thermal stability is a very important issue, if the permanent magnet is mostly composed of the soft phase. Fortunately, the optimal value of the energy product is not very sensitive to the fraction volume of the hard phase, due to the small value $(M_s - M_h)/M_s \sim 0.28$ [3]. So the thermal stability can be improved by increasing the fraction volume of the hard phase, without reducing the energy product too much.

1.2 AFM exchange spring systems

For obvious reasons, AFM exchange spring systems can not be used to increase the energy product. However, computer simulations show that besides applications as permanent magnets with an energy product approaching its theoretical limit, exchange-spring magnets can also be used as information storage elements in hard disks [6, 7, 8, 9, 10]. The problem confronting the information storage industry is the reduced thermal stability of the storage elements, as the size of a bit is reduced. One way out is to use hard magnetic materials to stabilize the information elements. This method is based on the simple fact that the thermal stability of an uniaxial, single domain particle depends on the energy barrier in a simple exponential fashion,

$$\tau \propto e^{KV/k_BT}. \tag{1.7}$$

Here τ is the magnetization decay lifetime constant of a magnetic information storage element of volume V and anisotropy constant K. T is the temperature and k_B is the Boltzmann constant. But the consequence of an increased anisotropy is a higher write field. So in order to circumvent this awkward situation, exchange-spring systems have been suggested. An exchange-spring magnet can have both thermal stability and small write field: the thermal stability is derived from the hard phase, while the small write field can be provided by the setup of exchange springs in the soft phase, which help to switch the hard phase via the exchange coupling. For this to occur, it is obvious that the thickness of the soft phase should be larger than the hard phase domain wall width, $t_s > \delta_h$, to avoid the exchange-coupled rigid magnet regime. The reason behind the fact that the thermal stability and the write field are determined by individual phases in a composite structure lies on the difference between thermal fluctuations and applied magnetic field. Basically, the thermal stability is determined by the hard phase with a very high energy barrier. If there is only a single, hard phase, the corresponding coercivity (write field) is also very large. By introducing an exchange-coupled soft phase to the hard phase, exchange springs can set up. As a result of exchange spring formation in the soft phase, the coercivity can be reduced significantly [6]. Hence the superparamagnetic limit problem can be circumvented. This warrants the study on exchange spring systems from the application point of view. From the point of a thorough understanding of exchange spring physics, which is needed before any serious applications, a well defined sample structure and known material properties are needed. Due to the single crystal structure of our MBE-grown AFM superlattices and the extensively studied material parameters, they are an ideal model system for studying exchange spring characteristics.

AFM exchange-spring $DyFe_2/YFe_2$ samples were grown at Oxford University by

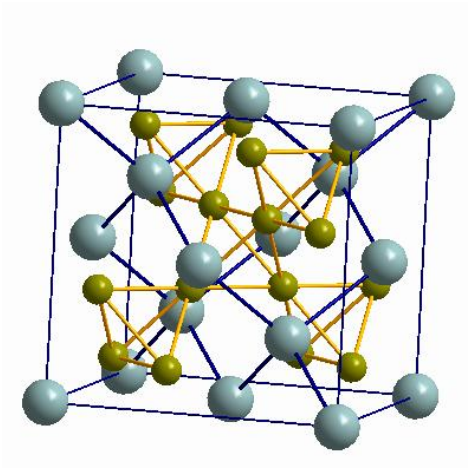

Figure 1.4: The C15 cubic Laves phase structure [11]. The large and the small spheres denote Mg and Cu like atoms, respectively.

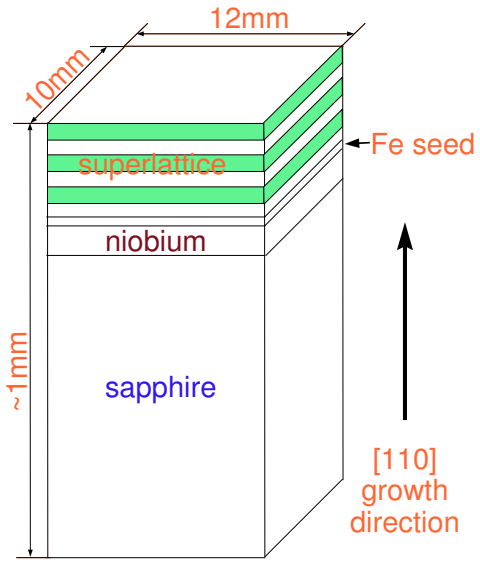

Figure 1.5: Schematic for the epitaxial growth of $DyFe_2/YFe_2$ superlattices.

MBE [11]. The crystal structure of both $DyFe_2$ and YFe_2 is the C15 cubic Laves phase structure [12, 13], shown in Fig. 1.4. Its prototype is $MgCu_2$ and it belongs to the space group $Fd\bar{3}m$. The cubic Laves phase structure is often found in many ideal AB_2 intermetallics, mainly because of its close analogy to the close packed structure in crystals. It can be regarded as tetrahedrally close packed structures from atoms A and B with ideal ratio of the radii, $r_A/r_B = \sqrt{3/2}$. The lattice mismatch between $DyFe_2$ and YFe_2 is only $(a_{YFe_2} - a_{DyFe_2})/a_{YFe_2} = 0.5\%$, so the epitaxial growth is very good. In the fabrication process, a layer of Nb, $\sim$ 1000 Å, is first deposited on the sapphire substrate, facilitating the epitaxial relation between bcc Nb and hexagonal Al_2O_3 [14]. Then a thin layer of Fe, $\sim$ 30 Å, is deposited on top of the Nb buffer layer to promote the formation of the cubic Laves phase. Subsequently, the multilayers are deposited on top of the Fe seed layer, with alternating $DyFe_2$ and YFe_2 layers. The top layer is usually YFe_2 for a multilayer sample. To prevent oxidation, usually a thin layer of Y, $\sim$ 100 Å, is deposited on top of the whole structure. A schematic view of this structure can be seen in Fig. 1.5. The epitaxial relationships between the Laves phase and sapphire substrate are [110] Laves//[11$\bar{2}$0] sapphire, [1$\bar{1}$1] Laves//[0001] sapphire and [$\bar{1}$12] Laves//[1$\bar{1}$00] sapphire [15].

The magnetic properties of RE-TM compounds have been studied extensively [13]. In the RE-TM compounds, the magnetic coupling depends on the atomic number of the RE element: for light rare-earth elements, for example Sm, it is FM; while for heavy rare-earth elements, such as Er, the magnetic moments of rare-earth and

transition-metal atoms are AFM coupled. For the $DyFe_2$ system, the exchange interaction between Dy and Fe is AFM ($\sim$ 100 K [16, 17]) while the Fe-Fe pair has FM exchange coupling, $\sim$ 600 K. The exchange interaction between rare-earth moments is very small, well below $\sim$ 100 K [13]. In $DyFe_2/YFe_2$ multilayers, the effective exchange coupling between $DyFe_2$ and YFe_2 layers is AFM. Crystal field interactions give rise to strong anisotropy at the rare earth sites, hence $DyFe_2$ is magnetically hard and YFe_2 is magnetically soft.

As a result of the AFM effective coupling between alternating layers, we can manipulate the magnetic properties of superlattices by changing the thickness of the hard and soft layers. Both the magnetization and the nucleation field of multilayers depend on the thicknesses, so by choosing suitable values for the thicknesses of $DyFe_2$ and YFe_2, we can make the net magnetization zero, thus an artificial antiferromagnet can be produced. In addition, the coercivity of the superlattices can be changed by varying the relative thicknesses of the hard and soft layers [18].

A more interesting feature in the $DyFe_2/YFe_2$ system is the formation of exchange springs in the soft YFe_2 dominated superlattices. When the applied field exceeds the bending field B_B, exchange springs will be generated in the soft YFe_2 layers, in order to minimize the Zeeman energy, but at the cost of Fe-Fe exchange energy. This process is reversible until the applied field goes to the still higher nucleation field B_N, when the hard and the soft layers switch irreversibly.

In the YFe_2 dominated 1:4 $DyFe_2/YFe_2$ superlattices, when the thickness of hard layer is greater than 45 Å the coercivity for the whole system is negative because of the exchange spring formation. While for thickness less than 45 Å, the nucleation field is very large, $B_N > 12$ T [19], and the whole system acts as a rigid magnet.

The exchange spring formed in hard and soft layers is very similar to a domain wall. When a current flows in this system, there will arise a giant magneto-resistance (GMR) effect [20], which can be viewed as a direct consequence of the regular oscillating spin arrangement in exchange spring superlattices. The mistracking of electrons traversing those exchange springs gives rise to the domain wall GMR [21].

1.3 Crystalline anisotropy

Anisotropy in magnetic materials means that the direction of magnetization tends to align along a preferred direction, or equivalent directions. There are at least two prerequisites for the existence of anisotropic behaviour in magnetic materials: crystal field interaction and spin-orbit interaction. The crystal field interaction arises from the Coulomb interaction between the magnetic ion and all the other ions composing the

crystal lattice. The symmetry of the crystal field interaction is basically determined by the symmetry of the crystal field and the wave function of the ion considered, which is a consequence of the fact that the Coulomb interaction is spherically symmetric. If the wave function is spherically symmetric, then the crystal field interaction is also spherically symmetric: there is no anisotropy. The appearance of anisotropy requires the wave function not to be spherically symmetric, i.e., the magnetic ion should not be in S-state. In this case, the electron density, which is proportional to the modulus of the wave function, is not evenly distributed over the 4π solid angle spanned around the ion: the electron density is higher along some directions. This gives rise to anisotropy and the energy of the magnetic ion depends on its orientation. However, this anisotropy is only effective for the orbital degree of freedom. For it to be effective also for the spin degree of freedom of the electrons, spin-orbit interaction has to be considered. With the spin-orbit interaction, the two degrees of freedom are coupled, hence the anisotropy now is effectively for spin, or equivalently, for the magnetization of ferromagnetic materials.

The fact that the anisotropy in magnetic materials is determined by the crystal field and spin-orbit interactions determines there are two cases to consider: (1) the crystal field interaction is dominant and (2) the spin-orbit interaction is dominant. In case (1), the spin-orbit interaction is treated perturbatively and the wave function is an eigenfunction of the orbital angular momentum operator, which commutes with the crystal field Hamiltonian. The crystal field interaction is essentially an electrostatic interaction and can be described by a real potential. Any real valued function can only have imaginary values for the orbital angular momentum. To satisfy the hermitian property of the orbital angular momentum operator, the value of the angular momentum has to be zero. This is termed as the orbital angular momentum quenching. Of course, this is a first order perturbation result, and second order perturbation will give a small value for the orbital angular momentum, i.e. the quenching is not complete. The quenching of the orbital momentum gives rise to an almost isotropic energy profile, so the anisotropy cannot be very large. Generally, this applies to 3d transition metal ions. In contrast, in case (2), the spin-orbit interaction is dominant over the crystal field effect, and the crystal field interaction is viewed as a perturbation: the orbital and spin angular momenta couple first to form a total momentum. The derived anisotropy can be large, if the crystal field is strong enough. The rare earth ions belong to this case.

Phenomenologically, the anisotropy can be described by an energy density functional, which is dependent on the direction of the magnetization vector. Usually, the anisotropy energy density is expressed as a power series in the direction cosines of the magnetization vector. For cubic materials, appropriate to our system, the anisotropy

density takes the form [22]

$$E_c = K_1\left(\alpha_x^2\alpha_y^2 + \alpha_y^2\alpha_z^2 + \alpha_z^2\alpha_x^2\right) + K_2\alpha_x^2\alpha_y^2\alpha_z^2 + K_3\left(\alpha_x^4\alpha_y^4 + \alpha_y^4\alpha_z^4 + \alpha_z^4\alpha_x^4\right), \quad (1.8)$$

where α_x, α_y and α_z are the direction cosines with respect to the three major axes of the cubic Laves crystal lattice, [100], [010] and [001]. Here only terms to 3rd order are included and higher terms are neglected.

The anisotropy coefficients, K_1, K_2 and K_3, are functions of temperature. Usually, the temperature dependence can be calculated on the basis of perturbation theory. For 3d transition metals, the calculation is very difficult, due to the presence of energy bands rather than discreet energy levels, arising from their extended 3d wave functions. In 4f metals, due to the shielding by the 5d and 6s electrons from the crystal field, the crystal field interaction between the localized 4f electrons and the crystal lattice is weaker than in 3d metals. The crystal field then can be treated as a perturbation. The starting point is the Hamiltonian of a rare-earth ion [22]

$$H = H_{ex} + H_{cf}, \quad (1.9)$$

with H_{ex} and H_{cf} denoting the exchange and crystal field Hamiltonian, respectively. Using this Hamiltonian, Martin *et al* [22] give the temperature dependence of the anisotropy coefficients to second order in the crystal field interaction, updating the values given in [23]. Their calculation only includes the single-ion contribution to the anisotropy, discarding the small double-ion exchange anisotropy. The final result is the expression for the anisotropy coefficients [22]

$$\begin{aligned} K_1 &= -\frac{15}{2\sqrt{\pi}}\tilde{K}_4 - \frac{21}{4}\sqrt{\frac{13}{\pi}}\tilde{K}_6 - 9\sqrt{\frac{17}{\pi}}\tilde{K}_8, \\ K_2 &= \frac{231}{4}\sqrt{\frac{13}{\pi}}\tilde{K}_6 + 9\sqrt{\frac{17}{\pi}}\tilde{K}_8, \\ K_3 &= \frac{65}{2}\sqrt{\frac{17}{\pi}}\tilde{K}_8, \end{aligned} \quad (1.10)$$

where the multipolar anisotropy coefficients $\tilde{K}_i$ are given in the table of Appendix A. These are the values used in our simulations.

Due to the [110] growth of our thin films on sapphire, the crystallographic coordinate used to derive K_i is different to the film coordinate used in experimental measurements. The x, y and z axes of the film system correspond to $[00\bar{1}]$, $[\bar{1}10]$ and [110] crystallographic directions, respectively. The transformation from the film system (f) to the crystallographic system (c) can be realized by an orthogonal matrix through

$$\begin{pmatrix} x \\ y \\ z \end{pmatrix}_c = \begin{pmatrix} 0 & -1/\sqrt{2} & 1/\sqrt{2} \\ 0 & 1/\sqrt{2} & 1/\sqrt{2} \\ -1 & 0 & 0 \end{pmatrix} \begin{pmatrix} x \\ y \\ z \end{pmatrix}_f . \quad (1.11)$$

On substituting (1.11) into (1.8), we obtain the expression for the anisotropy density in the (110) film system [24]

$$\begin{aligned} E_c &= K_1\left(\frac{(\alpha_y^2-\alpha_z^2)^2}{4}+\alpha_x^2(\alpha_y^2+\alpha_z^2)\right)+\frac{K_2}{4}\alpha_x^2(\alpha_y^2-\alpha_z^2)^2 \\ &+ K_3\left(\frac{(\alpha_y^2-\alpha_z^2)^4}{16}+\frac{\alpha_x^4}{2}(\alpha_y^4+\alpha_z^4+6\alpha_y^2\alpha_z^2)\right). \end{aligned} \tag{1.12}$$

This is the actual form of the crystalline anisotropy used in the expression for the total energy density in computer simulation.

In addition to the crystal field contribution discussed above, the magneto-elastic interaction contributes to the anisotropy, too. As shown in [25], the main origin of the strain in epitaxial $REFe_2$ thin films is due to the differential thermal contraction between the film and the substrate, on cooling down from the deposition temperature to room temperature. The resulted magneto-elastic Hamiltonian is [26]

$$H_e = b_2\epsilon_{xy}\alpha_x\alpha_y, \tag{1.13}$$

where b_2 is the temperature dependent magneto-elastic constant, $\epsilon_{xy}\sim -0.55\%$ [25] is the shear strain at room temperature and α_x and α_y are the direction cosines in the crystallographic system. The temperature dependence of ϵ_{xy} is not taken into account in this approach. To second order, the magneto-elastic contribution to the anisotropy has been calculated by Bowden *et al* [26], giving

$$E_e = \sqrt{\frac{15}{2\pi}}(\tilde{K}_2+\tilde{K}_{242})\alpha_x\alpha_y \tag{1.14}$$

with $\tilde{K}_2$ and $\tilde{K}_{242}$ the first and second order anisotropy coefficients. Performing the same transformation as we did for the crystal field anisotropy in (1.11), we get the magneto-elastic anisotropy in the film system [24]

$$E_e = \frac{1}{2}\sqrt{\frac{15}{2\pi}}(\tilde{K}_2+\tilde{K}_{242})(\alpha_z^2-\alpha_y^2). \tag{1.15}$$

The magneto-elastic anisotropy, or the strain term, is responsible for the transition of the in-plane easy axis $[00\bar{1}]$ at low temperature to $[\bar{1}10]$ at room temperature [27, 28]. In our simulations, a factor of 2.5 will be multiplied to the expression shown in (1.15), to accommodate the $\sim 14^\circ$ out-of-plane angle for the magnetization [29] as measured by a vector vibrating sample magnetometer [30].

1.4 Demagnetization dynamics

Neglecting the orbital degree of freedom, magnetization dynamics are identical to spin dynamics. For an isolated ensemble of spins, the magnetization vector will rotate

steadily around the applied field at an angle determined by the initial angle between the field and the magnetization vector. To align the magnetization to the direction of the applied field, relaxation is needed. This kind of relaxation usually is provided by the spin-lattice interaction. Microscopically, the relaxation process of magnetization is governed by the Bloch equations [31]

$$\begin{aligned} \frac{dM_\perp}{dt} &= -\gamma(\mathbf{M}\times\mathbf{B})_\perp - \frac{M_\perp}{T_2}, \\ \frac{dM_\parallel}{dt} &= -\gamma(\mathbf{M}\times\mathbf{B})_\parallel + \frac{M_s - M_\parallel}{T_1} \end{aligned} \tag{1.16}$$

for the perpendicular ($M_\perp$) and parallel ($M_\parallel$) components of the magnetization ($\mathbf{M}$) with respect to the total field $\mathbf{B}$. γ is the gyromagnetic ratio, M_s is the saturation magnetization, and T_1 and T_2 are the spin-lattice (longitudinal) and spin-spin (transverse) relaxation times, respectively. For free electrons, $\gamma = 1.8\times10^{11}$ Hz/T. Because the perpendicular relaxation usually finishes before the longitudinal relaxation, the spin-spin relaxation time should necessarily be less than the spin-lattice relaxation time, $T_2 \leq T_1$. The Bloch equations correctly describe the dynamics of a single spin, or an ensemble of isolated spins, in equilibrium at finite temperature through the temperature dependent T_j. The field here is only the externally applied magnetic field. Microscopically including the anisotropic, magneto-static, exchange and magneto-elastic interactions is very difficult. Further complications arise from the distribution of parameters, such as γ and T_j in addition to M_s, for a macroscopic sample.

Phenomenologically, some of those effects are taken into account by the Landau-Lifshitz-Gilbert (LLG) equation [31]

$$\frac{d\mathbf{m}}{dt} = -\gamma\mathbf{m}\times\mathbf{B} + \alpha\mathbf{m}\times\frac{d\mathbf{m}}{dt} \tag{1.17}$$

with $\mathbf{m} = \mathbf{M}/M_s$, the normalized magnetization vector. Here (i) $\mathbf{B}$ is the effective field obtainable from the functional derivative of the energy density functional E ($\mathbf{B} = -\partial E/\partial\mathbf{M}$) and (ii) α is the Gilbert damping constant. This equation of motion for $\mathbf{M}$ conserves the magnitude of $\mathbf{M}$, $\mathbf{m}^2 = 1$ independent of time. Multiplying (1.17) by $\mathbf{m}\times$, we find

$$\mathbf{m}\times\frac{d\mathbf{m}}{dt} = -\gamma\mathbf{m}\times(\mathbf{m}\times\mathbf{B}) - \alpha\frac{d\mathbf{m}}{dt} \tag{1.18}$$

where the fact $\mathbf{m}\cdot d\mathbf{m}/dt = 0$, which is a natural result of $\mathbf{m}^2 = 1$, is used. Multiplying α to (1.18) and substituting (1.17) in again, we obtain an explicit form for the time evolution

$$\frac{d\mathbf{m}}{dt} = -\gamma'\left(\mathbf{m}\times\mathbf{B} + \alpha\mathbf{m}\times(\mathbf{m}\times\mathbf{B})\right) \tag{1.19}$$

with the renormalized gyromagnetic ratio $\gamma' = \gamma/(1+\alpha^2)$. This is the form originally put forward by Landau and Lifshitz, and we will use this explicit form in simulation.

Considering the case of uniform magnetization or a single spin, $\mathbf{M}(r,t) \rightarrow \mathbf{M}(t)$, under the influence of a uniform field along z-axis, $\mathbf{B} = B\hat{z}$. Expanding (1.19) explicitly, we have three coupled equations [31]

$$\begin{aligned} \frac{dm_x}{dt'} &= m_y + \alpha m_x m_z, \\ \frac{dm_y}{dt'} &= -m_x + \alpha m_y m_z, \\ \frac{dm_z}{dt'} &= -\alpha(1 - m_z^2) \end{aligned} \tag{1.20}$$

with a dimensionless time variable $t' = -\gamma' B t$. The third equation has been simplified using $m^2 = 1$. Supposing $\mathbf{m}$ takes the following form [31]

$$m_x = e^{it'} \sin\theta, m_y = ie^{it'} \sin\theta, m_z = \cos\theta$$

with the real parts representing the physical components, then (1.20) reduces to [31]

$$\frac{d\theta}{dt'} = \alpha \sin\theta. \tag{1.21}$$

θ is the angle between $\hat{z}$ and $\mathbf{m}$. A direct integration gives [31]

$$\tan\frac{\theta}{2} = ce^{\alpha t'} = \tan\frac{\theta_0}{2} e^{\alpha t'}. \tag{1.22}$$

The integration constant c is determined by the initial angle $\theta(0) = \theta_0$. Fig. 1.6 shows the time evolution as given by the above solution to the LLG equation. This analytical solution will be used in Chapter 4 to check the validity of the Runge-Kutta method used in the numerical integration. Note that although various fields are included already, the LLG equation applies only to zero temperature, simply because the temperature dependence and the distribution within the sample of M_s and parameters, such as γ and α, are not included. The inclusion of those quantities could result in smoothing of demagnetization curves, at finite temperatures. Such temperature effects can be included by adding a random field, on the basis of the fluctuation-dissipation theorem [32], if we do not want to use position dependent quantities. Applications of the fluctuation-dissipation theorem in the context of magnetic properties have generated many meaningful results, such as thermally assisted reversal [33], current induced noise and damping [34] and creep of current-driven domain-wall lines [35], all starting from the seminal work of Brown [36] and extended by García-Palacios *et al* [37]. This approach is beyond the scope of the current work. Here we just simply use a higher temperature value of those temperature dependent parameters, as compared to the actual experimental temperature at which the measurement is made, to imitate the finite temperature effect, as done by Zimmermann *et al* [38].

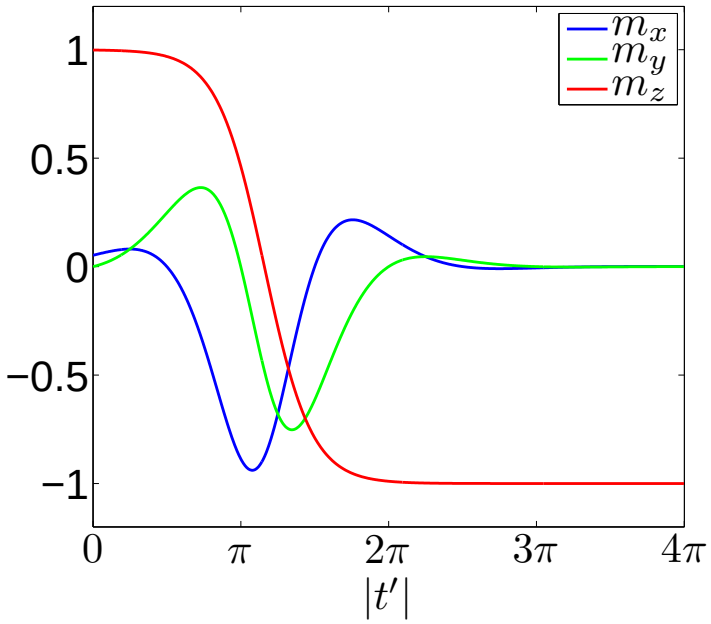

Figure 1.6: Time evolution of the magnetization according to the LLG equation for field applied along the negative z-axis. The dimensionless time t' is actually the relative phase. $\alpha = 1$ and $\theta_0 = \pi/60$ are used to generate those curves.

We have used two methods to simulate the magnetic response of our samples, though they are both based on the LLG equation. One is to solve the LLG equation using the Runge-Kutta method. The advantage of this route is that we can also simulate the measured magneto optic Kerr effect (MOKE) signal. The other uses the micromagnetic simulation package, OOMMF, which was developed at NIST [39]. The OOMMF realization for our samples utilizes the specially designed cubic anisotropy package [24]. To reduce the simulation time needed, we consider only a unit cell in the film plane, as a representative of the average magnetization in the film plane. By doing so, the whole sample is represented as a chain of exchange coupled spins, and the model is one dimensional (1D). Due to the three dimensional (3D) characteristics of the magnetostatic interaction, it is not included in this idealization. Collinear configuration of the hard and soft phases, both parallel to an in-plane principal axis, is taken as the initial state, with the applied field direction almost parallel to the magnetization direction. Then the final state of the current step of field evolution will be used as the initial state for the next step, iteratively. If the magnetization and the applied field are completely parallel, the direction of the magnetization remains constant during the field sweep. To implement the field evolution in OOMMF simulations, two 5 mT fields are applied along the two orthogonal axes perpendicular to the applied field. In the MOKE simulations, the field is applied at a small angle, 0.01 radians, with respect to the easy axis. The unit cell size used in the OOMMF simulation is 1 nm $\times$ 1 nm $\times$ 1 nm, which

is small enough to resolve detailed magnetic structures for an exchange length of 3.4 nm [24]. To facilitate a very fast convergence to an equilibrium for the spin dynamic evolution, $\alpha = 0.5$ will be used in the OOMMF simulation. The exchange coupling constants are chosen to be $A_s = A_h = -A_i = 1.46 \times 10^{-11}$ J/m. This value is obtained from the exchange constant of Fe by scaling down from Fe's Curie temperature. The minus sign in front of the interface exchange coupling constant A_i guarantees the AFM coupling between the layers of $DyFe_2$ and YFe_2.

1.5 Domain wall thickness and energy

Magneto-static interaction refers to the dipolar interaction between magnetic moments. Confined to a small volume, the magneto-static interaction is weak, as compared to exchange or crystal field interaction. But it is of long range, while crystal field interaction is local and exchange interaction can extend only to a few lattice constants. So for a macroscopic sample, magneto-static interaction has to be considered. The most significant consequence of the magneto-static interaction is the formation of domains, in an otherwise uniformly magnetized crystal. This can be viewed as a realization of the principle of pole exclusion: there would be effective surface magnetic poles according to Maxwell's equations if the sample is uniformly magnetized, hence increasing the associated magneto-static energy. This appearance of surface poles can be avoided by dividing the sample into several uniformly magnetized domains, each with its own magnetization direction. Those domains form a flux closure pattern, thus reducing the accompanied magneto-static energy. Domain walls separate the uniform domains by rotating spins from one direction to another. Due to the similar gradual rotation of magnetization direction in a exchange spring, the knowledge of domain walls helps the analysis of exchange springs and provides insight into the physics. As we will see later, formation of domain walls can affect the switching modes of exchange springs.

We will use a Bloch wall in a ferromagnet as an example to illustrate the various interactions involved in the determination of the thickness of the wall and its energy, accepting the existence of domains as a fact. The basic geometry is shown in Fig. 1.7: we have two domains with magnetization antiparallel to each other, and in between them is there a 180° Bloch wall. In this 1D model, the exchange interaction between two adjacent spins takes the form

$$E_i = -A \cos \theta_{ij} \sim \frac{A}{2} \theta_{ij}^2 \tag{1.23}$$

with $A > 0$ the exchange coupling constant and θ_{ij} the angle between the two spins. The first equation is exact and the second expression is only valid for small θ_{ij}, dropping

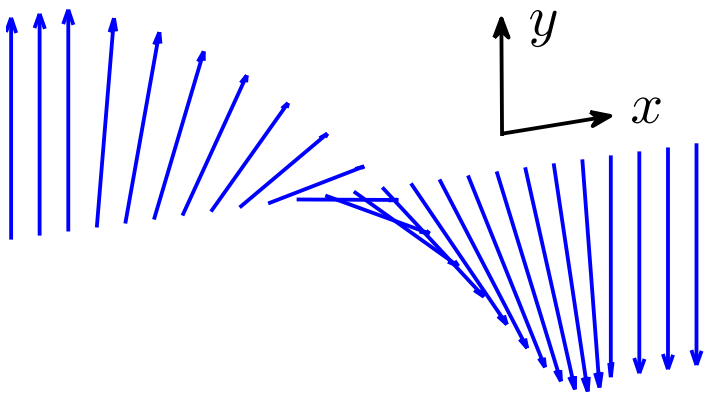

Figure 1.7: Schematic drawing for a 180° domain wall bwtween two domains. The arrows represent the magnetization vectors.

an irrelevant constant (1) in the Taylor expansion for $\cos\theta$. The FM exchange favors parallel spin configuration and tends to increase the wall thickness. Anisotropy limits the wall thickness to a finite value. For simplicity, a uniaxial anisotropy will be used

$$E_a = K \sin\theta^2, \tag{1.24}$$

where $K > 0$ is the first anisotropy constant and θ is the angle formed by the magnetization with respect to the easy axis, which is parallel to the magnetization direction in the left domain. Any deviation of the magnetization direction from the easy axis will result in an energy cost. Suppose we have N spins in the domain wall, then $\theta_{ij} = \pi/N$ and $\theta_j = j\pi/N$. The total energy of the wall is the sum of the exchange and anisotropic energies

$$\begin{aligned} E &= Na\frac{A}{2}\left(\frac{\pi}{N}\right)^2 + Ka^3\sum_j \sin\theta_j^2 = a\left(\frac{A}{2}\frac{\pi^2}{N} + Ka^2\frac{N}{\pi}\int_0^\pi \sin\theta^2 d\theta\right) \\ &= \frac{a}{2}\left(\frac{A\pi^2}{N} + Ka^2N\right), \end{aligned} \tag{1.25}$$

where a is the lattice constant of a cubic crystal. On arriving at the third equation, we have changed the sum to an integral using the relation $d\theta/dx = \pi/Na$, valid for $N \to \infty$. Minimization of the total energy gives the length of the domain wall

$$\delta_w = Na = \pi\sqrt{\frac{A}{K}}. \tag{1.26}$$

Putting the corresponding value for N back into the total energy expression, the energy per unit area of a Bloch wall is readily obtained as

$$E_w = \pi\sqrt{AK}. \tag{1.27}$$

Only if this domain wall energy is less than the reduction in magneto-static energy can domains form.

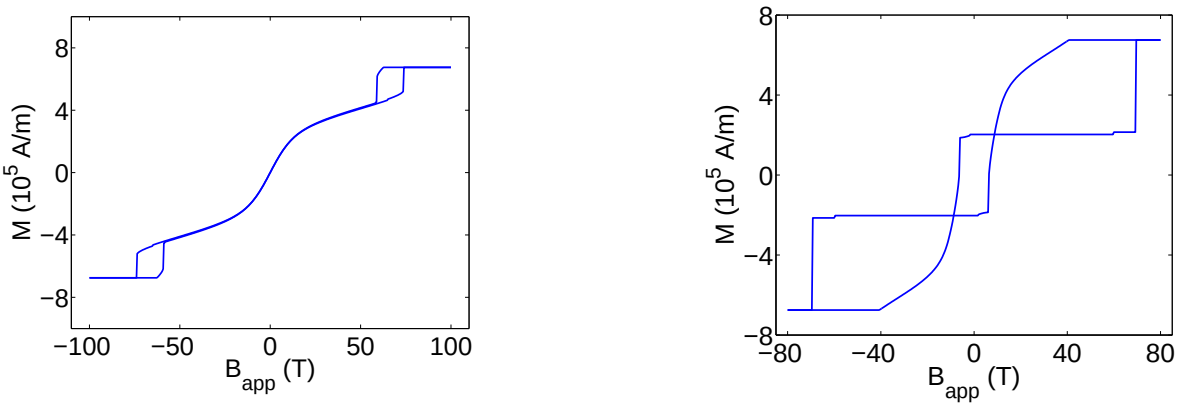

Figure 1.8: Transition from spin-flop (left, [$DyFe_2$ 10 Å/YFe_2 40 Å] × 80) to negative coercivity (right, [$DyFe_2$ 20 Å/YFe_2 80 Å] × 40) loops. Simulated at 100 K with field along $[00\bar{1}]$ using OOMMF.

1.6 Non-ideal exchange springs

Conventionally, exchange spring behaviour is discussed in the ideal case: the soft phase has negligible anisotropy and the hard phase is infinitely hard. Then the exchange spring will form in the soft phase only, and the bending field depends inversely on the square of the soft layer thickness $B_B \propto 1/t_s^2$, as shown experimentally in [40]. However, deviation and complexity do arise. For instance, for a fixed 1:4 ratio between the hard and soft layer thicknesses, there are transitions from spin-flop to negative coercivity hysteresis characteristics, as can be seen in Fig. 1.8. The same transition was actually observed experimentally [2]. More importantly, the switching mode at room temperature is different from that at low temperatures, which is relevant for applications. At low temperature, the hard phase is parallel to the positive field direction when ramping down the applied field from a positive value to zero. While at room temperature, it is the soft phase parallel to the positive field direction. This difference can be understood through the reduced hard anisotropy at room temperature. Conversely, an increase of anisotropy in the soft phase gives another non-ideal character, the irreversible exchange springs. The study of these non-ideal exchange springs is the main objective of this thesis.

Chapter 2

Experimental techniques

In this chapter, two methods used to investigate the magnetic properties of the $DyFe_2$/ YFe_2 films are discussed: (i) Magneto optic Kerr effect (MOKE) and (ii) vibrating sample magnetometery. MOKE measures the change of polarization or amplitude of light reflected from a magnetic material. To first order, this change is proportional to the sample's magnetization. Due to the finite penetration depth of light in material, MOKE is surface sensitive and suitable for characterization of exchange springs, because exchange springs tend to form first in the top soft layer of a superlattice sample. However, the current MOKE setup can only work at room temperature with a maximum field of ~ 0.35 T. So low temperature and high field measurements require the use of the vibrating sample magnetometer (VSM). Sometimes, VSM data can help in the comprehension of the MOKE data. The operation principle and basics of MOKE and VSM are briefly discussed below.

2.1 Magneto optic Kerr effect magnetometer

2.1.1 Introduction

There are two magneto-optic effects: the Faraday effect and the Kerr effect. Both of them arise from the interaction between the incident electromagnetic wave and the magnetic field of materials. Both the Faraday and Kerr effects have the same origin: the spin-orbit interaction of electrons in atoms with applied external electromagnetic field. The Faraday effect rotates the refracted electromagnetic wave's polarization (birefringence), while for Kerr effect it is the rotation of the polarization of the reflected electromagnetic wave (dichroism). The Faraday effect was discovered by Michael Faraday in 1845. More than 30 years later, the Rev. John Kerr discovered the corresponding effect for reflected light. The first use of the magneto-optic Kerr effect in the field

of surface magnetism dates back to 1985 [41, 42]. Since then there have been many applications of MOKE to the characterization of surface magnetism. The advantages of MOKE lie in that it is simple, easy to implement, surface sensitive and capable of probing very small areas. But, limited field strength and difficulty of absolute determination of magnetic moments constitute the main disadvantages of MOKE. Besides the traditional surface MOKE configuration, there are several new developments suitable for different aims: diffracted MOKE or Bragg-MOKE using both reflected and diffracted light to probe the magnetic structure of patterned samples [43, 44, 45]; x-ray MOKE employing x-ray as the probe, with the advantage to be element specific with a tunable x-ray source (now available at synchrotron sources), and capable of separating spin and orbital contributions by varying polarization [46, 47]; time-resolved MOKE which can be used to study the dynamics of spins in materials [48, 49]; and finally, second harmonic MOKE which is sensitive to the interface magnetization, and may be adopted to characterize interface magnetic properties [50, 51, 52, 53]. Finally, in addition to sensing the magnetic state of a sample, magneto optic means can be used to manipulate the magnetization configuration, through either inverse Faraday effect [54, 55, 56, 57] or spin transfer torque [58].

From the theoretical point of view, there are two descriptions for the origin of MOKE, one microscopic, the other macroscopic. A comprehensive treatment of magneto optics in metals can be found in [59]. Here we first discuss the microscopic theory of MOKE. In metallic ferromagnetic materials, it is the exchange Weiss field which aligns the individual spins. However, the exchange interaction alone cannot explain the origin of MOKE, because it has nothing to do with the electron motion which determines the dielectric properties of materials. The coupling between electron motion and electromagnetic field originates from the spin-orbit interaction, which has the form $(\nabla V \times \mathbf{p}) \cdot \mathbf{s}$ and demonstrates clearly the link between electron motion and spin. Here V, $\mathbf{p}$ and $\mathbf{s}$ are the electron potential, momentum and spin, respectively.

There are two ways to calculate magneto-optic effects using single electron quantum theory. Both are cast within the framework of time dependent perturbation theory, with the spin-orbit interaction as the perturbation. One starts with the unperturbed Hamiltonian and eigenfunctions, subsequently using perturbation theory to obtain the first order changes in the wavefunctions. The current is then calculated according to the formulation for the conserving current in quantum mechanics. This procedure [60] defines the dielectric constants for the material considered through the constitutive relation between current and applied field. The dielectric constant obtained in this

way takes the form of a tensor [60]

$$\epsilon = \begin{pmatrix} A_0 & -A_1 & 0 \\ A_1 & A_0 & 0 \\ 0 & 0 & A_0 \end{pmatrix} \tag{2.1}$$

for a cubic ferromagnetic sample uniformly magnetized in the positive z-direction. Here A_0 is the electronic part of the dielectric constant, which remains the same as that for the nonmagnetized state, while A_1 is dependent on the sample's magnetization, which can be expressed as a linear function of the magnetization to the first order. For a wave incident from the $+z$-direction, these two elements of the dielectric constant will give rise to two eigenmodes according to Maxwell's equations. One is left handed circularly polarized and the other is right handed circularly polarized: their refraction indices differ from each other due to A_1. When considering the refracted wave, it is the Faraday effect; while for the reflected wave, it is the Kerr effect. Numerically, A_1 is almost two or three orders smaller than A_0. Thus very sensitive measurements are needed to observe magneto-optic effects. Following this approach, the contribution of intraband and interband transitions to the dielectric constant has been discussed in [61].

The other approach [62], using the same time perturbation theory, employs transition probabilities, which are easier to calculate, rather than the elusive wave functions. In addition, we know that from the principle of causality in relativity, we can relate the imaginary part of dielectric constants to the real part, or vice versa. The result is the well known Kramers-Kronig relationships. The imaginary part of dielectric constants can be related to the absorption of light, so once we get the absorption of light in a material we can deduce the imaginary part, and hence the real part can be obtained readily. In quantum mechanics, that absorption is represented by the probability of photons moving from one state to another, which can be computed easily using time dependent perturbation theory. Working in this way for a cubic material, we reach identical conclusions, but with different mathematical forms for A_j. Furthermore, sum-rules for the components of the conductivity (or equivalently, dielectric) tensor are also obtained.

From the quantum mechanical description of MOKE, we know that the origin of magneto-optic effects is spin-orbit interaction. If we want to calculate the dielectric constants from first principles, we need the complete electronic band structure of the material of interest, together with the spin-orbit interaction aimed at obtaining elements of the transition matrix. This remains a challenging task, although there have been some successes in this theoretical direction ([63], [64] and references therein, [65]). Therefore we need the macroscopic approach to this problem.

2.1.2 Macroscopic theory – transfer matrix method

The macroscopic description [66, 67, 68, 69] of MOKE starts with the phenomenological dielectric constant tensor characterizing the system's response to an external electromagnetic field. Given the fact that every rank two tensor can be decomposed into symmetric and antisymmetric parts, it is only the antisymmetric part that will bring about the Kerr effect. The symmetric part of the dielectric tensor can be diagonalized, and so absorbed into the diagonal dielectric constants, by coordinate transformation. So for an isotropic and homogeneous medium it cannot contribute to birefringence or dichroism. Hence the symmetric part is irrelevant in the discussion of MOKE and we will consider it to be characterized by a scalar constant ϵ and the complete dielectric constant tensor takes the form [66]

$$\tilde{\epsilon} = \epsilon \begin{pmatrix} 1 & iq_z & -iq_y \\ -iq_z & 1 & iq_x \\ iq_y & -iq_x & 1 \end{pmatrix}, \tag{2.2}$$

where $\mathbf{q} = (q_x, q_y, q_z)$ is the Voigt vector (or magneto-optical) constant. This definition of $\mathbf{q}$ allows us to write $\mathbf{D} = \tilde{\epsilon}\mathbf{E} = \epsilon\mathbf{E} + i\epsilon\mathbf{E} \times \mathbf{q}$.

On substituting Eq. (2.2) into Maxwell's equations and taking the incident wave to be a plane wave $\sim e^{i(\mathbf{k}\cdot\mathbf{x}-\omega t)}$ [1], we find [66]

$$\begin{cases} \mathbf{k}\cdot\mathbf{E} &= i\mathbf{k}\cdot(\mathbf{q}\times\mathbf{E}) \\ \mathbf{k}\times\mathbf{E} &= \omega\mu_0\mathbf{H} \\ \mathbf{k}\cdot\mathbf{H} &= 0 \\ \mathbf{k}\times\mathbf{H} &= -\omega\epsilon(\mathbf{E} + i\mathbf{E}\times\mathbf{q}) \end{cases}, \tag{2.3}$$

in which $\mathbf{B} = \mu_0\mathbf{H}$ has been used. Here we consider only the optical frequency magneto-optic response via the dielectric constant tensor. From (2.3), it is clear that $\mathbf{D}$ and $\mathbf{B}$ are perpendicular to $\mathbf{k}$ while $\mathbf{E}$ has a component parallel to the wave vector $\mathbf{k}$. The electric field vector can be decomposed according to the usual polarization decomposition [66]

$$\mathbf{E} = E_s\mathbf{e}_s + E_p\mathbf{e}_p + i(\mathbf{q}\cdot\mathbf{e}_s E_p - \mathbf{q}\cdot\mathbf{e}_p E_s)\mathbf{e}_k. \tag{2.4}$$

$\mathbf{e}_s$, $\mathbf{e}_p$ and $\mathbf{e}_k$ are the mutually perpendicular three unit vectors along the s-, p- polarization and $\mathbf{k}$ directions (Fig. 2.1). Thus the equations of motion for the s- and p-polarization components of the electric field can be obtained from (2.3). Explicitly

[1] It is sufficient here to consider only plane waves, because any other function can be viewed as a superposition of plane waves. Only specular reflection is considered and diffusive scattering is not taken into account.

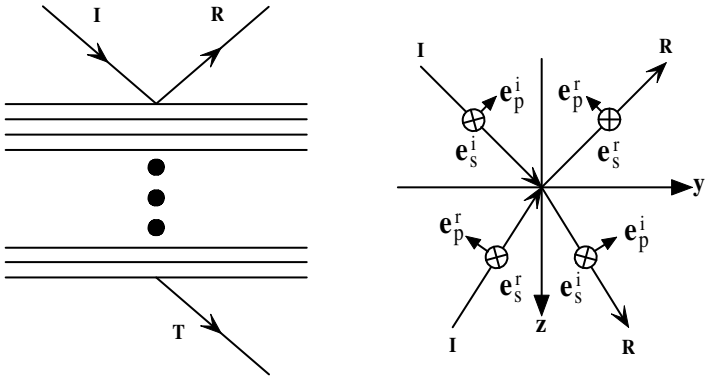

Figure 2.1: Schematic of multilayered structure (left) and definition of s- and p-polarizations (right). The omitted layers are represented as black dots. The crosses give the direction of s-polarization (pointing into the paper plane), and the short arrows specify the direction of p-polarization. I, R and T denote incident, reflected and transmitted light, respectively.

[66],

$$\begin{cases} \left(\frac{\omega^2\epsilon}{c^2\epsilon_0} - k^2\right) E_s + i\frac{\omega^2 \mathbf{q}\cdot\mathbf{e}_k\epsilon}{c^2\epsilon_0} E_p &= 0 \\ -i\frac{\omega^2 \mathbf{q}\cdot\mathbf{e}_k\epsilon}{c^2\epsilon_0} E_s + \left(\frac{\omega^2\epsilon}{c^2\epsilon_0} - k^2\right) E_p &= 0 \end{cases}, \tag{2.5}$$

where ϵ_0 is the vacuum permittivity, $\epsilon_0\mu_0 = 1/c^2$ and c is the speed of light in vacuo. Equations (2.5) to first order in $\mathbf{q}$ admit left (L)- and right (R)-circularly polarized states with eigenstates [66]

$$k_{R,L} = k(1 \pm \frac{1}{2}\mathbf{q}\cdot\mathbf{e}_k) \qquad \text{or} \qquad n_{R,L} = n(1 \pm \frac{1}{2}\mathbf{q}\cdot\mathbf{e}_k). \tag{2.6}$$

Here $k = n\omega/c$ and $n = \sqrt{\epsilon/\epsilon_0}$ are the wave number and refractive index without magnetization, respectively. All the modes of the electromagnetic waves in magnetic materials can be expressed as a linear superposition of the two eigenstates obtained above.

For electromagnetic waves propagating in a magnetic multilayered system (Fig. 2.1), we need the boundary conditions for the electromagnetic field in different layers. Because the boundary conditions are in terms of tangential components of the field, it is convenient to express them in terms of polarization components of the field and deduce the corresponding conditions for them. Suppose the coordinate is chosen to be that the x and y axes lie in the film plane, with y in the incident plane and x perpendicular to it, and the z axis is coincident with the film normal. For the x component of the electric field, the relation is simply [66]

$$E_x = E_s^i + E_s^r, \tag{2.7}$$

because s is parallel to x. The superscripts i and r refer to the incident and reflected waves, respectively. As the L and R modes have different refraction indices and propagating angles, the relation for the y component is complex [66]:

$$\begin{aligned} E_y &= E_p^{i,L}\cos\theta_L + E_p^{i,R}\cos\theta_R + i(\mathbf{q}\cdot\mathbf{e}_s^i E_p^i - \mathbf{q}\cdot\mathbf{e}_p^i E_s^i)\sin\theta \\ &- E_p^{r,L}\cos\theta_L - E_p^{r,R}\cos\theta_R + i(\mathbf{q}\cdot\mathbf{e}_s^r E_p^r - \mathbf{q}\cdot\mathbf{e}_p^r E_s^r)\sin\theta. \end{aligned} \tag{2.8}$$

For the electric components along z direction, a similar expression can be obtained, but there is no need to distinguish between θ_L, θ_R and θ. The reason lies simply on the fact that we are concerned only about the terms linear in $\mathbf{q}$ and the $\mathbf{e}_k$ term in (2.4) is already of the order $\mathbf{q}$. The difference between θ_L, θ_R and θ contributes only to higher order corrections. Under this approximation, the electromagnetic field can be characterized by a single propagating angle θ, instead of three.

Eq. (2.8) can be simplified with the definition of the propagating angles and the relation between s and p components [66]

$$\begin{cases} E_p^L = +iE_s^L & , \quad E_p^R = -iE_s^R \\ n_R\sin\theta_R = & n\sin\theta = n_i\sin\theta_i \quad = n_L\sin\theta_L \end{cases} \tag{2.9}$$

into [66]

$$\begin{aligned} E_y = &\frac{i}{2}\left[q_z s_\theta^2 - q_y t_\theta(1+c_\theta^2)\right]E_s^i + (iq_x s_\theta + c_\theta)E_p^i \\ &+\frac{i}{2}\left[q_z s_\theta^2 - q_y t_\theta(1+c_\theta^2)\right]E_s^r + (iq_x s_\theta - c_\theta)E_p^r, \end{aligned} \tag{2.10}$$

where the abbreviations $s_\theta = \sin\theta$, $c_\theta = \cos\theta$ and $t_\theta = \tan\theta$ have been used. θ_i is the incident angle and n_i is the refraction index of the incident medium. The corresponding relations for the magnetic components can be similarly obtained from $\mathbf{k}\times\mathbf{E} = \omega\mu_0\mathbf{H}$. We find [66]

$$\begin{aligned} H_x &= \frac{in}{2}(q_y s_\theta + q_z c_\theta)E_s^i - nE_p^i + \frac{in}{2}(q_y s_\theta - q_z c_\theta)E_s^r - nE_p^r, \\ H_y &= nc_\theta E_s^i + \frac{in}{2}(q_y t_\theta + q_z)E_p^i - nc_\theta E_s^r - \frac{in}{2}(q_y t_\theta - q_z)E_p^r. \end{aligned} \tag{2.11}$$

Note that a constant has been factored out to obtain (2.11). From Eqs. (2.7), (2.10) and (2.11), the x and y components of the electromagnetic field can be expressed by the s and p polarization amplitudes through a medium boundary matrix A as $F_c = AF_p$, where F_c is the column vector of the Cartesian coordinate incident and reflected field components and F_p is the corresponding polarization vector. The resulting 4×4

medium boundary matrix is [66]

$$A = \begin{pmatrix} 1 & 0 & 1 & 0 \\ \frac{i}{2}\left[q_z s_\theta^2 + q_y t_\theta (1+c_\theta^2)\right] & i q_x s_\theta + c_\theta & \frac{i}{2}\left[q_z s_\theta^2 - q_y t_\theta (1+c_\theta^2)\right] & i q_x s_\theta - c_\theta \\ \frac{in}{2}(q_y s_\theta + q_z c_\theta) & -n & \frac{in}{2}(q_y s_\theta - q_z c_\theta) & -n \\ n c_\theta & \frac{in}{2}(q_y t_\theta + q_z) & -n c_\theta & \frac{in}{2}(q_y t_\theta - q_z) \end{pmatrix}.$$

For two media with a single interface, A is sufficient to obtain the reflection coefficients. For multilayered systems, another matrix – the propagation matrix P – is needed to characterize the propagation of the field in different layers. The two surfaces of a film with thickness d are denoted as τ and β, with light propagating from τ to β. The incident and reflected waves at both surfaces are composed of L and R modes, hence we can use superscripts 1 and 2 to distinguish incident L and R modes, and 3 and 4 to discriminate those for the reflected ones. After propagation in the film, we have the following relations for the fields at two surfaces [66]

$$E_\tau^{1,2} = E_\beta^{1,2} \exp(idk^{1,2} c_\theta^{1,2}), E_\tau^{3,4} = E_\beta^{3,4} \exp(-idk^{3,4} c_\theta^{3,4}). \tag{2.12}$$

The fields at boundaries τ, $F_\tau = (E_s^i, E_p^i, E_s^r, E_p^r)_\tau^T$ and β, $F_\beta = (E_s^i, E_p^i, E_s^r, E_p^r)_\beta^T$, can be related as $F_\tau = P F_\beta$ by the propagation matrix P [66]

$$P = \begin{pmatrix} U c_\delta^i & U s_\delta^i & 0 & 0 \\ -U s_\delta^i & U c_\delta^i & 0 & 0 \\ 0 & 0 & U^{-1} c_\delta^r & -U^{-1} s_\delta^r \\ 0 & 0 & U^{-1} s_\delta^r & U^{-1} c_\delta^r \end{pmatrix} \tag{2.13}$$

with [66]

$$U = \exp(-ikdc_\theta), \delta^i = \frac{kd}{2}(q_y t_\theta + q_z), \delta^r = \frac{kd}{2}(q_y t_\theta - q_z). \tag{2.14}$$

The superscript T denotes the transpose of a matrix. With matrices A and P for each layer, we can calculate the reflection and transmission coefficients for the whole system as follows. The electric fields on the top of the system consist of incident and reflected waves while the electric field emerging from the bottom of the system comprises only the refracted one [66]

$$F_i = \begin{pmatrix} E_s^i \\ E_p^i \\ r_{ss} E_s^i + r_{sp} E_p^i \\ r_{ps} E_s^i + r_{pp} E_p^i \end{pmatrix}, F_f = \begin{pmatrix} t_{ss} E_s^i + t_{sp} E_p^i \\ t_{ps} E_s^i + t_{pp} E_p^i \\ 0 \\ 0 \end{pmatrix}. \tag{2.15}$$

r and t are 2×2 reflection and transmission matrices. Using continuity of the tangential components of field at each boundary, we have [66]

$$\begin{aligned} A_i F_i = A_1 P_1 F_1 = A_1 P_1 A_1^{-1} A_1 F_1 = A_1 P_1 A_1^{-1} A_2 P_2 F_2 \\ = \cdots = \prod_{m=1}^{N} (A_m P_m A_m^{-1}) A_f F_f, \end{aligned} \tag{2.16}$$

where F_i, F_f and generic F_n denote initial, final and the nth film's second boundary fields. So the transmission matrix defined through $F_i = T F_f$ is given by [66]

$$T = A_i^{-1} \prod_{m=1}^{N} (A_m P_m A_m^{-1}) A_f \equiv \begin{pmatrix} G & H \\ I & J \end{pmatrix}. \tag{2.17}$$

With those 2×2 submatrices G, H, I and J, it is easy to get the reflection and transmission matrices r and t as [66]

$$t = G^{-1} = \begin{pmatrix} t_{ss} & t_{sp} \\ t_{ps} & t_{pp} \end{pmatrix} \qquad \text{and} \qquad r = IG^{-1} = \begin{pmatrix} r_{ss} & r_{sp} \\ r_{ps} & r_{pp} \end{pmatrix}. \tag{2.18}$$

The general expressions can be very complex. However, in the thin film limit for a multilayer sample, $\frac{2\pi}{\lambda} \sum_m d_m |N_m| \ll 1$ with d_m the thickness of the mth layer, the reflection coefficients for small incident angles ($\theta_i \sim 0$) can be simplified considerably to [67, 68]

$$\begin{aligned} r_{sp}^P = r_{ps}^P = -\frac{4\pi}{\lambda} \frac{N_i}{(N_i + N_f)^2} \sum_m N_m^2 q_m d_m, \\ r_{sp}^L = -r_{ps}^L = -\frac{4\pi}{\lambda} \frac{N_i^2 N_f \cos\theta_i}{(N_i + N_f)^2} \sum_m q_m d_m. \end{aligned} \tag{2.19}$$

Here N_i and N_f are the refractive indices of the incident and final media, P and L denote the polar and longitudinal configurations between the incident light and the sample magnetization, θ_i is the incident angle, and $q_m = |\mathbf{q}_m|$ is the modulus of the Voigt constant of the mth layer. Obviously, the contribution from each layer is additive in this limit. For our superlattices, we have only two composites, so only two terms survive in (2.19).

2.1.3 Experimental setup

In the usual experimental MOKE setup, we measure the reflected intensity variation with the magnetization. The intensity measured by the photo detector is [66]

$$I \propto |E_s \sin\delta + E_p \cos\delta|^2 \approx |E_s \delta + E_p|^2 \tag{2.20}$$

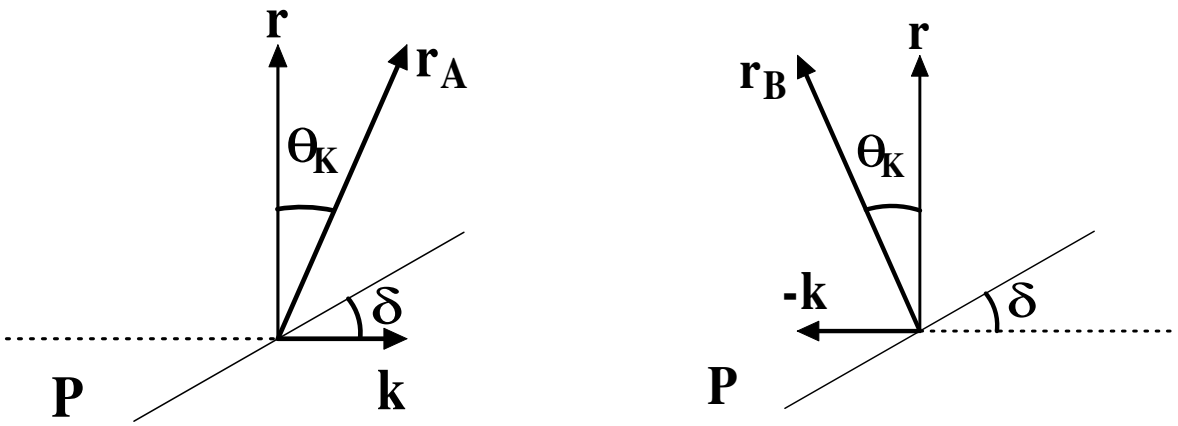

Figure 2.2: Illustration of standard reflection **r** and Kerr reflection **k** for positive (left) and negative (right) magnetization. The fixed angle δ is the angle of the analyzer with respect to the plane of incidence. P denotes the analyzer's axis of polarization. The sum of **r** and **k** is the total amplitude, $\mathbf{r}_A$ or $\mathbf{r}_B$. All the components are in the plane of the paper.

with the small angle δ between the polarizer and the p-axis. Here the convention that the p-axis is in the plane of incidence and the s-axis is perpendicular to it is adopted. The polarizer is used to analyze the reflected light and will be referred to as the analyzer. E_s and E_p are the corresponding s and p components of the electric field. In the above expression for I, it is assumed that the incident light is s-polarized and a small p-component is induced after reflection. Given that the definition of the Kerr rotation $E_p/E_s = \theta_K + i\epsilon_K \propto M$, which is valid because the Voigt constant is small, we have, to first order [66],

$$I \propto |E_s|^2|\delta + \theta_K + i\epsilon_K|^2 \approx |E_s|^2(\delta^2 + 2\delta\theta_K) = I_s\left(1 + \frac{2\theta_K}{\delta}\right) \tag{2.21}$$

with $I_s = |E_s|^2\delta^2$ representing the intensity at zero Kerr rotation. θ_K and ϵ_K are the Kerr rotation angle and ellipticity. Since both θ_K and ϵ_K are proportional to the magnetization M, the measured intensity as a function of applied field H yields the magnetic hysteresis loops.

Noise is always present and inevitably manifests itself in every experiment. In order to obtain a better experimental result, a higher signal to noise ratio (S/N) is desirable. The following analysis for MOKE follows the conventions and definitions in [70]. The simple case of s-polarized incident light, with magnetization within incident plane and perpendicular to the film normal, is considered again. No phase difference ($\epsilon_K = 0$) is assumed upon reflection between the standard, magnetization independent, and Kerr reflections, and in practical cases this can be achieved through the addition of a retardation plate to remove any phase difference if present. The signal is then

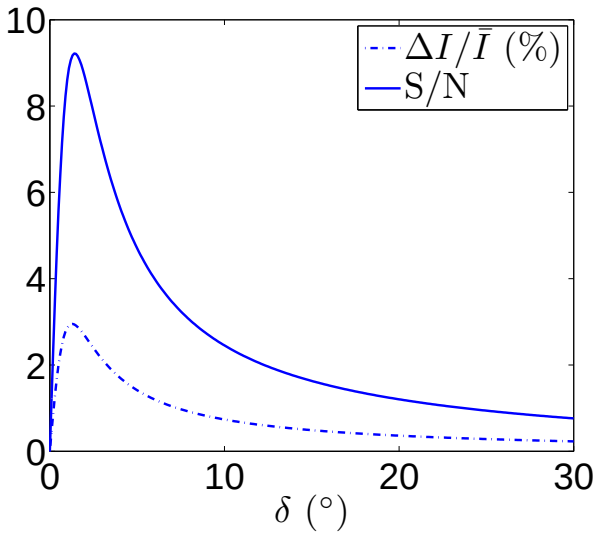

Figure 2.3: Signal to noise ratio S/N and fraction MOKE signal $\Delta I/\bar{I}$ available for the system used in our experiments. The analyzer used to detect the reflected light is inclined at an angle δ into the plane of incidence. The Kerr rotation of $DyFe_2$ [71] is adopted.

detected through a photo detector placed after the analyzer with an angle δ to the incident plane. For the configurations in Fig. 2.2, the intensities are [70]

$$\begin{aligned} I_A &\propto I_0 \cos^2(\frac{\pi}{2} - \delta - \theta_K) = I_0 \sin^2(\delta + \theta_K), \\ I_B &\propto I_0 \cos^2(\frac{\pi}{2} - \delta + \theta_K) = I_0 \sin^2(\delta - \theta_K), \end{aligned} \tag{2.22}$$

with θ_K the Kerr rotation angle. When there is no phase difference, θ_K is the angle between vectors of the normal and Kerr reflected amplitudes. I_0 is the modulus of r_A and r_B, $I_0 = |r_A|^2 = |r_B|^2$. The average of I_A and I_B [70]

$$\bar{I} \propto \frac{I_0}{2}(1 - \cos 2\delta \cos 2\theta_K) \approx I_0 \sin^2 \delta, \qquad \text{for} \quad \theta_K \sim 0 \tag{2.23}$$

can be viewed as the base signal, while the difference, the MOKE signal, is related to the change of magnetization, via θ_K, as [70],

$$\Delta I \propto I_0 \sin 2\delta \sin 2\theta_K. \tag{2.24}$$

Using Eqs. (2.23) and (2.24) the fractional MOKE signal, which acts as a measure of the contrast of MOKE signal, is defined as [70]

$$\frac{\Delta I}{\bar{I}} = \frac{2 \sin 2\delta \sin 2\theta_K}{1 - \cos 2\delta \cos 2\theta_K}. \tag{2.25}$$

This expression is only valid for a perfect analyzer. However, the imperfection of the analyzer used can be taken into account by a depolarization constant $\gamma_D = I_{min}/I_0$.

So finally [70],

$$\bar{I} \propto \frac{I_0}{2}(1 - \cos 2\delta \cos 2\theta_K + 2\gamma_D),$$
$$\frac{\Delta I}{\bar{I}} = \frac{2 \sin 2\delta \sin 2\theta_K}{1 - \cos 2\delta \cos 2\theta_K + 2\gamma_D} \approx \frac{2\theta_K \sin 2\delta}{\sin^2 \phi + \gamma_D}, \tag{2.26}$$

where again, the last step is valid only for small θ_K. A plot of the fractional MOKE signal can be seen in Fig. 2.3 as a function of the analyzer angle δ using the Kerr rotation angle and depolarization constant appropriate for our experiments, as given in Table 2.1. An approximate analytical expression for the optimal polarizer angle can be obtained by differentiating the last expression in (2.26) with respect to δ. This gives $\delta_{max} = \sqrt{\gamma_D}$ and $(\Delta I/\bar{I})_{max} = 2\theta_K/\sqrt{\gamma_D}$ for small δ. These equations are only approximately valid but nevertheless lend some insight into designing a MOKE magnetometer. For example, one can use a long focal length objective lens to reduce the range of angles of incidence and hence γ_D. However, this enhancement of contrast may be offset in the case of measuring a single magnetic nanostructure, for the focal spot size on the sample maybe increased to cover more than the interested sample area with a long objective focal length and hence reduce θ_K [70].

Kerr rotation angle, θ_K	300 μrad [71]
Depolarization constant, γ_D	2.1×10^{-4} [2]
Incident power, P_0	0.3 mW [2]
Laser intensity noise fraction, f_L	10^{-3} [2]
Efficiency, η	0.45 A/W [3]
Noise equivalent power, NEP	10^{-12} W/$\sqrt{\text{Hz}}$ [3]
Band width, $\Delta\nu$	100 kHz [3]
Resistance, R	3 MΩ [4]
Temperature, T	293 K

Table 2.1: Parameters used for the S/N plot and performance evaluation.

For the noise sources, only dark, shot, laser (or instrument) and Johnson noises [72] are included, with the assumption that the electromagnetic induction noise is negligible. The average signal current, $\bar{i}$, and MOKE current, Δi on the photodiode detector are

[2]Measured

[3]Front-End Optical Receivers, Models 2001 and 2011 Users Manual, New Focus, Inc..

[4]The product of NEP and η gives the noise (dark) current. The quotient between the measured noise voltage and the calculated noise current gives an estimate of R.

then [70]

$$\bar{i} = \eta \bar{P}, \qquad \Delta i = \eta \Delta P, \tag{2.27}$$

where η is the detector efficiency at the operating wavelength, $\bar{P}$ and ΔP are the average and MOKE signal power detected, respectively. They are obtainable by substitution of the corresponding Is to Ps in (2.26). Then the contributions of various noise sources can be calculated using [70]

$$\begin{aligned} \text{Dark current} : i_D = \eta \Delta \nu^{1/2}\ \text{NEP}, \text{Shot current} : i_S = (2e\bar{i}\Delta\nu)^{1/2}, \\ \text{Laser current} : i_I = f_I \bar{i}, \text{Johnson voltage} : V_J = (4k_B T R \Delta\nu)^{1/2}, \end{aligned} \tag{2.28}$$

where NEP is the noise equivalent power of the detector, $\Delta\nu$ is the measurement bandwidth, e is the absolute charge of an electron, f_I is the noise fraction of the laser beam (which may depend strongly on $\Delta\nu$), k_B is the Boltzmann constant, T is the working temperature and R is the transimpedance gain of the signal pre-amplifier of the photo detector to which all the currents should be referred. Under the assumption of independence of different types of noise, the total power is simply the sum of each noise power and the signal to noise ratio is [70]

$$\frac{S}{N} = \frac{R\Delta i}{[R^2(i_D^2 + i_S^2 + i_I^2) + V_J^2]^{1/2}} = \frac{\Delta i}{[i_D^2 + i_S^2 + i_I^2 + V_J^2/R^2]^{1/2}}. \tag{2.29}$$

From the second expression, it is obvious that the parameter R enters S/N only through the Johnson voltage. The net effect is a $1/\sqrt{R}$ dependence of S/N. So the dependence on R of the signal to noise ratio is mild. The typical parameters for the laser and analyzer used in our experiment are given in Table 2.1. Corresponding to those parameters, the plot of signal to noise ratio is shown in Fig. 2.3. It can be seen that we have a peak at $\delta \sim 3^\circ$.

A S/N ratio as high as 10 could therefore be obtained in our system, and the actual experimental results corroborate this prediction. With a commercial laser and polarizers, the surface MOKE magnetometer with the sensitivity to a magnetic moment of $\mu \sim 6 \times 10^{-12}$ emu can be achieved [70].

The experimental MOKE geometry can be categorized into three types according to the relative configuration of the incident plane and the sample magnetization: for polar MOKE the magnetization lies in the incident plane and perpendicular to the film surface, for longitudinal MOKE the magnetization lies in the incident plane but parallel to the film surface, whereas for transverse MOKE the magnetization is in the film surface and perpendicular to the incident plane. An illustration of the three geometries can be seen in Fig. 2.4. The enumeration of three geometries of MOKE is according to their relative importance. For the same magnitude of Kerr rotation, the

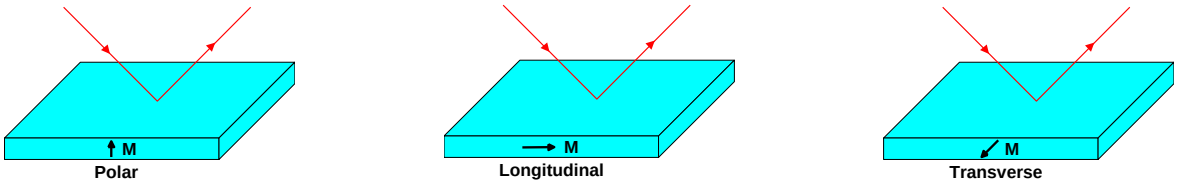

Figure 2.4: Three configurations of experimental MOKE: polar, longitudinal and transverse (left to right).

polar contribution to MOKE signal is the most important one, the next is longitudinal, while the transverse is the least important [69]. Further, the polarization plane of linear incidence rotates in both the polar and longitudinal cases, but transverse MOKE can only change the amplitude of reflected wave with respect to normal reflection, without rotation of polarization.

In our experiment, the longitudinal configuration is adopted: the sample is placed between two poles of an electromagnet, with the film plane perpendicular to poles, so the applied magnetic field is in the film plane, see Fig. 2.5. A He-Ne 632.8 nm linearly polarized, intensity stabilized laser is used as the light source. In order to minimize the spot size incident on the sample, aiming at probing as small region as possible, two dispersing lenses (D1 and D2) are placed in front of the laser and on the light path, and a focusing lens (F1) is applied to focus the expanded beam to a small spot. On the detection side, two focusing (F2 and F3) lenses are also used to collect the reflected light to a photodiode. Besides them, two polarizers (P and A), one to polarize (P) the incident light and another to analyze (A) the reflected light, are used with polarization angles almost perpendicular to each other in the experiment. The reason that we do not use the complete cross configuration is that with a finite ($< 90°$) angle, between the polarizer and analyzer, we can obtain a higher S/N ratio, as mentioned earlier, but also avoid the region where the nonlinearity of the intensity with respect to magneto-optic constant $\mathbf{q}$ is more intensive [73], cf. Eq. (2.22) for $\delta \to 0$. In the ideal case, the optical axes of all elements should be aligned with the wave vector of the laser beam, on which all proceeding discussions are based. Deviation from perfect alignment could reduce the signal contrast. On the other hand, perfect alignment of all optical elements results in multiple reflection of light, rendering the interpretation of data difficult. To avoid this complication, a slightly off axis configuration is used. The field generated by the electromagnet is measured by a Hall probe placed near the sample. The triangle wave form used to control the power supply to the electromagnet is generated by a function generator. Two multimeters, one connected to the Hall probe and the other to the photodiode, are connected to a computer. The interface and data collection is

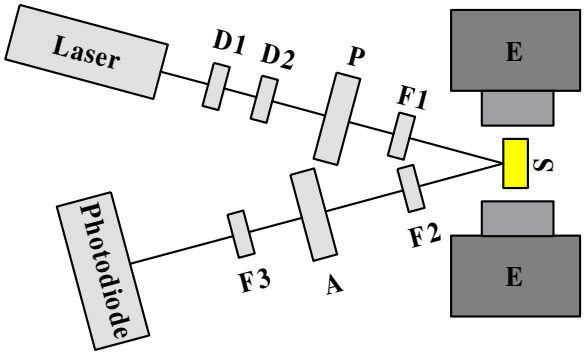

Figure 2.5: Diagrammatic representation of the equipments used in the measurement of surface MOKE. D1 and D2 are two dispersing lenses. F1, F2 and F3 are three focussing lenses. P and A are two polarizers. E is the electromagnet and S is the sample to be measured.

realized through HP VEE [5]. Finally, the analysis of the collected data is accomplished using MATHCAD [6].

In the discussion of the preceding paragraph, we have neglected the polar and transverse components of the magnetization vector, so a longitudinal configuration is realized (Fig. 2.4). However, if those components are not zero in the measurement, the change in light intensity is given by the combination of all nonzero components of the magnetization vector, instead of with only the longitudinal component contributing, as what is intended for. This fact can be simply traced back to the small incident angle (with respect to the film normal) of light in our MOKE setup, which enhances the polar signal relative to the longitudinal one. As we will see in Chapter 4, if the polar component of the magnetization vector is not zero, the measured MOKE intensity will also be affected by the variation caused by that component. The resulted hysteresis loop can be dramatically different from the conventional hysteresis loop measured by induction methods. Similar behaviour due to an additional transverse magnetization component was observed in (001) single crystal Fe/GaAs films [74]. By varying the angle between the analyzer and the plane of incidence, transverse and longitudinal components can be separated [74]. Additional contribution from the polar component to longitudinal MOKE was also observed in thin Co films grown on (111) Au [75]. The polar and longitudinal contributions can be disentangled by changing to a negative angle of incidence.

Theoretically, we can calculate the minimum Gaussian beam width w_2 from the

[5]HP VEE® is a registered trademark of Hewlett-Packard
[6]MATHCAD® is a registered trademark of MathSoft

laser after the focussing of three lenses with focal lengthes f_1, f_2 and f_3 as

$$w_2 = \frac{\lambda}{\pi}\frac{f_3}{d}\frac{f_1}{f_2}\sqrt{1+\left(\frac{\beta}{R}\right)^2}, \tag{2.30}$$

where λ is the wave length, d is the beam width at a certain position, R is the radius of curvature at that same point, and $\beta = \pi d^2/\lambda$ is the corresponding depth of focus. If we take those parameters at the beam waist, $R \to \infty$, this expression reduces to

$$w_2 = \frac{\lambda}{\pi}\frac{f_3}{d}\frac{f_1}{f_2}, \tag{2.31}$$

from which we can see that if a small spot size is desired a small focal length f_3 for the focussing lens or a large width of the incident beam is appropriate, for a fixed incident wave length. Experimentally, it is very easy to get an estimate of the actual spot size by scanning the beam through the sample edge and measuring the corresponding variation of the reflected beam with the photodiode. Using this method we got an actual spot size of ~ 100 μm, which is larger than the ideal size calculated to be ~ 10 μm.

2.2 Vibrating Sample Magnetometer

Ever since its first implementation in 1959 [76], the vibrating sample magnetometer (VSM) has become the standard apparatus for routine characterization of magnetic properties, due to its versatility, high sensitivity and ease of use. The operational principle behind any VSM is Faraday's law of induction: a moving magnetic moment will induce an electromotive force (emf) in any pickup coil close to it. A schematic sketch illustrating how a VSM works can be seen in Fig. 2.6: a magnetic sample is attached to the sample rod, which vibrates sinusoidally along the z-axis. Two pickup coils are located just above and below the middle point of sample vibration; the sample is magnetized by an external field $\mathbf{B}$ parallel to the z-axis. If the dimensions of the sample and the cross sections of the pickup coils are far less than other length scales, the sample can be viewed as a magnetic dipole and the coils as ideal thin coils. Under this assumption, the general analysis of any VSM's output voltage as a function of the vibrating moment can be simplified considerably by the use of the principle of reciprocity [77]: the magnetic flux through a pickup coil generated by a magnetic moment $\boldsymbol{\mu}$ is reciprocal to the field induced by the same coil carrying a current I [78]

$$\mathbf{B} \cdot \boldsymbol{\mu} = I\Phi, \tag{2.32}$$

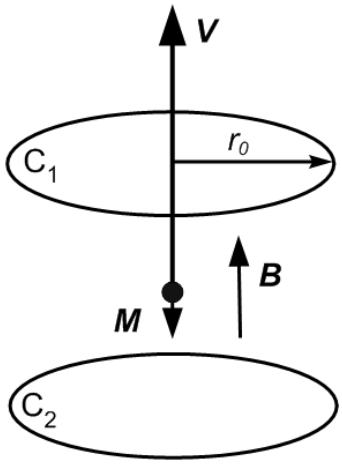

Figure 2.6: Schematic of an axial VSM. C_1 and C_2 are two pickup coils, connected in series opposition. Sample M can be driven by the sample rod to vibrate sinusoidally with frequency ω around the equilibrium position, $\triangle z \propto \sin \omega t$. The applied field, magnetization and axis of pick-up coils are all parallel to the z-aixs.

where $\mathbf{B}$ is the magnetic induction field at the location of the moment [7]. We consider first the simple case of only one pickup coil. In free space, the induced voltage is proportional to the time derivative of the flux [78] (provided the time delay due to the finite speed of light can be neglected, $l \ll \lambda$, where l is the distance between the moment and the pickup coil, and $\lambda = c/\omega$ is the radiation wavelength. The moment vibrates at frequency ω.)

$$V(t) = \frac{d\Phi}{dt} = \nabla \left(\frac{\mathbf{B}(\mathbf{r})}{I} \cdot \boldsymbol{\mu} \right) \cdot \frac{d\mathbf{r}}{dt} = \boldsymbol{\mu} \cdot \overleftrightarrow{G}(\mathbf{r}) \cdot \mathbf{v}(t) \tag{2.33}$$

with $\mathbf{v}$ the sinusoidal velocity of the moment. The tensor sensitivity function is defined by the gradient $\overleftrightarrow{G} = \nabla(\mathbf{B}/I)$. Obviously, $\overleftrightarrow{G}$ is a harmonic function $\nabla^2 \overleftrightarrow{G} = 0$, and the all space integral of $\overleftrightarrow{G}$ is zero $\int_\infty \overleftrightarrow{G} d^3\mathbf{r} = 0$ [8]. For the simple case considered here, the axis of the pickup coils is parallel to the moment, both parallel to the applied magnetic field $\mathbf{B}$. The sensitivity function for this axial configuration reduces to a scalar G, and can be calculated from the Biot-Savart law. For a single pickup coil the result is [79]

$$G \propto r_0^2 Z (Z^2 + r_0^2)^{-5/2}, \tag{2.34}$$

[7] This reciprocity is nothing else but the fact that the interaction energy of the coil-moment system can be calculated from either side; the interaction energy is the left hand side if calculated from the moment's point of view, while it is the right hand side from the coil's point of view.

[8] The first equation follows from $\nabla \cdot \mathbf{B} = 0$ and the second is a natural result from the boundary condition $\mathbf{B}(\infty) = 0$.

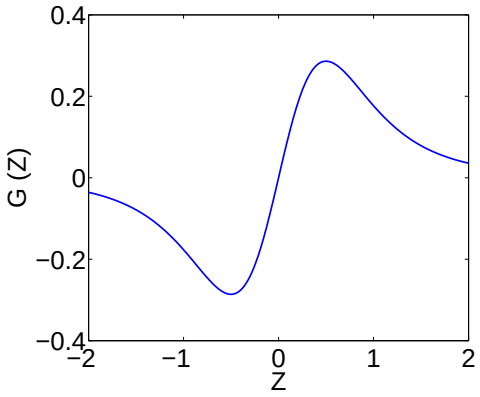

Figure 2.7: The sensitivity function G for a single coil, as a function of the distance away from the coil centre, along its axis.

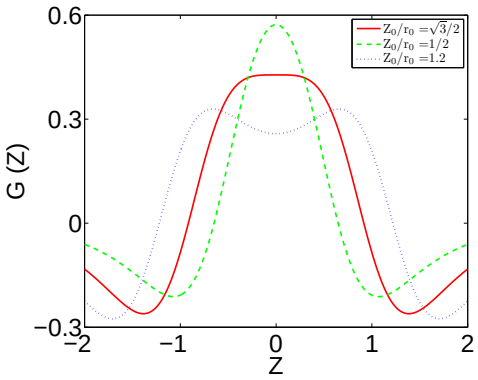

Figure 2.8: The sensitivity function G for two axially aligned coils for various separation-to-radius ratio Z_0/r_0. The distance Z is measured axially from the middle point of the two pickup coils.

where r_0 is the radius of the pickup coil and Z is the distance of the moment from the centre of the coil along the axis [9]. This function is plotted in Fig. 2.7 for $r_0 = 1$ against the position of the moment Z.

The above discussion is only valid under ideal conditions. In real life, various noise sources will inevitably come into play. Field inhomogeneity is one of them, and this inhomogeneity will make an appreciable contribution to the induced voltage in the pickup coil; the higher the field the larger this contribution will be. One way to circumvent this problem is to have two otherwise identical pickup coils connected in series opposition, one above and one below the vibrating sample. Due to the reversed velocity of the vibrating sample with respect to the two coils, the signal from the sample will be added, while that from the field inhomogeneity will be subtracted to almost cancelation. Suppose the sample position is displaced a distance Z from the centre of the coils along the alignment axis, then the output voltage will be given by [78, 79]

$$G \propto r_0^2 \left[(Z_0 + Z) \left((Z_0 + Z)^2 + r_0^2 \right)^{-5/2} + (Z_0 - Z) \left((Z_0 - Z)^2 + r_0^2 \right)^{-5/2} \right] \qquad (2.35)$$

with Z_0 the distance between the two coils. From this expression, the optimal insensitivity to displacement of sample can be achieved at $Z_0 = \sqrt{3} r_0/2$ (the saddle point) [79, 78]. The sensitivity function corresponding to this value, together with other two

[9] Actually, the field produced by a current carrying element is $d\mathbf{l} \times \mathbf{r}/r^3$; the component along the moment (z) direction is $\cos\theta/r^2$. Integrating this along the coil gives $2\pi a_0 \cos\theta/r^2 = 2\pi a_0^2/r^3$, whose derivative is exactly (2.34). This expression can also be obtained from the scalar potential of a magnetic dipole $\propto \boldsymbol{\mu} \cdot \mathbf{r}/r^3$, under this simple configuration.

representative values, can be seen in Fig. 2.8. The insensitivity of the optimal geometry to sample displacement is obvious from this figure (see red curve). For the actual implementation and optimization of a VSM, various coil arrangements [80] and noise resources [81, 82], including sample position and geometry effects, have been studied thoroughly in the literature.

If the sample size is not small compared to the distance between it and the pickup coils, the dipole approximation breaks down. Under this situation, the induced voltage will be an integral over the whole sample

$$V \propto \int G(\vec{r})\mathbf{M}(\mathbf{r})d^3\mathbf{r} \tag{2.36}$$

assuming that the magnetization is still along the z-axis $\mathbf{M}(\mathbf{r}) = M(\mathbf{r})\mathbf{e}_z$. As it appears in Eq. (2.36), G must be a constant over all the sample volume, otherwise the output will only be an average of the product of the sensitivity function and the magnetization over the whole sample. If the saddle point configuration of the coils is chosen, provided the sample size is smaller than the dimension of the flat region and the sample is uniformly magnetized, G and $\mathbf{M}$ are both constant and it is not a problem. However, a priori knowledge about the coil geometry and sample state is hence required to decide the appropriate sample size. So a smaller sample is always preferable, even in expense of the magnitude of the output signal. The smallest sample volume is determined by the VSM base noise level, below which no signal can be detected reliably, roughly speaking. In actual measurements, the optimal sample position is actually determined by the maximal point of the sensitivity function, which gives the largest output voltage. In general therefore, the output signal of a VSM is proportional to the magnetization M. However, to establish a direct relationship between induced voltage and magnetic moment value, the constant parameter G needs to be determined. The usual approach consists in using a sample with known saturation magnetization. This sample should ideally have the same geometry (both size and shape) with and preferably a larger magnetization of saturation than the sample under investigation. Nickel spheres are usually used for this objective, as they can be obtained in high purity and can be saturated at relatively low fields.

In this work, a commercial Oxford Instruments Aerosonic 3001 axial VSM was used to measure the magnetic properties of the $DyFe_2/YFe_2$ multilayer films. For this VSM, the frequency and the amplitude of the sinusoidal motion is typically set at 66.66 Hz (50 Hz mains) and 1.5 mm (adjustable from 0.1 to 2 mm with stability better than 0.1%) respectively. The actual vibration amplitude has almost no effect on the sensitivity function; it only changes the absolute value of the induced emf: the larger the amplitude the larger the signal, which is very obvious from Eq. (2.33). But very

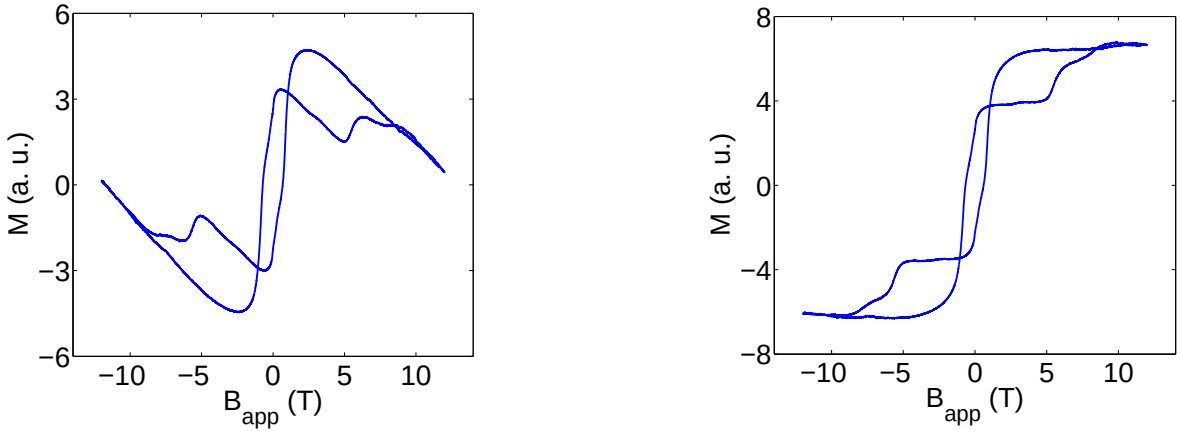

Figure 2.9: Hysteresis loops before (left) and after (right) background subtraction, through a linear fitting to the high field part of the raw data loop.

large amplitudes are not possible given the dimensions of the suspended magnet. So an amplitude of $\sim$ 1 mm was selected. The Nb_3Sn superconducting magnet incorporated in the VSM provides fields up to 12 T, with sensitivity of 1 Oe. This magnet has a homogeneity of 0.1% over a 10 mm diameter sphere. The sensitivity of the instrument is $\sim 6.0 \times 10^{-6}$ emu at zero field and $\sim 2.7 \times 10^{-4}$ emu at 12 T. The magnet is surrounded by a jacket of liquid He, which cools it to the superconducting state. This, in turn, is surrounded by a vacuum. Outside this space is a jacket of liquid nitrogen. The vacuum and liquid nitrogen reduce the rate at which liquid He is lost through evaporation. Liquid He can be sprayed through a needle valve into a space around the sample in order to cool it. The liquid He expands adiabatically as it flows into the space through the needle valve. Thus, temperatures below liquid He temperature (4.2 K) are achievable. There is a heater within the 52 mm diameter magnet bore. The heater power and the flow of liquid He from the needle valve are adjusted to stabilize the temperature at a given target value. To alleviate lateral vibration, a light and rigid carbon fiber tube is used as the sample rod. Another advantage of carbon fiber is the small diamagnetic response.

The thickness of the Laves phase films is typically 4000 Å. The sapphire substrate thickness is $\sim$ 1 mm. Measurements were made on roughly square pieces of those films. These pieces are typically 5 mm on a side. Larger sizes risk friction with the sides of the pickup coils and are a source of noise. 5 mm samples provide sufficient signal (typically $\sim 1 \times 10^{-3}$ emu) while being small enough to avoid frictional noise. Before the actual acquisition of hysteresis loops, a z (height) scan is performed at 300 K, 0.5 T to find the maximum of the sensitivity function G. At lower temperatures, a higher field is needed to saturate the sample, which also enhances the diamagnetic contribution, which in turn tends to decrease the signal. The sample holder and sapphire substrate have a

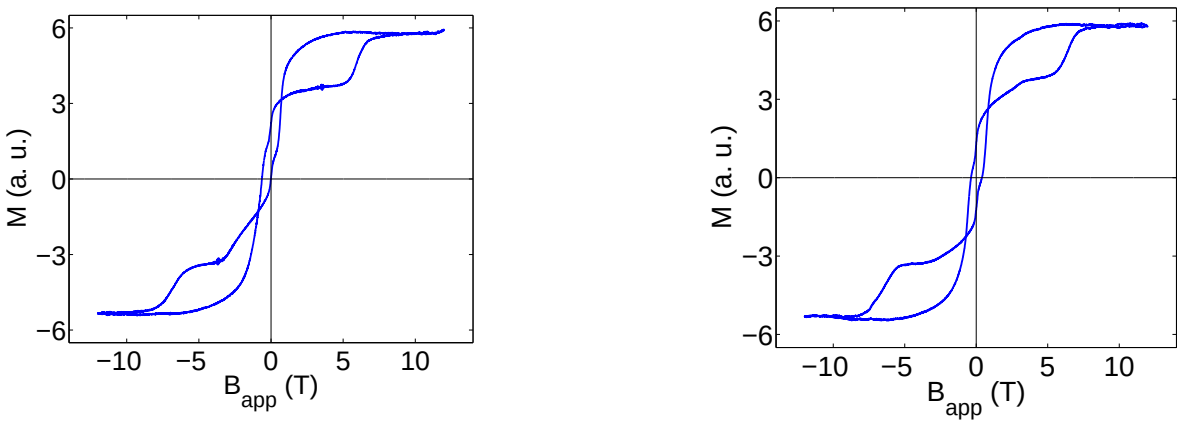

Figure 2.10: Unsaturated (left) and saturated (right) hysteresis loops. The saturation is achieved through field cooling at 12 T from 300 K. The applied field B_{app} is parallel to the $[\bar{1}10]$ axis.

very large volume compared with the Laves phase material. Then, the data shows a significant diamagnetic component from the holder and substrate. This component is removed by simple linear subtraction, with the diamagnetic correction obtained by fitting the high field data. As an example, the background subtraction is shown in Fig. 2.9 for the (110) multilayer [$DyFe_2$ 40 Å/YFe_2 160 Å] × 20 at 50 K, with field along the $[\bar{1}10]$ direction.

The VSM measures the moment of the entire sample in emu. If values for the magnetization of the sample are to be made, the sample dimensions must be known. Then the unit of magnetization can be converted to Bohr magnetons per formula unit (μ_B/f.u.). When the quantitative values of magnetization are not important, the normalized magnetization M/M_s is often used. This is simply the ratio of the magnetization M to its value at saturation M_s. The absolute values of the magnetization of $DyFe_2$ and YFe_2 at different temperatures have been measured extensively before, so here only the relative magnetization is of interest.

It is important to apply a sufficiently large field to saturate the magnetization of a sample. If the sample starts from a unsaturated state, the magnetic history of the sample is then important. In the virgin state, there are many randomly oriented domains, resulting in a net zero magnetization. If a positive field is applied, domains aligned parallel with the field grow at the expense of their antiparallel counterparts. This process gives rise to the initial increase in magnetization as the applied field is increased from zero. At magnetic saturation, the sample can be considered as a single domain. During the course of a full hysteresis loop, the sample will be exposed to a negative field large enough to reverse its magnetization. If the field is then brought back to a large positive value, the magnetization curve will not generally lie on top

of the initial magnetization curve. This is the magnetization process from the virgin state to a large enough field to saturate the sample. If the field is not large enough, complicated partial loops, which are difficult to interpret, appear. For some samples at very low temperatures, we cannot saturate the samples even at the highest field 12 T. This unsaturated state can be easily inferred from the displacement of the hysteresis curve from the field origin. Field cooling from a high temperature (usually room temperature) was then used to bring the sample into saturation. As an example, magnetization loops, with and without field cooling, for the (110) multilayered [$DyFe_2$ 40 Å/YFe_2 80 Å/$DyFe_2$ 8 Å/YFe_2 80 Å] $\times$ 20 at a temperature of 100 K are shown in Fig. 2.10, with field along [$\bar{1}$10]. The slightly, unequal magnitudes of the saturation magnetization at the positive and negative fields, are due either to the misalignment of the sample rod with respect to the pickup coil axis, slight bending of the sample rod, or instrumental offset. But it does not affect the interpretation of the data.

Chapter 3

Analytical description of exchange spring superlattices

To understand the mechanism responsible for the formation of an exchange spring, we need to investigate the dynamics of the magnetization process for superlattices. Heralded by the work of Stoner and Wohlfarth, there are many approaches to describe the magnetization process. One can start from the expression for the total energy density of the interacting spin system and minimize it to get the magnetization curve [83, 84, 85]. Alternatively, one can work with the LLG equation, solving for the evolution of spins in the system considered, to get the magnetization process [86, 87]. In addition, we also have the option to use the continuum model to describe the response of the system under the influence of an external field [88, 89, 90, 91]. In this chapter, we use the continuum model to describe qualitatively the response of our exchange-spring system under the influence of an external field [88, 89, 90, 91]. The continuum model can be solved analytically, and so provides more physical insight into the magnetization process. Following the method described in [89, 91] for the description of FM coupled superlattices, with both in-plane and out-of-plane uniaxial anisotropy, the whole magnetization process of AFM superlattices can be studied using the continuum model, down to the scale of ~ 2 nm. In particular, we use this method to discuss the bending field in small fields, where the two phases are antiparallel. However, the same method can be applied to the determination of the bending field for the onset of deviation from parallel configuration in large fields, if the AFM coupling is not infinite.

The simple geometry considered here is depicted in Fig. 3.1: a magnetically soft layer, thickness t_s, is exchange coupled to a magnetically hard layer with thickness t_h. The soft layer has magnetization M_s and exchange constant A_s, while those parameters are M_h and A_h for the hard layer. For simplicity, in-plane uniaxial anisotropy, with z as the easy axis, is assumed in this theoretical analysis. Actually, this analysis can

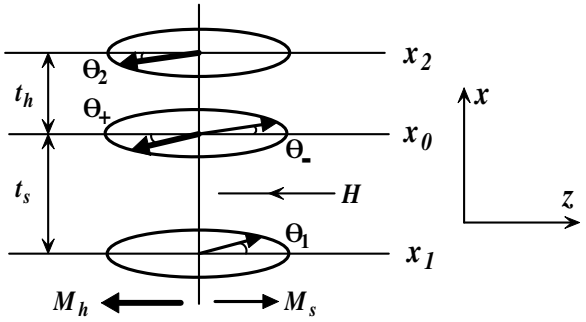

Figure 3.1: Schematic view of the bilayer structure used in this chapter. θ_1 and θ_2 are the deviation angles from antiparallel configuration at the soft and hard free surfaces, while θ_- and θ_+ are the corresponding angles at the interface. They are measured from the z and -z axes respectively, in the yz plane. The azimuthal angle ϕ is not shown explicitly here, which should be measured from the x axis, in the xy plane.

be carried out for perpendicular uniaxial anisotropy, as done in [91]. The interface exchange coupling A_0 could be negative (AFM) or positive (FM). The FM case has been studied extensively in [89, 91], so here the AFM case is considered. It is a trivial generalization of the method to include AFM coupling in the model. This simple bilayer model, contrary to its oversimplified appearance, describes also planar superlattices, provided periodic boundary conditions are employed, where t_s and t_h correspond to half of the thicknesses of the soft and the hard phases in a superlattice sample. Uniform distribution of magnetization in the film plane of each individual layer, which is assumed to be infinitely extended, is required to guarantee this 1D model is valid.

The starting point is the Gibbs free energy density, defined as a functional of the material parameters [89, 91],

$$F = \sum_{i=1,2} (-1)^i \int_{x_0}^{x_i} F_i dx + F_0, \tag{3.1}$$

where

$$F_i = A_i \left[\dot{\theta}^2 + \dot{\phi}^2 \sin^2\theta\right] + (-1)^{i-1}\mu_0 M_i H \cos\theta + K_i \sin^2\theta. \tag{3.2}$$

For the soft layer $i = 1$, and for the hard layer $i = 2$. When referring to quantities given in the preceding paragraph, such as magnetization, subscript 1 (2) should be replaced by subscript s (h). Due to the zero temperature considered here, F is also the energy density. The abbreviations used here are $\dot{\theta} = \partial\theta/\partial x$ and $\dot{\phi} = \partial\phi/\partial x$. H is the negative of the applied field, $H = -H_{app}$, so $H > 0$ corresponds to the second quadrant part of the hysteresis loop. $F_0 = -2\nu\left(\cos\theta_+\cos\theta_- + \sin\theta_+\sin\theta_-\cos(\phi_+ - \phi_-) + 1\right)$ is the areal energy density at the interface, with θ_+, ϕ_+, θ_-, ϕ_- the polar and azimuthal

angles above and below the interface, respectively. Note θ in the soft layer is measured from the z axis, while θ in the hard layer is measured from the -z direction. The constant $\nu = |A_0|/a$, where a is the separation between the two atomic layers defining the interface. The minus sign in front of the second term in F_i is due to the AFM configuration of the whole structure, so the soft layer is antiparallel while the hard layer is parallel to the applied negative field. The equilibrium configuration of the system corresponds to the minimum of the free energy, which is determined by the stationary point $\delta F = 0$. The functional variation upon the variations $\delta\theta(x)$ and $\delta\phi(x)$ is [91]

$$\begin{aligned} \delta F &= \sum_{i=1,2}(-1)^i \left(\frac{\partial F_i}{\partial\dot{\theta}}\delta\theta + \frac{\partial F_i}{\partial\dot{\phi}}\delta\phi\right)\Big|_{x_0}^{x_i} + \sum_{i=+,-}\left(\frac{\partial F_0}{\partial\theta_i}\delta\theta_i + \frac{\partial F_0}{\partial\phi_i}\delta\phi_i\right) \\ &+ \sum_{i=1,2}(-1)^i \int_{x_0}^{x_i}\left[\left(\frac{\partial F_i}{\partial\theta} - \frac{d}{dx}\frac{\partial F_i}{\partial\dot{\theta}}\right)\delta\theta - \frac{d}{dx}\frac{\partial F_i}{\partial\dot{\phi}}\delta\phi\right]dx. \end{aligned} \tag{3.3}$$

A partial integration has been performed to obtain the first term, using the fact that variation and differentiation are interchangeable $\delta\dot{\theta} = d\delta\theta/dx$. Due to the arbitrariness of the variations $\delta\theta$ and $\delta\phi$, the integrands and the summands have to vanish, which gives the equations of motion, i.e. two Euler equations, and the corresponding boundary conditions. For the azimuthal variable ϕ, the equation of motion is [91]

$$\frac{d}{dx}\frac{\partial F_i}{\partial\dot{\phi}} = 0. \tag{3.4}$$

This equation of motion, whose explicit solution is given by [91]

$$\dot{\phi}\sin^2\theta = const., \tag{3.5}$$

can be used to simplify the boundary conditions derived from the remaining part of (3.3). If the top and bottom surfaces are free to move, the variations $\delta\phi_i$ are not zero, the corresponding boundary conditions are [91]

$$\left.\frac{\partial F_i}{\partial\dot{\phi}}\right|_{x_i} = 0,\ \left.\frac{\partial F_i}{\partial\dot{\phi}}\right|_{x_-} + \frac{\partial F_0}{\partial\phi_-} = 0,\ \left.\frac{\partial F_i}{\partial\dot{\phi}}\right|_{x_+} - \frac{\partial F_0}{\partial\phi_+} = 0. \tag{3.6}$$

Then at the two surfaces [91],

$$\dot{\phi}\sin^2\theta_i|_{x_i} = 0. \tag{3.7}$$

Except for $\theta = 0$, this gives $\dot{\phi} = 0$. Hence ϕ is a constant, which is $\pi/2$ for the in-plane case and can be chosen to be 0 in the out-of-plane case. In the case $\theta = 0$, the definition of ϕ is arbitrary; we can set $\phi = 0$. Putting this result back into the definition of F, ϕ does not appear any more and only θ remains. This results from the fact that ϕ is

only present in the exchange term. Based on this consideration, in the following only the polar angle dependence will be taken into account in the free energy. The derived equation of motion for θ is [91]

$$\frac{\partial F_i}{\partial \theta} - \frac{d}{dx}\frac{\partial F_i}{\partial \dot{\theta}} = 0 \tag{3.8}$$

with the boundary conditions

$$\left.\frac{\partial F_i}{\partial \dot{\theta}}\right|_{x_i} = 0, \left.\frac{\partial F_i}{\partial \dot{\theta}}\right|_{x_-} + \frac{\partial F_0}{\partial \theta_-} = 0, \left.\frac{\partial F_i}{\partial \dot{\theta}}\right|_{x_+} - \frac{\partial F_0}{\partial \theta_+} = 0. \tag{3.9}$$

Substituting into the explicit form of F, the boundary conditions reduce to [91]

$$\dot{\theta}|_{x_i} = 0, A\dot{\theta}|_{x_-} = \nu \sin(\theta_+ - \theta_-) = A\dot{\theta}|_{x_+}. \tag{3.10}$$

Together with the Euler equation [89, 91],

$$\ddot{\theta} + (\alpha_i/2 - \beta_i \cos\theta)\sin\theta = 0, \tag{3.11}$$

they are the main result of this chapter, with $\alpha_i = (-1)^{i-1}\mu_0 M_i H/A_i$ and $\beta_i = K_i/A_i$.

The first integral of the Euler equation is trivial to find as [89]

$$\dot{\theta} = -\sqrt{\alpha_i(\cos\theta - \cos\theta_i) + \beta_i(\sin^2\theta - \sin^2\theta_i)}. \tag{3.12}$$

Choosing the negative sign of the square root corresponds to the configuration that the deviation angle for the soft layer is larger than that of the hard layer, $\theta_1 > \theta_2$. The whole hysteretic response of the exchange spring system can be obtained by solving the equations derivable from (3.12) [89],

$$\int_{\theta_0}^{\theta_i} \frac{d\theta}{\sqrt{\alpha_i(\cos\theta - \cos\theta_i) + \beta_i(\sin^2\theta - \sin^2\theta_i)}} = x_0 - x_i, \tag{3.13}$$

with the boundary conditions at the interface, to determine the four angle parameters θ_+, θ_-, θ_1 and θ_2 (θ_0 denotes the interface angles θ_-, θ_+ for $i = 1$ or 2, respectively). Then the obtained θs can be used to calculate the average magnetization at the corresponding field. Usually this warrants numerical solution of the whole coupled boundary problem.

Although the determination of the whole hysteresis loop depends on numerical solution, the bending field can be easily found using the linearized form of the Euler equation (3.11)

$$\ddot{\theta} + (-1)^{i-1}\gamma_i^2\theta = 0, \tag{3.14}$$

with $\gamma_i^2 = (-1)^i(\beta_i - \alpha_i/2)$. We are only interested in the magnetic behaviour in the vicinity of the bending field, so we consider here the field range $2K_s/M_s < \mu_0 H <$

$2K_h/M_h$. Then these second order equations can be solved by the following piece-wise continuous function

$$\theta = \begin{cases} c_1 \cos\gamma_1(x-x_1)\csc\gamma_1 x_1, x_1 < x < x_0 \\ c_2 \cosh\gamma_2(x-x_2)\ (\cosh\gamma_2 x_2 - \sinh\gamma_2 x_2), x_0 < x < x_2 \end{cases}, \tag{3.15}$$

considering the boundary conditions for the two free surfaces. Putting this form into the interface boundary equations gives

$$\begin{aligned} \nu\cos\gamma_1 t_s \csc\gamma_1 x_1\ c_1 - (\nu\cosh\gamma_2 t_h + A_h\gamma_2\sinh\gamma_2 t_h)(\cosh\gamma_2 x_2 - \sinh\gamma_2 x_2)\ c_2 &= 0, \\ (\nu\cos\gamma_1 t_s - A_s\gamma_1\sin\gamma_1 t_s)\csc\gamma_1 x_1\ c_1 - \nu\cosh\gamma_2 t_h(\cosh\gamma_2 x_2 - \sinh\gamma_2 x_2)\ c_2 &= 0. \end{aligned}$$

To insure the solution is not trivial, the determinant of the coefficient matrix has to be zero. This gives

$$A_s\gamma_1\nu\cosh\gamma_2 t_h\sin\gamma_1 t_s + A_h\gamma_2(A_s\gamma_1\sin\gamma_1 t_s - \nu\cos\gamma_1 t_s)\sinh\gamma_2 t_h = 0, \tag{3.16}$$

which can be simplified to the implicit equation for the bending field [91]

$$A_s\gamma_1\tan\gamma_1 t_s = A_h\gamma_2(1 - \frac{A_s\gamma_1}{\nu}\tan\gamma_1 t_s)\tanh\gamma_2 t_h. \tag{3.17}$$

When $\nu \to \infty$, this reduces to $A_s\gamma_1\tan\gamma_1 t_s = A_h\gamma_2\tanh\gamma_2 t_h$, which is exactly the bending field equation for two rigidly coupled layers. When the hard layer is infinitely hard $\gamma_2 \to \infty$, the bending field obeys the inverse square law [88]

$$\mu_0 H_B = \frac{2K_s}{M_s} + \frac{A_s\pi^2}{2M_s t_s^2}, \tag{3.18}$$

which was actually confirmed in our system [40]. This equation requires that there is only one ($\gamma_1 t_s \neq n\pi$) domain-wall like structure in the bilayer for fields infinitesimally close to the bending field, which is what can be expected because multi-domain-wall configuration is usually preceded by switching events, upon increasing the applied field from the bending field. Several curves for the bending field as a function of the soft layer thickness are shown in Fig. 3.2, with different values for the interface coupling constant ν. The parameters used to get those curves at room temperature are: $M_s = 5.0 \times 10^5$ A/m, $K_s = 6.3 \times 10^3$ J/m^3 for YFe_2 and $M_h = 8.3 \times 10^5$ A/m, $K_h = 1.3 \times 10^5$ J/m^3 for $DyFe_2$. The effective anisotropy constants are derived from the room temperature coercivity through $B_c = 2K/M$.

Depending on the ratio between the hard and the soft layer thicknesses, an exchange spring magnet can exhibit different switching modes: they are exchange spring (ES), rigid magnet (RM) and decoupled magnet (DM) modes [89]. To investigate this classification, the susceptibility at the bending field, which will be discussed below, is

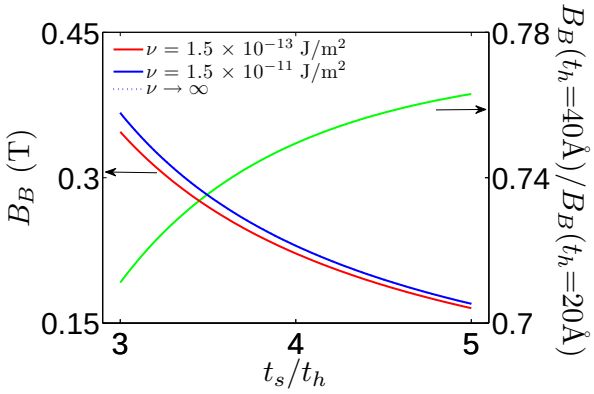

Figure 3.2: Bending field as a function of the soft layer thickness with the hard layer thickness $t_h = 20$ Å, determined from Eq. (3.17). Two values of ν are used, as shown in the graph. The bending field for infinite interface coupling, $\nu \to \infty$, is almost coincident with that obtained for $\nu = 1.5 \times 10^{-11}$ J/m^2. The green curve, whose scale is shown on the right axis of ordinates, is the ratio between the bending field values for two different hard layer thicknesses, 20 Å and 40 Å.

needed. Expanding (3.12) to 4th order in angles and taking the square root, we have [89]

$$\frac{d\theta}{\sqrt{|\theta^2 - \theta_i^2|}}\left[1 + \frac{p_i}{2}(\theta^2 + \theta_i^2)\right] = -\gamma_i dx \tag{3.19}$$

with $p_i = (\alpha_i - 8\beta_i)/12(\alpha_i - 2\beta_i)$. Integrate it over x and keep only terms to 4th order, the result is [89]

$$\begin{aligned}
\theta_- - \frac{p_1}{4 + 3p_1\theta_1^2}\theta_-(\theta_1^2 - \theta_-^2) &= \theta_1 \cos\frac{4\gamma_1 t_s}{4 + 3p_1\theta_1^2}, \\
\theta_+ - \frac{p_2}{4 + 3p_2\theta_2^2}\theta_+(\theta_2^2 - \theta_+^2) &= \theta_2 \cosh\frac{4\gamma_2 t_h}{4 + 3p_2\theta_2^2}.
\end{aligned} \tag{3.20}$$

On arriving at (3.20), the relations $\theta_-/\theta_1 = \cos\gamma_1 t_s$ and $\theta_+/\theta_2 = \cosh\gamma_2 t_h$, which follow from (3.15), are used. We want to study the response of the magnetization upon increasing the field from the bending field. The infinitesimal field increment is τ, $H \to H_B(1+\tau)$. The corresponding angles are $\theta_i \to \theta_i + \eta_i$, where the changes in angle, η_i, are higher order infinitesimal quantities. Putting those substitutions back into the 4th order equations (3.20) and neglecting terms with order higher than θ^3, such as $\eta\theta^2$ or $\eta^2\theta$, we arrive at two following equations [89]

$$\begin{aligned}
\eta_- - \eta_1 \cos\gamma_1 t_s &= \frac{\theta_1}{4}\gamma_1 t_s \sin\gamma_1 t_s \left(3p_1\,\theta_1^2 - \frac{\alpha_1\tau}{\gamma_1^2}\right) + \frac{p_1}{4}\theta_-\left(\theta_1^2 - \theta_-^2\right), \\
\eta_+ - \eta_2 \cosh\gamma_2 t_h &= \frac{\theta_2}{4}\gamma_2 t_h \sinh\gamma_2 t_h \left(-3p_2\,\theta_2^2 - \frac{\alpha_2\tau}{\gamma_2^2}\right) - \frac{p_2}{4}\theta_+\left(\theta_+^2 - \theta_2^2\right).
\end{aligned}$$

Doing the same thing for the interface boundary conditions, we have two more equations [89]

$$\begin{aligned}
& \eta_- \left(A_s^2\gamma_1^2\theta_- + \nu^2(\theta_- - \theta_+)\right) - \eta_+\nu^2(\theta_- - \theta_+) - \eta_1 A_s^2\gamma_1^2\theta_1 \\
= \; & \frac{A_s^2}{4}\tau\alpha_1(\theta_1^2 - \theta_-^2) + \frac{\nu^2}{6}(\theta_+ - \theta_-)^4 + \frac{A_s^2}{2}p_1\gamma_1^2(\theta_-^4 - \theta_1^4), \\
& \eta_-\nu^2(\theta_- - \theta_+) - \eta_+ \left(A_h^2\gamma_2^2\theta_+ + \nu^2(\theta_- - \theta_+)\right) + \eta_2 A_h^2\gamma_2^2\theta_2 \\
= \; & \frac{A_h^2}{4}\tau\alpha_2(\theta_2^2 - \theta_+^2) + \frac{\nu^2}{6}(\theta_+ - \theta_-)^4 + \frac{A_h^2}{2}p_2\gamma_2^2(\theta_+^4 - \theta_2^4). \qquad (3.21)
\end{aligned}$$

To guarantee nontrivial solution for ηs, the augmented determinant has to be zero because the determinant of the coefficients matrix is zero, which follows from the 2nd order equations. This gives the relation [89]

$$\begin{aligned}
& \tau\left[\alpha_1\left(\frac{1}{\gamma_1^2} + \frac{2t_s}{\gamma_1 \sin 2\gamma_1 t_s}\right) + \omega\alpha_2\left(\frac{1}{\gamma_2^2} + \frac{2t_h}{\gamma_2 \sinh 2\gamma_1 t_s}\right)\right] \\
+ \; & \theta_-^2\left[\frac{2(1-\omega)^3}{3} - p_1\left(2 + 3\sec^2\gamma_1 t_s + 3\gamma_1 t_s \sec^3\gamma_1 t_s \csc\gamma_1 t_s\right)\right. \\
+ \; & \left.\omega^3 p_2\left(2 + 3\,\mathrm{sech}^2\gamma_2 t_h + 3\gamma_2 t_h\,\mathrm{sech}^3\gamma_2 t_h\,\mathrm{csch}\gamma_2 t_h\right)\right] = 0. \qquad (3.22)
\end{aligned}$$

$\omega = A_s\gamma_1 \tan\gamma_1 t_s / A_h\gamma_2 \tanh\gamma_2 t_h = 1/(1 + A_h\gamma_2 \tanh\gamma_2 t_h/\nu)$, and the second equality follows from the implicit equation for the bending field (Eq. (3.17)). In the derivation, the relation $\theta_+ = \omega\theta_-$ has been used, which is derivable from the interface boundary conditions to the second order as $\nu(\theta_+ - \theta_-) = A_s\dot{\theta} = -A_s\gamma_1\theta_- \tan\gamma_1 t_s = A_h\dot{\theta} = -A_h\gamma_2\theta_+ \tanh\gamma_2 t_h$.

The magnetization component along the field direction is the average [89]

$$M_z = \frac{M_s\int_{x_1}^{x_0} dx\cos\theta - M_h\int_{x_0}^{x_2} dx\cos\theta}{x_2 - x_1} = \frac{M_s I_1 - M_h I_2}{t_h + t_s}. \qquad (3.23)$$

To second order, substituting in the explicit form of θ, the integral I_1 can be expressed as [89]

$$\begin{aligned}
I_1 &= \int_{x_1}^{x_0} dx\left(1 - \frac{\theta^2}{2}\right) = \int_{x_1}^{x_0} dx\left[1 - \frac{\theta_1^2}{2}\cos^2\gamma_1(x - x_1)\right] \\
&= t_s\left(1 - \frac{\theta_-^2}{4\cos^2\gamma_1 t_s}\right) - \frac{\theta_-^2}{4\gamma_1}\tan\gamma_1 t_s. \qquad (3.24)
\end{aligned}$$

This is actually also an expansion of the normalized magnetization for the soft layer to second order in θ at the bending field. For fields smaller than the bending field, the angle θ_- is zero and I_1 reduces to the normalized magnetization for the soft layer at saturation, t_s. Similarly, for the hard layer [89],

$$I_2 = \int_{x_0}^{x_2} dx\left[1 - \frac{\theta_2^2}{2}\cosh^2\gamma_2(x - x_2)\right] = t_h\left(1 - \frac{\theta_+^2}{4\cosh^2\gamma_2 t_h}\right) - \frac{\theta_+^2}{4\gamma_2}\tanh\gamma_2 t_h.$$

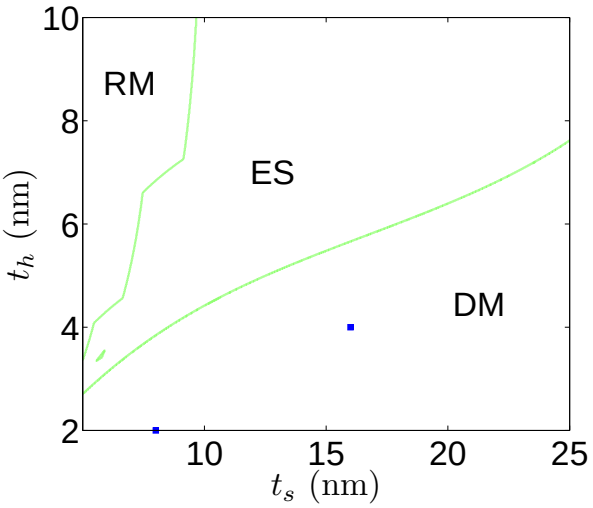

Figure 3.3: Phase diagram for $DyFe_2/YFe_2$ superlattices at room temperature determined from χ_c (Eq. (3.25)), with $\nu \to \infty$. t_s and t_h are the thicknesses of the soft and the hard layers, respectively. Exchange spring, rigid magnet and decoupled magnet are denoted as ES, RM and DM, respectively. The small island in the ES regime signifies the breakdown of the simple assumption used to differentiate between hard-dominant ($M_h t_h > M_s t_s$) and soft-dominant ($M_s t_s > M_h t_h$) superlattices. Two samples measured by MOKE (Chapter 4) are given by two blue squares.

The relative change of magnetization upon an infinitesimal increment at the bending field is [89]

$$\begin{aligned} \delta m &= \frac{\delta M}{M_s} = \frac{M_s - (t_s + t_h) M_z}{M_s} \\ &= \frac{\theta_-^2}{4 M_s} \left[M_s \left(\frac{t_s}{\cos^2 \gamma_1 t_s} + \frac{\tan \gamma_1 t_s}{\gamma_1} \right) - \omega^2 M_h \left(\frac{t_h}{\cosh^2 \gamma_2 t_h} + \frac{\tanh \gamma_2 t_h}{\gamma_2} \right) \right]. \end{aligned}$$

Then the susceptibility is given by [89, 91]

$$\begin{aligned} \chi_c = \frac{\delta M}{\delta H} = \frac{M_s \delta m}{H_B \tau} \propto \left[\alpha_1 \left(\frac{1}{\gamma_1^2} + \frac{2 t_s}{\gamma_1 \sin 2\gamma_1 t_s} \right) + \omega \alpha_2 \left(\frac{1}{\gamma_2^2} + \frac{2 t_h}{\gamma_2 \sinh 2\gamma_1 t_s} \right) \right] \\ \times \frac{M_s \left(\frac{t_s}{\cos^2 \gamma_1 t_s} + \frac{\tan \gamma_1 t_s}{\gamma_1} \right) - \omega^2 M_h \left(\frac{t_h}{\cosh^2 \gamma_2 t_h} + \frac{\tanh \gamma_2 t_h}{\gamma_2} \right)}{\frac{3 p_1}{\cos^2 \gamma_1 t_s} \left(1 + \frac{2 \gamma_1 t_s}{\sin 2 \gamma_1 t_s} \right) - \frac{3 \omega^3 p_2}{\cosh^2 \gamma_2 t_h} \left(1 + \frac{2 \gamma_2 t_h}{\sinh 2 \gamma_2 t_h} \right) + 2 (p_1 - \omega^3 p_2) - \frac{2(1-\omega)^3}{3}}. \end{aligned} \quad (3.25)$$

$\chi_c > 0$ corresponds to the exchange spring regime, where the change of magnetization due to the applied field is gradual, at the bending field. Contrary to that, the magnetization switches irreversibly in regions with $\chi_c < 0$, where the above discussed approach is not valid any more. In the case of FM coupling, the boundary between those phases is given by $\chi_c \to \infty$, because in this case only the denominator of χ_c can change sign

and the numerator of the second line in Eq. (3.25) is always greater than 0. For AFM coupling, this is not true and both the denominator and numerator determine the phase boundary. The room temperature phase diagram for our superlattices is shown in Fig. 3.3, with rigid interlayer coupling, $\nu \to \infty$. On arriving at this diagram, a simple antiparallel with the hard layer opposing to the applied field is assumed for the hard dominant geometry ($M_h t_h > M_s t_s$). Note here uniaxial anisotropy is assumed, not the relevant cubic anisotropy derived from the lattice. So the phase diagram cannot be compared directly with the experiment. It is only of qualitative significance. The same set of material parameters as used to generate Fig. 3.2 are used here.

Two data points (blue squares, details to be given in Chapter 4) are also shown in Fig. 3.3 for comparison. From the measured MOKE hysteresis loops, they belong to the ES regime. But in Fig. 3.3, they lie in the DM region. This signifies that our simple 1D, uniaxial, analytical model can only used for qualitative discussion of real, 3D, cubic exchange spring systems. In Fig. 3.3, the interface exchange coupling is assumed to be infinite, which is definitely not true. Another factor contributing to the discrepancy between theory and experimental data can be attributed to the rough material parameters used to generate Fig. 3.3. They are estimated from the room temperature coercivity using uniaxial, instead of cubic, Stoner-Wolhfarth model. Furthermore, if the coercivity is primarily determined by domain wall pinning, this estimation, even with cubic anisotropy, can give an erroneous answer. Finally, analytical model is only of qualitative significance. It can tell use the general character of exchange spring systems, but it cannot be used to make quantitative predictions. It is even worse in our case here, using uniaxial anisotropy to approximate cubic anisotropy.

Periodic boundary condition has been used to simplify the discussion. But the exact solution for the bending field can be expressed in a closed form even without the help of periodic boundary condition. Comparing the two solutions, the effect of the application of periodic boundary condition on the determined bending field can be seen. For this aim, we will reformulate the whole problem in a matrix form. Define the variable $\vartheta = (\theta, d\theta/dx)^T$. The propagation matrix for a soft layer is $\vartheta_1 = P_s \vartheta_0$,

$$P_s = \begin{pmatrix} \cos\gamma_1 t_s & \sin\gamma_1 t_s/\gamma_1 \\ -\gamma_1 \sin\gamma_1 t_s & \cos\gamma_1 t_s \end{pmatrix}. \tag{3.26}$$

The interface matrix is $\vartheta_2 = I_s \vartheta_1$

$$I_s = \begin{pmatrix} 1 & A_s/\nu \\ 0 & A_s/A_h \end{pmatrix}. \tag{3.27}$$

The total transfer matrix is

$$T_s = I_s P_s = \cos\gamma_1 t_s \begin{pmatrix} 1 - \frac{A_s\gamma_1}{\nu}\tan\gamma_1 t_s & \frac{A_s}{\nu} + \frac{\tan\gamma_1 t_s}{\gamma_1} \\ -\frac{A_s\gamma_1}{A_h}\tan\gamma_1 t_s & A_s/A_h \end{pmatrix}. \tag{3.28}$$

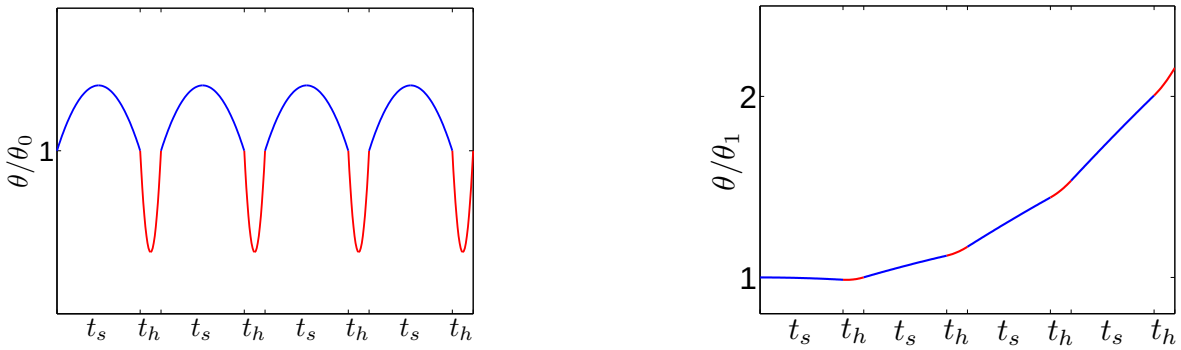

Figure 3.4: Schematic profile of the distribution of angle along the x direction, showing the difference between the application of the periodic (left) and non-periodic (right) boundary conditions. The relatively large change in amplitude for the hard phase is caused by this particular choice of parameters.

For the hard layer,

$$P_h = \begin{pmatrix} \cosh\gamma_2 t_h & \sinh\gamma_2 t_h/\gamma_2 \\ -\gamma_2 \sinh\gamma_2 t_h & \cosh\gamma_1 t_s \end{pmatrix}, I_h = \begin{pmatrix} 1 & A_h/\nu \\ 0 & A_h/A_s \end{pmatrix}, \tag{3.29}$$

and

$$T_h = \cosh\gamma_2 t_h \begin{pmatrix} 1+\frac{A_h\gamma_2}{\nu}\tanh\gamma_2 t_h & \frac{A_h}{\nu}+\frac{\tanh\gamma_2 t_h}{\gamma_2} \\ \frac{A_h\gamma_2}{A_s}\tanh\gamma_2 t_h & A_h/A_s \end{pmatrix}. \tag{3.30}$$

For a bilayer, starting from the soft layer, the final angle θ_f is related to the initial angle $\theta_i = (\theta_0, 0)^T$ through $\theta_f = T\theta_i$ with $T = P_h T_s$. The boundary condition at the free surface $d\theta/dx = 0$ corresponds to

$$T_{2,1} = \cosh\gamma_2 t_h \cos\gamma_1 t_s \left(\gamma_2\left(1-\frac{A_s\gamma_1}{\nu}\tan\gamma_1 t_s\right)\tanh\gamma_2 t_h - \frac{A_s}{A_h}\gamma_1\tan\gamma_1 t_s\right) = 0,$$

from which the implicit equation for the bending field (Eq. (3.17)) follows. The eigenvalue equation will not change if we consider the hard layer first.

For our multilayer samples, with N hard-soft bilayers, we can start from the first soft layer to get the transfer matrix $T = I_h^{-1}(T_h T_s)^N$. Actually, here the matrix I_h^{-1} can be neglected for our purpose, because of the proportionality of the two differentials on the two sides of an interface, Eq. (3.10). The nonsingular product matrix $T_h T_s$ can be diagonalized as $\cosh\gamma_2 t_h \cos\gamma_1 t_s \Lambda = Q^{-1}(T_h T_s)Q$. $\Lambda = (\lambda_1, \lambda_2)$ is a diagonal matrix with $\lambda_1 = \alpha - \beta$ and $\lambda_2 = \alpha + \beta$.

$$\begin{aligned} \alpha &= 1 + \frac{A_h\gamma_2}{\nu}\tanh\gamma_2 t_h - \frac{A_s\gamma_1}{\nu}\tan\gamma_1 t_s \\ &+ \frac{1}{2}\left(\frac{A_h\gamma_2}{A_s\gamma_1} - \frac{A_s\gamma_1}{A_h\gamma_2} - \frac{A_h A_s\gamma_1\gamma_2}{\nu^2}\right)\tan\gamma_1 t_s \tanh\gamma_2 t_h, \end{aligned} \tag{3.31}$$

$$\beta = \sqrt{\alpha^2 - \sec^2 \gamma_1 t_s \mathrm{sech}^2 \gamma_2 t_h}. \tag{3.32}$$

The matrix Q has the form

$$Q = \begin{pmatrix} A_s\nu(\xi+\beta)/\Delta & A_s\nu(\xi-\beta)/\Delta \\ 1 & 1 \end{pmatrix}. \tag{3.33}$$

$$\xi = \left(\frac{A_s\gamma_1}{\nu} + \frac{1}{2}\left(\frac{A_h\gamma_2}{A_s\gamma_1} + \frac{A_s\gamma_1}{A_h\gamma_2} + \frac{A_hA_s\gamma_1\gamma_2}{\nu^2} \right) \tanh \gamma_2 t_h \right) \tan \gamma_1 t_s, \tag{3.34}$$

and

$$\Delta = A_s\gamma_1\nu \tan \gamma_1 t_s - A_h\gamma_2\nu \tanh \gamma_2 t_h + A_s\gamma_1 A_h\gamma_2 \tan \gamma_1 t_s \tanh \gamma_2 t_h. \tag{3.35}$$

Carrying out the matrix product, the boundary condition corresponds to $\Delta = 0$, which is exactly the same equation as shown in Eq. (3.16), though there are two other solutions with $t_s\gamma_1 > \pi/2$, indicating the formation of domain walls. Note here t_s and t_h are the actual thicknesses, not the half of the thicknesses of the individual layers. Except for this difference, the form of Eq. (3.17) is very general for exchange coupled superlattices. The result remains the same if we consider the hard layer first. The main difference between the above geometry and the periodic geometry is illustrated in Fig. 3.4. Roughly, the periodic boundary condition is more suited for the description at high fields where the exchange springs are tightly squeezed, while the non-periodic boundary is more appropriate for exchange springs near zero field.

Chapter 4

Room temperature magneto optic exchange springs

Increasing the temperature is the easiest way to change the ratio of the soft layer anisotropy to that of the hard layer, because the anisotropy of $DyFe_2$ is very sensitive to temperature, while YFe_2's anisotropy is almost constant over temperature. Previously, the low temperature property of a series of 1:1 superlattices with different thick layer thicknesses was extensively studied using a VSM [40]. It was found that the bending field is proportional to the inverse square of the soft layer thickness ($B_B \propto 1/t_s^2$). In this chapter, we detail the room temperature behaviour of 1:4 soft-dominant superlattices, and effects originating from the reduced hard layer anisotropy, using MOKE and 1D computer simulation. A clear deviation from the inverse square law is observed. This can be explained by a transition to a new switching mode, traceable to the reduced hard phase anisotropy. Both analytical and computer simulations support this explanation.

4.1 Measurements on YFe_2 and $DyFe_2$ films

Before examining the superlattice samples, the magneto optic response of the two building blocks, pure $DyFe_2$ and YFe_2 films, should be determined. YFe_2 is the nominal soft phase, whose coercivity is small. The induced strain in YFe_2 is negligible. So there is no magneto-elastic contribution to the anisotropy. The easy axis for an YFe_2 film is always $[\bar{1}11]$, independent of temperature. Due to the very small intrinsic anisotropy, the hard axis ($[1\bar{1}2]$) behaviour is similar to that of the easy axis. The coercivity of pure YFe films is independent of temperature in the range 4.2 K $< T <$ 290 K [2]. This temperature independence of anisotropy is characteristic of many 3d transition metals, whose anisotropy is determined primarily by the weak spin-orbit interaction. A typical MOKE hysteresis loop for fields applied along the easy axis can be seen in

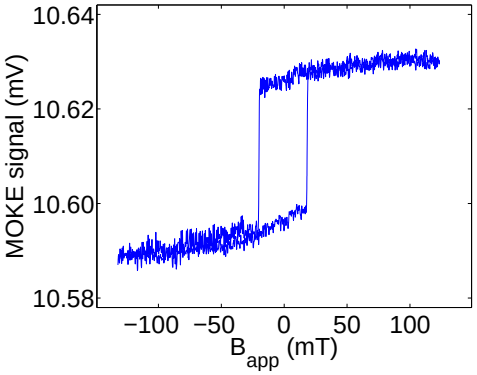

Figure 4.1: Room temperature easy axis ($[\bar{1}11]$) MOKE hysteresis loop for a 1000 Å YFe_2 film.

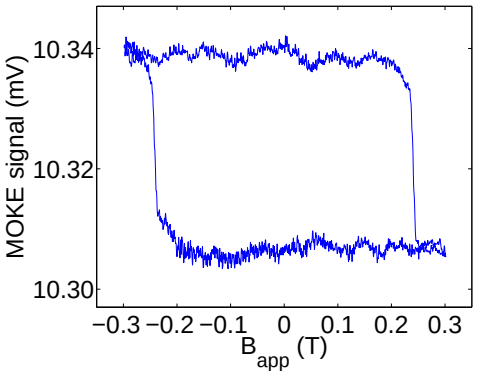

Figure 4.2: Room temperature easy axis ($[\bar{1}10]$) MOKE hysteresis for a 2000 Å $DyFe_2$ film.

Fig. 4.1.

$DyFe_2$ is the hard phase of our superlattice samples. This ideally entails a very large coercivity. At low temperatures, this is provided by the large crystal fields, giving rise to very large anisotropy constants. However, the latter are very sensitive functions of temperature, and at room temperature the coercivity of a pure $DyFe_2$ films is less than 0.5 T. Another complication comes from the magneto-elastic contribution, which induces a transition of the easy axis from $[00\bar{1}]$ to $[\bar{1}10]$ about 100 K. An easy axis hysteresis loop of a 2000 Å $DyFe_2$ film at room temperature can be seen in Fig. 4.2. When the applied field is rotated away from the easy axis, the coercivity increases, so even at the largest available field for our electromagnet, $\sim$ 0.35 T, the hard axis magnetization curve cannot be saturated, so the hard axis hysteresis is not shown here. Note also the sense of switching for $DyFe_2$ is reversed, in contrast to YFe_2, which is due to $DyFe_2$'s negative Kerr rotation [71].

When the film thickness is increased to 4000 Å, the MOKE hysteresis loop exhibits strange behaviour before switching (Fig. 4.3). This cannot be observed in the corresponding VSM measured loop (Fig. 4.4) for a film with the same thickness. It is possible that this strange gradual change of MOKE signal is caused by a slow rotation of magnetization into the film plane, given that at room temperature the actual easy axis for a 4000 Å thick $DyFe_2$ film is $\sim 14^\circ$ out of plane, above the $[\bar{1}10]$ axis [30]. In this case, both the longitudinal and the polar components contribute to the measured MOKE intensity, as discussed in Chapter 2. However, the same behaviour does not occur when the thickness is increased to 8000 Å, where the typical square loop of an easy axis is observed, similar to that shown in Fig. 4.2. This behaviour may be due to the competition between the magneto-elastic, demagnetization and intrinsic crystalline anisotropy: When the film is thin enough, the demagnetization energy is

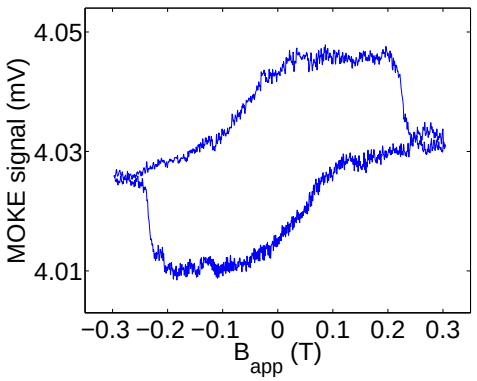

Figure 4.3: Room temperature easy axis ([$\bar{1}$10]) MOKE hysteresis loop for a 4000 Å $DyFe_2$ film.

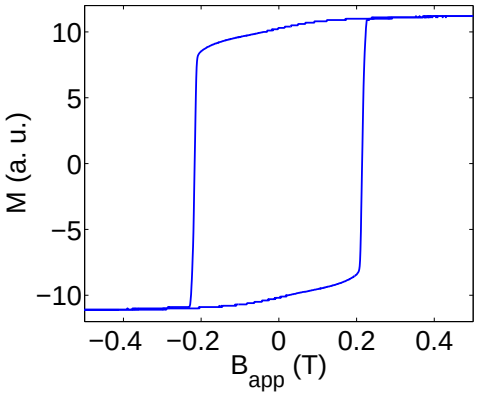

Figure 4.4: Room temperature easy axis ([$\bar{1}$10]) VSM hysteresis loop for a 4000 Å $DyFe_2$ film.

strong enough to pull the magnetization almost into the film plane, so the out-of-plane component is reduced. But if the film thickness is increased to a very large value, then the magneto-elastic interaction will become significant, prohibiting the appearance of an out-of-plane component of the magnetization. Only at intermediate values does the crystalline anisotropy give rise to a measurable out-of-plane component.

As is well known, the coercivity of a film can be dependent on its thickness, due to either surface anisotropy or domain wall pinning. The coercivity of our films does depend on thickness (Fig. 4.5). If this dependence is caused by fuzzy domain wall pinning, the increase of coercivity upon decreasing thickness means that the size of the pinning centers is greater than the domain wall width [92], which is not an unreasonable assumption for $DyFe_2$. The same domain-pinning argument for YFe_2 does not hold, because of the very wide domain walls, resulting from the small anisotropy. If the same mechanism is postulated to be responsible for the similar increase in coercivity with decreasing film thickness, mechanisms other than domain wall pinning are needed. For an ideal $DyFe_2$ film, 1D OOMMF simulations show that the coercivity is independent of the film thickness. So in order to account for the observed thickness dependence, deviations from ideal behaviour have to be sought. For example, the thickness-dependent strain relaxation is a probable candidate, if we assume that the MBE superlattices are single crystals. Due to the small magneto-elastic constant of YFe_2, magneto-elastic effect here is negligible, but the change of coercivity is also very small. Of course, in real samples, the effects of defects and island growth for the first $\sim$ 300 Å of the films have to be taken into account [25]. Actually, the decrease of the coercivity for a 500 Å $DyFe_2$ film (Fig. 4.5), may be attributable to the island growth for this very thin film. Of course, the effect of domain wall pinning in the consideration of coercivity cannot

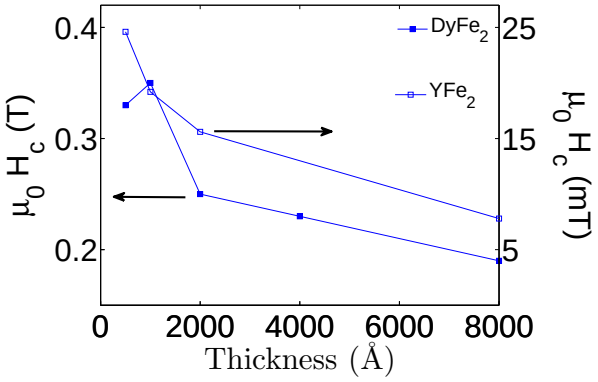

Figure 4.5: Thickness dependence of the coercivity of pure YFe_2 and $DyFe_2$ films. Two arrows point to the two scales for $DyFe_2$ and YFe_2, respectively.

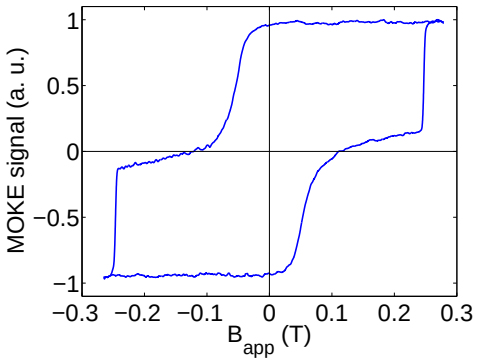

Figure 4.6: Room temperature easy axis MOKE hysteresis loop for sample SA.

be ruled out, especially at high temperatures.

4.2 Soft dominant superlattices

Two 1:4 YFe_2 dominant superlattice samples were measured using MOKE. The room temperature hysteresis loop for the first superlattice sample [$DyFe_2$ 45 Å /YFe_2 180 Å] $\times$ 18 (sample SA) can be seen in Fig. 4.6, where the formation of a reversible exchange spring occurs before irreversible switching at ~ 0.25 T. Additional measurements were performed on another MBE grown [$DyFe_2$ 20 Å/YFe_2 80 Å] $\times$ 40 superlattice (sample SB) and the corresponding result is presented in Fig. 4.7. To prove that the formation of exchange spring is reversible, the minor loops for fields smaller than the nucleation field have been performed (Fig. 4.7, red curves). The hysteresis is negligible within the experimental error limit. The exchange spring behaviour can be regarded as reversible and ideal. The same conclusion can also be drawn from the VSM loops shown in Fig. 4.7. Note that the switching field $B_c \sim 0.25$ T is close to the coercivity of pure $DyFe_2$ films at room temperature. For pure $DyFe_2$ film of 4000 Å thickness, a transition from in-plane to out-of-plane of the direction of the magnetization is observed (Fig. 4.3), but no such transition has been observed in superlattices. This can be explained by the demagnetization effect, since the $DyFe_2$ thickness is thin and the stacking of $DyFe_2$ and YFe_2 is planar. Another possible reason is the exchange coupling of $DyFe_2$ magnetization to YFe_2 magnetization. What is worth noting here is that the magnetization of YFe_2 is always in the film plane.

As noted earlier, the variation of the bending field, with the soft layer thickness, has

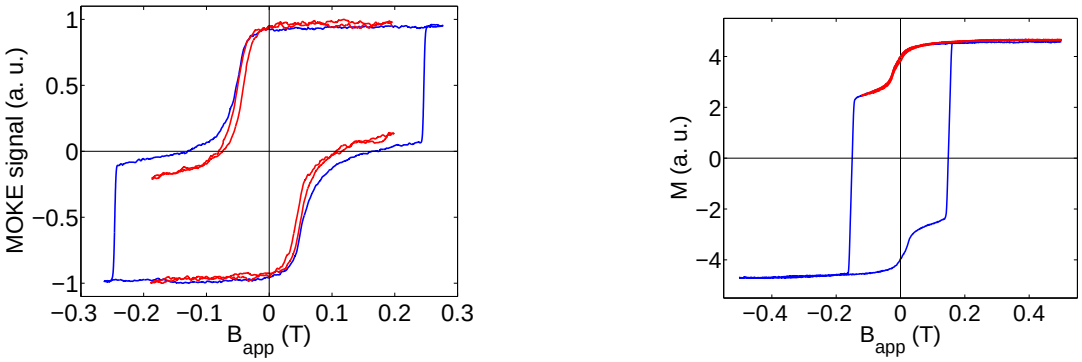

Figure 4.7: Room temperature easy axis MOKE (left) and VSM (right) major (blue) and minor (red) hysteretic loops for sample SB.

already been studied in the same system at cryogenic temperatures. It was found that the relationship $B_B \propto 1/t_s^2$ agrees very well with the experimental data, for a series of 1:1 superlattices [40], where t_s is the soft layer thickness. This $1/t_s^2$ dependence is a micromagnetic analog to the $1/L^2$ dependence of the energy levels of electrons confined to a cube of volume L^3 [93, 94]. Using the exchange field given in Ref. [40], the bending fields are predicted to be 0.9 T (SA) and 4.1 T (SB). However, these figures are unrealistic, given that they are larger than measured coercivity at room temperature. Indeed, the bending field from MOKE measurements at room temperature is found to be $B_B = 32$ mT (SA) and $B_B = 38$ mT (SB), roughly double the room temperature coercivity of pure YFe_2 films. Note that the bending field does increase with decreasing YFe_2 thickness, but the inverse square law is not obeyed. Clearly, the assumptions of infinitely hard and infinitely soft layers are not valid at room temperature.

A reasonable model at room temperature must include the finite anisotropy of both layers. Here we use the continuum model [89, 90, 91], developed to study the ferromagnetic exchange spring systems, to determine the bending field in soft-dominant superlattices. On the assumption that both the intra-layer exchange coupling constants for hard and soft layers are identical (A), the equation for the bending field of a superlattice with rigid inter-layer antiferromagnetic coupling is found to be

$$\gamma_s \tan \frac{t_s \gamma_s}{2} = \gamma_h \tanh \frac{t_h \gamma_h}{2}, \tag{4.1}$$

where $\gamma_s = \sqrt{(M_s B_B - 2K_s)/2A}$, $\gamma_h = \sqrt{(M_h B_B + 2K_h)/2A}$, and with t, K and M representing the thickness, anisotropy and saturation magnetization, respectively. The subscripts s and h refer to the soft and the hard layers. The same equation has been used widely in the discussion of exchange spring systems [94, 93]. A detailed derivation of this equation was given in Chapter 3.

For hard-dominant superlattices, the prototype of which is the 1:1 superlattices,

the s and h subscripts must be interchanged, because the applied field is now opposite to the hard moment. In the latter configuration, the applied field has to overcome the hard anisotropy, instead of the soft anisotropy, in order to set up an exchange spring. Generally speaking, if the thickness of the hard layer is larger than the corresponding domain wall width $\delta_h = \pi\sqrt{A/K_h}$, $t_h \gg \delta_h$, the hyperbolic tangent function is constant to the first order approximation. Expanding the tangent function to first order and solving for B_B, the expression for the bending field of a soft dominant sample is readily obtainable

$$B_B = \frac{2K_s}{M_s} + \frac{4M_h A}{M_s^2 t_s^2} + \frac{4\sqrt{AK_h}}{M_s t_s}. \tag{4.2}$$

For the soft-dominant superlattices considered here $t_s > t_h \gg \delta$, the third term dominates. However for hard-dominant superlattices the main contribution comes from the second term, with a negligible correction from the third term which is now proportional to the small soft layer anisotropy K_s (remember subscripts $s \leftrightarrow h$ have to be interchanged for hard-dominant superlattices). If the hard layer anisotropy decreases, thereby increasing δ_h and decreasing $t_h\gamma_h \to 0$, then Eq. (4.2) is no longer valid anymore and the appropriate solution to (4.1) is now

$$B_B = \frac{2(K_s\tau + K_h)}{M_s\tau - M_h}, \tag{4.3}$$

where $\tau = t_s/t_h$ is the normalized soft layer thickness. This formula approximates our superlattices at room temperature with reduced anisotropies. For the 1:4 hard-soft layer ratio, the normalized soft thickness is a constant $\tau = 4$. Consequently, the bending field is constant, in reasonable agreement with experiment. In passing, we note that the inverse square law can be regained, simply by letting $K_h \to \infty$ and $K_s \to 0$ in Eq. (4.1).

For the above theoretical analysis, the magnetic configuration at remanence, i.e. whether it is the soft or hard phase that is opposing to the applied (negative) field, is very important. The remanent state can be obtained by energy consideration. Suppose the two phases are parallel at high fields. Subsequently, on decreasing the applied field, one phase will switch to be antiparallel to the applied field. But to realize this switching, there is an energy barrier to be overcome. This energy barrier corresponds to the energy difference between the parallel and perpendicular configurations between the two phases, if the coherent rotation demagnetization process holds. We find it is

$$M_j N_j B + N_j K_j + \frac{A_i}{a^2(N_s + N_h)} \tag{4.4}$$

or equivalently,

$$M_j t_j B + t_j K_j + \frac{A_i}{(t_s + t_h)}, \tag{4.5}$$

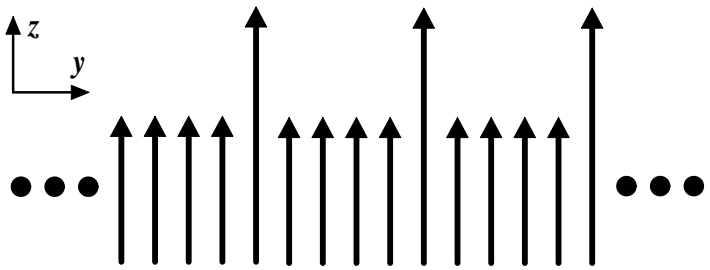

Figure 4.8: Schematic representation of the 1D spin configuration for $DyFe_2/YFe_2$ 1:4 superlattices. y direction is along the film normal and the applied field is in the x-z plane and parallel to the easy z axis. The large and small arrows denote the magnetic moments of $DyFe_2$ and YFe_2 atomic layers respectively. The actual orientation of those moments is field dependent. What is shown here is only valid at high fields. Black dots denote the omitted repeats of the $DyFe_2/YFe_2$ bilayer structure.

where a is the lattice constant, which has been chosen to be identical for the two phases. M_j, K_j and A_i are the magnetization, anisotropy constant and interface coupling constant, respectively. N_j corresponds to the number of atomic layers in the j phase. The subscript j can be either s or h, corresponding to the soft or hard phase. The absence of energy terms corresponding to the intra-layer exchange coupling is caused by our assumption on the perpendicular configuration of the two phases. Under this assumption, there is no continuous rotation in both phases, different to the case in a domain wall. The zero of this energy barrier gives an estimate of the threshold field for the switching to happen. It is

$$B_t = -\frac{A_i}{M_j(t_s + t_h)t_j} - \frac{K_j}{M_j} \tag{4.6}$$

Remember here $A_i < 0$. If the hard phase anisotropy K_h is very large, then the corresponding threshold for the hard phase is negative. Hence it is the soft phase that switches first and the remanent state has the hard phase opposing to the applied negative field, different to what we have discussed above for soft dominant samples. However, if both K_h and K_s are negligible compared to the first term, then the phase with the larger thickness-weighed magnetization, $t_j M_j$, will switch first. For soft dominant superlattices at room temperature, this leaves the soft phase to resist the applied coercing field, consistent with the picture used for the discussion of the bending field for a soft dominant sample. A similar energy consideration could be used to determine the threshold field for the transition from the perpendicular to antiparallel states, as in a spin-flop transition. The simple energy arguments are supported by the computer simulation presented in the next section.

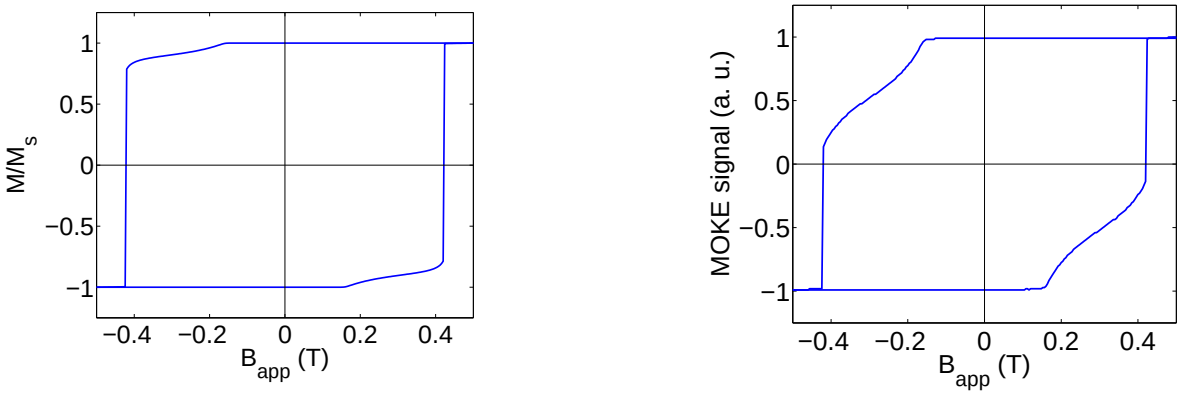

Figure 4.9: Simulated magnetic easy axis hysteresis loop (left) and MOKE signal (right) for sample SA at room temperature, with the applied field ranging from −0.5 T to 0.5 T. The difference between the magnetic and MOKE hysteresis loops is due to the surface sensitivity of MOKE: exchange springs form mostly in the top semi-free YFe_2 layer, as shown in Fig. 4.11.

4.3 Computer simulation

As discussed in Chapter 3, there are a variety of methods that can be used to describe the demagnetization process. Here we adopt the 1D model which has been used to model exchange spring systems successfully [86, 87]. The whole superlattice is treated as composed of many layers that interact with each other. The spacing between two layers can be chosen to be the lattice constant. Also the assumption of the uniformity of the spin distribution in the film plane is made, upon which the magnetic moment of an individual layer can be represented by a single spin variable so that spin depends only on the y variable with x-z plane as the film plane. A simple schematic illustration for this 1D model can be seen in Fig. 4.8.

The total energy density E of the system, or the free energy at zero temperature $T = 0$, is given by

$$E = -\sum_{i=1}^{N-1}\left(\frac{A_{i,i+1}}{d^2}\right)\mathbf{m}^i\cdot\mathbf{m}^{i+1} - \sum_{i=1}^{N}K_i\left(a_z^i\right)^2 - \sum_{i=1}^{N}\left(\mathbf{B}+\mathbf{b}^i\right)\cdot\mathbf{m}^i M^i, \tag{4.7}$$

where M^i is the magnetization of the ith atomic layer, $\mathbf{m}^i$ is the normalized magnetic moment vector $\mathbf{m}^i = \mathbf{M}^i/M^i$ with $\mathbf{M}^i$ the magnetization vector, and d is the inter-layer separation. K_i denotes the first anisotropy constant for the uniaxial anisotropy approximation used here and $A_{i,i+1}$ is the exchange coupling constant between layers i and $i+1$. $\mathbf{B}$ is the externally applied field, while $\mathbf{b}^i$ represents the demagnetizing field of a thin layer. Here we simply choose it to be $\mathbf{b}^i = -\mu_0 M^i \mathbf{m}_y^i$, which is an approximation valid in the long wavelength limit $pD \ll 1$, where D is the film thickness

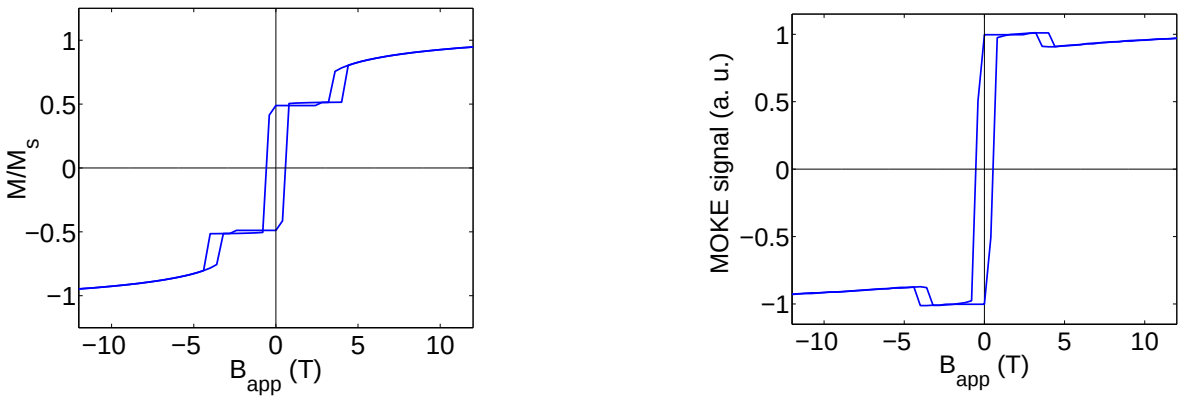

Figure 4.10: Simulated easy axis hysteresis loop (left) and MOKE signal (right) for sample SA at room temperature, with the applied field ranging from −12 T to 12 T.

and p is the component of the spin wave wave vector parallel to the film plane [87]. With the energy given by (4.7) the equation of motion for the system is

$$\frac{d\mathbf{m}^i}{dt} = -\gamma \left(\mathbf{m}^i \times \mathbf{B}_{eff} + \alpha \, \mathbf{m}^i \times (\mathbf{m}^i \times \mathbf{B}_{eff}) \right), \tag{4.8}$$

in which γ is the gyromagnetic ratio, α is the damping factor for the material and $\mathbf{B}_{eff}$ is the effective field acting on the moment $\mathbf{m}^i$ defined by $\mathbf{B}_{eff} = -\partial E/\partial \mathbf{M}^i$. This equation is exactly the LLG equation given in Chapter 1, extended to a chain of coupled spins. For the magnetization process, we set the damping α to a very large value compared to the physical value, because the numerical value of α and also that of γ which we set to $\gamma = 2.92 \times 10^{10}$ Hz/T, is unimportant for the simulation of magnetization, what matters is the ratio between them which determines the damping time. Other parameters used in the computation are: $A_{i,i+1} = 1.5 \times 10^{-11}$ J/m for the intra-layer exchange and $A_{i,i+1} = -1.5 \times 10^{-11}$ J/m for the inter-layer exchange [38], $M_s = 4.9 \times 10^5$ A/m and $K_s = 10^2$ J/m^3 for magnetically soft YFe_2 layers, while $M_h = 7.6 \times 10^5$ A/m and K_h =7.0 $\times$ 10^5 J/m^3, which is only 1/4 of the K_1 value from [23, 22], for magnetically hard $DyFe_2$ layers. The layer separation is approximately the lattice constant $d = 7.5$ Å.

For the MOKE simulation, we need more parameters pertaining to the optical properties of the substances considered. For YFe_2 the diagonal part of the conductivity tensor was set at $\sigma_{xx} = (2.5 + 1.3i) \times 10^{15}$ s^{-1} and the non-diagonal one at $\sigma_{xy} = (0.5 + 3.2i) \times 10^{13}$ s^{-1} [95]. For $DyFe_2$ those parameters are not available, so the conductivity for $CeFe_2$ is used instead for it: $\sigma_{xx} = (1.8 + 1.1i) \times 10^{15}$ s^{-1} and $\sigma_{xy} = (-0.4 + 0.6i) \times 10^{13}$ s^{-1} [95]. Those components of the conductivity tensor can be related to the dielectric tensor via the relation $\tilde{\epsilon} = \epsilon_0(1 - 4\pi\tilde{\sigma}/i\omega)$. The magneto-optical constants deduced from them are $q_s = -(0.6 + 1.0i) \times 10^{-2}$ for YFe_2 and $q_h = (0.5 - 3.6i) \times 10^{-3}$ for $DyFe_2$. Actual values of the dielectric constants are not important for the determination of the

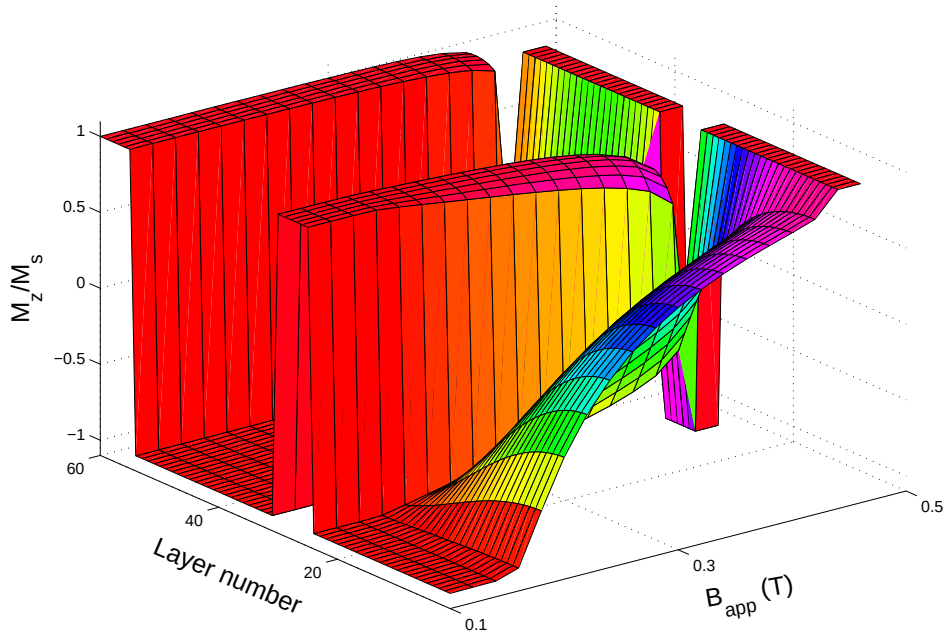

Figure 4.11: The depth distribution of z ($[\bar{1}10]$) magnetic moments for the first 60 atomic layers with field parallel to z. For the remaining layers, a repeat of this pattern is found, but with reduced amplitude. The 60 atomic layers include two bilayers, each containing 24 YFe_2 and 6 $DyFe_2$ atomic layers.

shape of the MOKE hysteresis, and the variation of them really affects only the reflected intensity. The incident angle used here is 30°; the designed value for the experimental setup.

The matrix of coupled ordinary differential equations (4.8) can be solved numerically, using the Runge-Kutta method. The program and code developed in Ref. [96], for a stiff system, was applied to the problem in hand. An evolution time of ~ 5 ns was found to yield stable configurations. Once the equilibrium magnetization is obtained, the transfer matrix method [67, 68, 69, 66] can be used to calculate the reflected MOKE intensity, layer by layer. The resultant room temperature bulk hysteresis loop can be seen in Figs. 4.9 and 4.10, together with the simulated MOKE signal. The difference between the bulk magnetization and the MOKE signal is due to the surface sensitivity of MOKE, which probes only ~ 20 nm of the top few layers. In the simulation, it was found that the evolution time needed for MOKE is longer than that for the magnetization, hence MOKE is more sensitive to the relative spin configuration of the top layers, due to its surface sensitive character. This gives rise to the difference observed both experimentally (Fig. 4.7) and theoretically (Fig. 4.9) between MOKE and bulk hysteresis loops, because the exchange springs nucleate mostly in the top YFe_2 layer and MOKE is very sensitive to the top several $DyFe_2/YFe_2$ bilayers. The bulk mag-

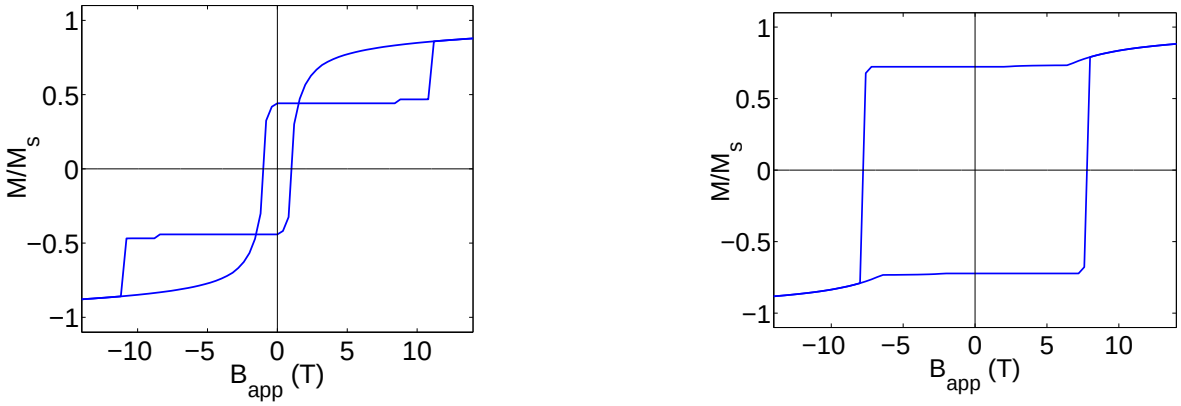

Figure 4.12: Simulated easy axis hysteresis loops for [$DyFe_2$ 45 Å/YFe_2 180 Å] × 18 (left) and [$DyFe_2$ 180 Å/YFe_2 45 Å] × 18 (right). The anisotropy constant at T = 200 K was used in this simulation.

netization is a simple average over the whole sample, so the change in signal due to exchange spring formation in the top several layers is very small. The distribution of angle of the atomic layer's moment relative to the easy axis can be seen in Fig. 4.11. It is easy to see that there is a propagation of domain wall from the soft phase into the hard phase. For comparison, the simulated hysteresis loops for different configurations are also presented in Fig. 4.12, with the anisotropy for $DyFe_2$ corresponding to a temperature of 200 K.

The results in Fig. 4.9 reveal a simple exchange spring formation in soft-dominant AFM coupled superlattices, in fields exceeding B_B. But in large positive fields, the stable configuration is that of the AFM state with the soft YFe_2 layers pointing parallel to the applied field. This AFM state is retained on decreasing the field to zero; the remanent state with positive M. On decreasing the field to negative values, the bending field B_B is reached and exchange springs are set up in the soft YFe_2 layers. Finally, on decreasing the field still further irreversible switching occurs, involving the simultaneous switching of both the hard and the soft phases, favoring again the AFM state again but now in the opposite direction. The qualitative agreement between the experiment and the theory is good. The small discrepancies could be due to various factors. For example, (i) the room temperature easy axes of $DyFe_2$ and YFe_2 are $[1\bar{1}0]$ and $[\bar{1}11]$, respectively, not parallel to each other, (ii) uncertainties in the chosen anisotropy values, (iii) slight misalignment of the applied field with respect to the easy axis when doing the measurement, and (iv) temperature effects, which are not included in our simple model. Nevertheless, room temperature effects, in principle, can be modeled by a random field with the help of the fluctuation-dissipation theorem, as discussed in Chapter 1. Furthermore, within this 1D model, the ratio between the two simulated

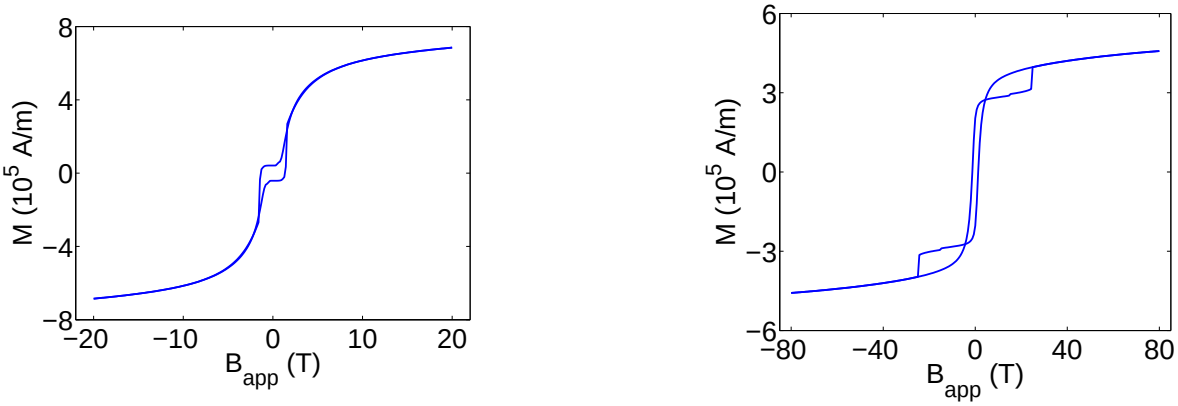

Figure 4.13: Simulated easy axis hysteresis loops for [$DyFe_2$ 40 Å/YFe_2 160 Å] × 20 superlattice at 380 K, with increased magnetization ($4M_h$, left) and anisotropy ($10K_h$, right) for the hard phase. The stabilization effect for the hard phase of those increased values is obvious.

bending fields for SA and SB is found to be ~ 2, a slightly larger value than the experimental result of 1.2 for the two superlattices considered. However, on reducing the hard anisotropy still further, a ratio ~ 1 can be obtained. Finally, the quantitative difference between simulation and experiment is the magnetization value just before the occurrence of switching: one above while the other below zero. A reduced exchange coupling constant for both phases or increased anisotropy of the hard phase can be used to reconcile this difference.

As stated in the preceding section, the deviation from the well established $1/t_s^2$ law for the bending field can be traced to the reduced hard anisotropy or magnetization. This assertion can be verified by the computer simulation. Two figures in Fig. 4.13, one with increased hard magnetization and the other with increased hard anisotropy constants, serve to demonstrate this point clearly. The simulated results are obtained using OOMMF, taking into account of the cubic nature of our system. Obviously, both graphs show that with the increased value, the hard phase remains parallel to the positive field direction and the soft phase starts to rotate first. Additionally, OOMMF simulation gives the bending field for a series of superlattice 1:4 samples of various thickness at 100 K, with field along $[00\bar{1}]$. The $1/t_s^2$ law is obeyed. But at 380 K, for fields along the easy axis $[\bar{1}10]$, clear deviations can be observed (Fig. 4.14). Even though the data points with the soft layer thickness (t_s) between 80 Å and 200 Å can still be fitted by a straight line on a log-log plot, the slope is not -2, as appropriate for the $1/t_s^2$ law. It is -0.66, as shown in Fig. 4.14. Actually, a transition from -2 to -1 for the slope is already predicted in Eq. (4.2). The exact dependence of the bending field on t_s cannot be described by a simple power law, because in Eq. (4.2) there are

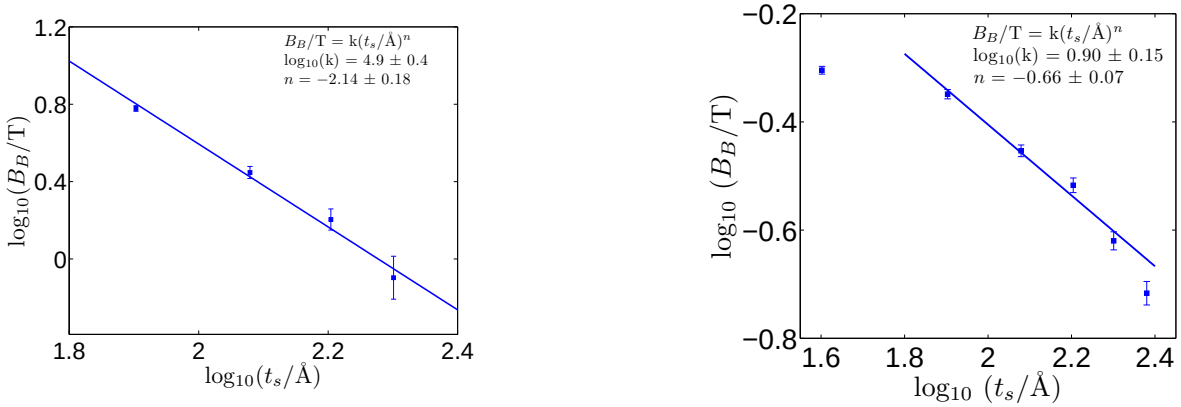

Figure 4.14: Simulated bending fields for a series of [$DyFe_2$ x Å/YFe_2 $4x$ Å] × N superlattices at 100 K (left) and 380 K (right), with field along the corresponding easy axes [00$\bar{1}$] and [$\bar{1}$10] respectively. For 100 K, x = 20, 30, 40, 50 and N = 40, 27, 20, 16, respectively. Two additional samples, [$DyFe_2$ 10 Å/YFe_2 40 Å] × 80 and [$DyFe_2$ 60 Å/YFe_2 240 Å] × 13, are also considered for 380 K. At 100 K, the $1/t_s^2$ law fits the data very well. The corresponding fitted parameters are given along with the data points. However, deviations from the $1/t_s^2$ law are clearly observable in the 380 K data. Especially, the exponent obtained from a fitting to the four data points with x = 20, 30, 40, 50 is −0.66, instead of −2. The whole set of data points at 380 K cannot be fitted by a linear function.

three terms contributing to the bending field, each with a different power of t_s. The data in Fig. 4.14 demonstrates clearly that violation of the $1/t_s^2$ law is caused by the high-temperature switching mode transition.

4.4 Summary

The room temperature magnetic properties of thin YFe_2 and $DyFe_2$ layers have been studied by MOKE. It is found that the coercivity of both $DyFe_2$ and YFe_2 films depends on the film thickness. For the thinnest films measured, the coercivity is $B_c \sim 0.3$ T and $B_c \sim 25$ mT for $DyFe_2$ and YFe_2, respectively. Those values are taken to be the intrinsic coercivities of thin MBE $DyFe_2$ and YFe_2 films. For a thick $DyFe_2$ film, a deviation from the ideal easy axis behaviour is observed, with the applied field along the in-plane nominal easy axis, [$\bar{1}$10]. This deviation can be explained by the $\sim 14°$ out-of-plane angle formed by the direction of magnetization at zero field.

YFe_2 dominant superlattice samples composed of alternating hard and soft layers have been measured. Clear exchange spring behaviour is observed, before the occurrence of switching. 1D computer simulations give qualitatively similar results. It has

been shown that the bending field varies only slowly with the soft layer thickness, contradicting the $B_B \propto 1/t_s^2$ law obeyed in 1:1 superlattices at low temperature. This discrepancy can be explained in terms of the reduced hard layer anisotropy K_h, using an analytical model. OOMMF simulations reveal that the reduced magnetization of the hard phase can also result in the observed transition in coercivity from negative to positive. In fact, this transition of switching mode is deemed to be the main cause behind the deviation from the $1/t_s^2$ law. In the theoretical derivation of the $1/t_s^2$ law [97], an infinite anisotropy was assumed for the hard material. In this case, the exchange spring formation starts from the hard/soft interfaces, and the resulting coercivity for soft dominant superlattices is negative. This corresponds to the standard switching mode for an exchange spring magnet, where the anisotropy provides the pinning force. When the temperature is elevated, due to the difference in the temperature variation of the magnetization and anisotropy, the Zeeman energy provides the pinning force at large fields. The anisotropy stabilizes the whole structure at small fields. Applying a negative field, exchange springs form in the soft magnetic layers, and the coercivity is hence positive. This is the switching mode appropriate for soft dominant samples at high temperature. Obviously, due to the change in pinning mechanism, the bending field in this mode does not obey the $1/t_s^2$ law, which is derived based on the pinning provided by the anisotropy of the hard magnetic material.

Chapter 5

Exchange spring collapse

The deviations of the room temperature exchange spring from ideal behaviour, as discussed in Chapter 4, results from the reduction of the hard layer anisotropy, at high temperatures. But it is also possible to bring about non-ideal exchange spring behaviour by introducing one or two hard $DyFe_2$ mono-layers directly into the centre of the soft YFe_2 layers or doping YFe_2 layers uniformly with $DyFe_2$. In this chapter, we report both experimental and theoretical studies of such modified springs. In particular, the OOMMF simulation package [39], originally developed at NIST, has been used to give further insights into the whole demagnetization process. This relies on extensions designed especially for our cubic anisotropy system [38]. In the OOMMF simulations, we use the coordinate system appropriate to our MBE grown (110) films: the z direction is parallel to [110], which is the film normal. x and y directions correspond to $[00\bar{1}]$ and $[\bar{1}10]$, respectively. Depending on the temperature, the in-plane easy axis is $[00\bar{1}]$ or $[\bar{1}10]$. For both the VSM and OOMMF results, we will only use the crystallographic notation ($[00\bar{1}]$, $[\bar{1}10]$, [110] and etc.) to specify directions, in order to avoid confusion. The use of the film coordinate is only confined to the actual implementation of the OOMMF simulation. There is no explicit reference to it in the description of the experimental and theoretical results.

In general, any increase in soft-layer anisotropy, either uniform or by doping as described above, can give rise to irreversible exchange spring behaviour, which we denote as 'exchange spring collapse'. In fact, exchange spring collapse has already been observed in the FM coupled systems SmCo/Co system [85] and $CoPt/TiO_x/CoPt$ [98]. Similar behaviour can also be realized in the $DyFe_2/YFe_2$ system [99], where the anisotropy K_s has been artificially set to a higher value. A similarly simulated demagnetization curve can be seen in Fig. 5.1, which shows hysteretic behaviour at ~ 0.43 T. The irreversible jump at 0.43 T corresponds to the formation of a domain wall in the top soft layer. The domain wall penetrates into the adjacent hard layer,

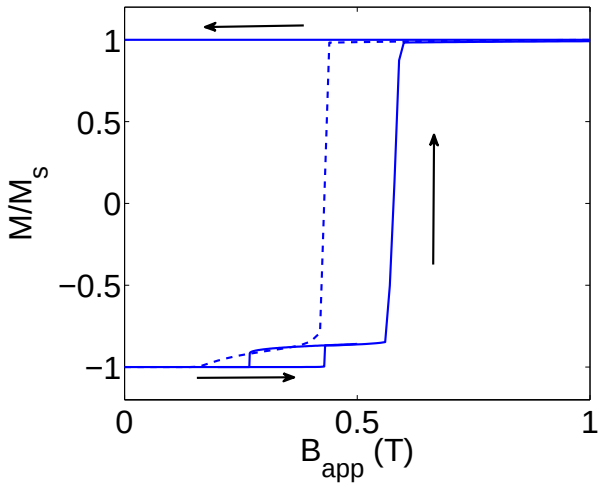

Figure 5.1: Simulated demagnetization curve showing irreversible behaviour for the exchange spring superlattice [$DyFe_2$ 45 Å/YFe_2 180 Å] × 18. The parameters used here are the same as those stated in Chapter 4 for MOKE simulation, except the soft layer anisotropy constant now has been increased to $K_s = K_h/10$. The dashed line is copied from Fig. 4.9.

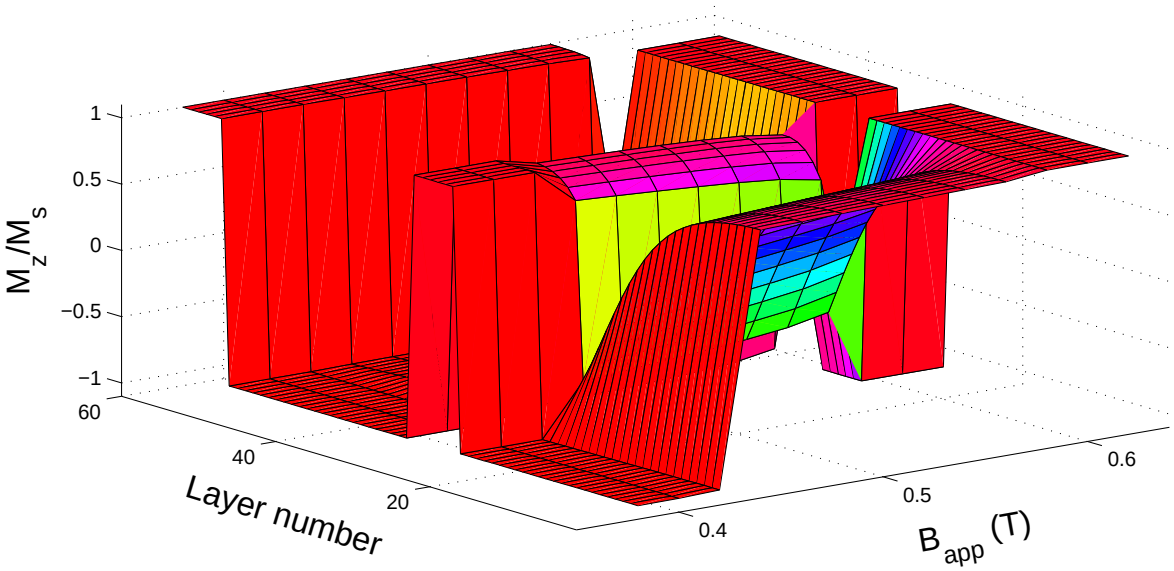

Figure 5.2: Normalized z component of magnetization of the top 60 atomic layers for the simulated hysteresis curve given in Fig. 5.1, showing the formation of a domain wall in the top soft layer, with increased anisotropy constant $K_s = K_h/10$. The amplitude of variation of the z component for the remaining layers is small.

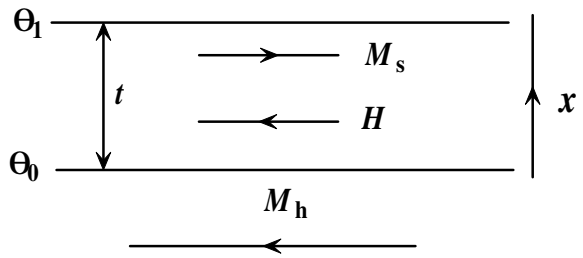

Figure 5.3: Sketch of the bilayer configuration used for the analytical discussion of the exchange spring collapse. Note here the positive direction for the x coordinate is reversed, as compared to the bilayer structure used in Chapter 3.

but the deviation in the next soft layer is negligible, as shown in Fig. 5.2. To obtain those results, uniaxial anisotropy is assumed, as what we have done in Chapter 4. In this case, the easy axis is denoted as the z axis, which is different from the notation used for cubic anisotropy in OOMMF simulation. The same convention, i.e. z-axis is the easy axis and x direction is the film normal, is adopted in the first section (Section 5.1) of this chapter, for an analytical discussion about irreversible exchange springs.

5.1 Analytical investigation

5.1.1 Infinite interface coupling

A simple picture of the induced irreversibility and the determination of the critical value of the soft layer thickness allowing for the occurrence of irreversibility can be provided by the analytical model which we have used for the discussion of the bending field in Chapter 4. Only the outline will be given here, as a detailed derivation has been given in Chapter 3.

First, the case of an infinitely hard hard layer with also an infinite interface exchange coupling constant will be considered. The relative configuration of the soft layer , the hard layer magnetization and the applied field is shown in Fig. 5.3. The Gibbs free energy is defined as

$$F = \int_0^t \left[A \left(\frac{d\theta}{dx} \right)^2 + \mu_0 M H \cos\ \theta + K \sin^2 \theta \right] dx. \tag{5.1}$$

For simplicity, the subscript s has been omitted. So K is the uniaxial anisotropy constant and A the soft layer exchange coupling constant. Variation of F to minimize it leads to the differential equation for θ

$$\frac{d^2\theta}{dx^2} + \left(\frac{\alpha}{2} - \beta \cos\ \theta \right) \sin\theta = 0 \tag{5.2}$$

with $\alpha = \mu_0 MH/A$, $\beta = K/A$. The first integral of Eq. (5.2) is given by

$$\frac{d\theta}{dx} = \sqrt{\alpha(\cos\ \theta - \cos\ \theta_1) + \beta(\sin^2\theta - \sin^2\theta_1)}. \tag{5.3}$$

This integral can be carried out explicitly, with boundary conditions

$$\left.\frac{d\theta}{dx}\right|_t = 0, \quad \theta|_0 = 0, \tag{5.4}$$

yielding

$$\sin\frac{\theta}{2} = \left(\frac{\alpha - \beta\cos\theta - \beta\cos\theta_1}{\alpha - 2\beta\cos\theta_1}\right)^{1/2} \sin\frac{\theta_1}{2}\ \mathrm{sn}\left(x\gamma, \rho\sin^2\frac{\theta_1}{2}\right), \tag{5.5}$$

where $\gamma = \sqrt{\alpha/2 - \beta\cos\theta_1}$ and $\rho = (\alpha + \beta - \beta\cos\theta_1)/(\alpha - 2\beta\cos\theta_1)$. sn is the Jacobi sine elliptic function [100] and t is the thickness of the soft layer, cf. Fig. 5.3. The value of θ_1 is determined by the eigenvalue equation obtained at $x = t$, $\mathrm{sn}(t\gamma, n) = 1$ with $n = \rho\sin^2\theta_1/2$. θ_1 is then defined as a function of H through this implicit equation, and once θ_1 is determined, the whole soft layer configuration is determined. Set $\theta_1 = 0$, then $n = 0$ and the eigenvalue equation reduces to $\sin t\gamma = 1$. The corresponding bending field can be determined as

$$\alpha = 2\beta + \frac{\pi^2}{2t^2} \rightarrow B_B = \frac{2K}{M} + \frac{\pi^2}{2}\frac{A}{Mt^2}. \tag{5.6}$$

As can be expected, B_B is the largest field for which a uniform solution can exist. This form for the bending field has been obtained before for exchange coupled bilayers with an infinitely soft layer [88] and is well known. Differentiating the eigenvalue equation with respect to H,

$$\frac{\partial\theta_1}{\partial H} = \frac{\frac{\partial\gamma}{\partial H}t - \frac{\partial J}{\partial n}\frac{\partial n}{\partial H}}{\frac{\partial J}{\partial H}\frac{\partial n}{\partial\theta_1} - \frac{\partial\gamma}{\partial\theta_1}t}. \tag{5.7}$$

J is the complete elliptic integral of the first kind. Require $\partial\theta_1/\partial H \rightarrow \infty$, we get an implicit equation for the nucleation field at which the irreversibility sets in,

$$\frac{\partial J}{\partial n} = \frac{L(n) - (1-n)J(n)}{2n(1-n)} = \frac{2t\beta\gamma^3}{\alpha\gamma^2 - \beta^2\sin^2\theta_1}. \tag{5.8}$$

L is the complete elliptic integral of the second kind. At B_B with $\theta_1 = 0$, this gives the critical ratio $r = t/\delta = (2\sqrt{3})^{-1}$ for the setting in of irreversibility, where $\delta = \pi\sqrt{A/K}$ is the Bloch domain wall width of the soft phase.

5.1.2 Finite interface coupling

For AFM finite interface exchange coupling $A_0 < 0$, the Gibbs free energy becomes

$$F = \int_0^d \left[A\left(\frac{d\theta}{dx}\right)^2 + \mu_0 MH\cos\ \theta + K\sin^2\theta\right] dx + 2\nu(1 - \cos\theta_0), \tag{5.9}$$

where $\nu = |A_0|/a > 0$, and a is the inter atomic distance for the two interface atomic layers. The finite interface coupling does not affect the differential equation (5.2) for the determination of the equilibrium configurations, and the change occurs in the boundary conditions:

$$\left.\frac{d\theta}{dx}\right|_t = 0, \quad \left.\frac{d\theta}{dx}\right|_0 = \frac{\nu}{A}\sin\theta_0. \tag{5.10}$$

Expand Eq. (5.3) to second order in θ and impose the boundary conditions, the equation for the bending field reads $A\gamma\tan\gamma t = \nu$ where $\gamma = \sqrt{\alpha/2-\beta}$. The angle θ_0 is related to θ_1 as $\theta_0 = \theta_1\cos\gamma t$. For the investigation of the susceptibility, the 4th order solution and interface boundary condition, with infinitesimal variations on field and angles $\alpha \to \alpha(1+\tau)$, $\theta_0 \to \theta_0 + \eta_0$ and $\theta_1 \to \theta_1 + \eta_1$, are needed:

$$\begin{aligned} \eta_0 - \eta_1\cos\gamma t &= \frac{\theta_1}{4}\gamma t\sin\gamma t\left(3p\,\theta_1^2 - \frac{\alpha\tau}{\gamma^2}\right) + \frac{p}{4}\theta_0\left(\theta_1^2 - \theta_0^2\right), \\ \eta_0(A^2\gamma^2+\nu^2)\theta_0 - \eta_1 A^2\gamma^2\theta_1 &= \frac{A^2}{4}\tau\alpha(\theta_1^2-\theta_0^2) + \frac{\nu^2}{6} + \frac{A^2}{2}p\gamma^2(\theta_0^4-\theta_1^4), \end{aligned} \tag{5.11}$$

where $p = (\alpha - 8\beta)/24\gamma^2$. To guarantee nontrivial solution for ηs, the augmented determinant has to be zero because the determinant of the coefficients matrix is zero. This gives the relation

$$\frac{\tau}{\theta_1^2} \propto -4 + 6p\left[2 + 3\sec^2\gamma t\left(1 + \frac{2\gamma t}{\sin 2\gamma t}\right)\right], \tag{5.12}$$

which is exactly proportional to the denominator of Eq. (8) (χ_c) in [91] with an infinite hard layer.

By integrating the z component of the magnetization, which is proportional to $\cos\theta$, the total easy axis magnetization is found to be $\propto \theta_1^2$. Consider that the variation in field is τ, the susceptibility is thus proportional to θ_1^2/τ. Irreversibility corresponds to a divergent susceptibility, hence we should have the right hand side in Eq. (5.12) $\to$ 0. This equation can only be satisfied by $\gamma^2 \geq 3\beta$. On substituting this condition into the expression for the bending field, we can get the critical ratio for the irreversible spring to occur

$$r = \frac{1}{\sqrt{3}\pi}\arctan\frac{\delta}{\sqrt{3}\pi}\frac{\nu}{A}. \tag{5.13}$$

For infinite ν, this reduces to $r = 1/2\sqrt{3} \simeq 0.29$. The value $r \sim 0.2$ [99] corresponds to $\nu = 2\sqrt{3}\pi A/\delta$. For the material of our soft phase, YFe_2, the simple analysis presented above is not applicable, because of its cubic anisotropy. Actually, domain walls in cubic materials have many variants [101], rather than simple Bloch and Neel walls in uniaxial materials. Nonetheless, we can still use the same expression for uniaxial materials to get an estimate of order for cubic materials. An effective uniaxial anisotropy constant

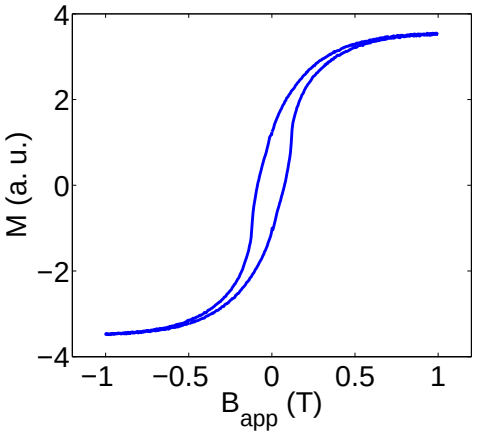

Figure 5.4: Hysteresis loop for [$DyFe_2$ 40 Å/YFe_2 160 Å] × 20 at 300 K with the field along the [00$\bar{1}$] direction.

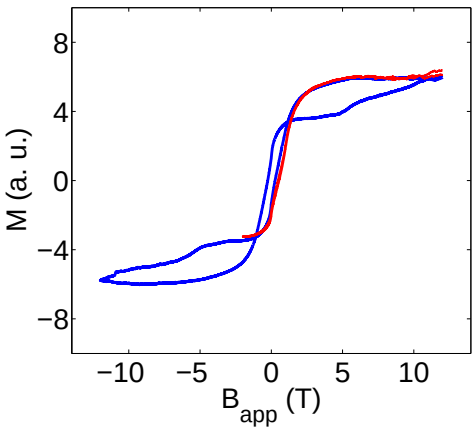

Figure 5.5: Major (blue) and minor (red) hysteresis loops for [$DyFe_2$ 40 Å/YFe_2 160 Å] × 20 at 80 K with the field along the [00$\bar{1}$] direction.

K_s for YFe_2 can be obtained from the coercivity simply through the relation $\mu_0 H_c = 2K_s/M_s$, with H_c the coercive field and M_s the magnetization. Neither the coercivity nor the magnetization is a rapid changing function of temperature for YFe_2, so the value of K at 10 K will be used to get an estimate. Putting the coercivity $\mu_0 H_c = 30$ mT and the magnetization $M = 5.6 \times 10^5$ A/m at 10 K into the expression for K_s, we can get the value $K_s = 8.4 \times 10^3$ J/m^3. The exchange coupling constant can be taken as $A = 1.46 \times 10^{-11}$ J/m, as used in the OOMMF simulations. Then the critical thickness corresponding to $r = 0.2$ will be 260 Å. Given the rough approximation used here, this value could be reduced by 2, down to $\sim$ 130 Å, if 90° domain walls in cubic materials are taken into account.

5.2 Reversible exchange springs

Prior to examining exchange spring collapse in the $DyFe_2/YFe_2$ system, induced by placing one or two mono-layers into the magnetically soft YFe_2 regions or doping, it is instructive to review and detail results from the undoped $DyFe_2/YFe_2$ system. To this end, the 1:4 YFe_2 dominated superlattice [$DyFe_2$ 40 Å/YFe_2 160 Å] × 20 has been studied first. For fields directed along the easy [00$\bar{1}$] axis at low temperatures, it is well known that the system exhibits negative coercivity [19]. For our purposes, we have applied the field along both the 'easy' [00$\bar{1}$] and [$\bar{1}$10] axes, at temperatures from 300 K down to 10 K. A typical curve at 300 K is shown in Fig. 5.4. The coercivity at this

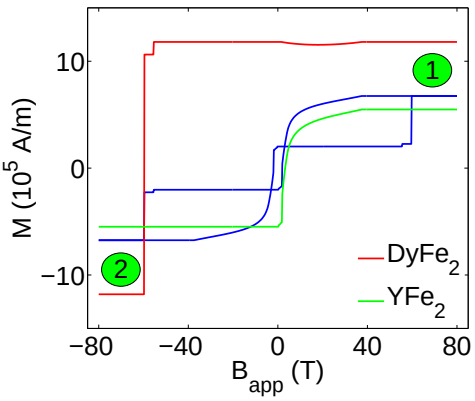

Figure 5.6: OOMMF simulated total (blue) and compound specific demagnetization curves for [$DyFe_2$ 40 Å/YFe_2 160 Å] × 20 at 100 K with the field along the [00$\bar{1}$] direction. The circled numbers correspond to those shown in Fig. 5.7.

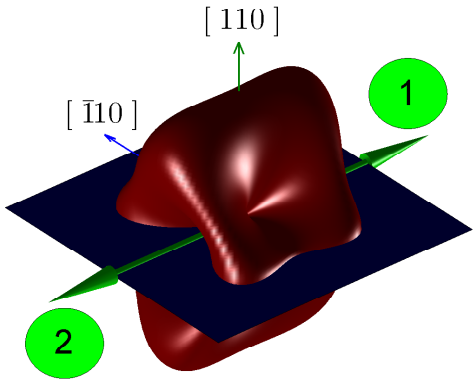

Figure 5.7: Energy surface for $DyFe_2$ at 100 K. The blue plane represents the (110) film plane. The green arrows with adjacent circled numbers show possible stable directions.

temperature is only 82.9 mT.

When the temperature is decreased below 100 K, [00$\bar{1}$] is the in-plane easy axis due to the strong crystal field at the Dy^{3+} sites. Measured major and minor hysteresis loops at 80 K can be seen in Fig. 5.5. Negative coercivity can be clearly observed, and the corresponding coercivity is −0.256 T. From the minor loop, we can see that the exchange spring unwinding is almost completely reversible, as can be expected. Any irreversibility is very small and barely detectable. Such irreversibility could originate from weak anisotropy in the soft phase, as will be shown later by the OOMMF simulation, or any deviation from the ideal single domain model on which our paradigm of exchange spring is based. From the temperature dependence of the irreversibility, thermal effects clearly contribute to it: the degree of hysteresis decreases if the temperature is lowered to 60 K.

The whole demagnetization process can be understood based on the OOMMF simulation. Starting from the positively saturated state, the unwinding of the exchange spring will start from the hard/soft interfaces, on decreasing of field. The middle part of the soft phase will continuously rotate away from the parallel configuration, tilting out of the film towards [010], until the whole soft phase becomes antiparallel to the direction of the hard phase, which happens at the negative coercive field. The stable configuration at zero field thus is this antiparallel state, with the hard and soft moments parallel to [00$\bar{1}$] and [001], respectively. The rotation process of soft moments

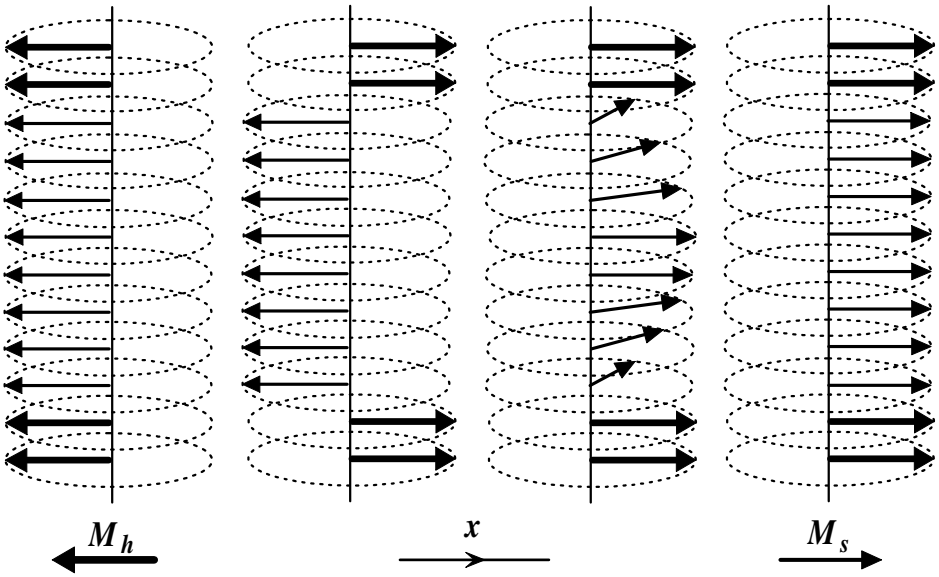

Figure 5.8: A schematic representation of the spin configuration for the demagnetization process for [$DyFe_2$ 40 Å/YFe_2 160 Å] × 20 at 100 K with field along the [$00\bar{1}$] (x) direction. Thick and thin arrows denote the magnetic moments of $DyFe_2$ and YFe_2, respectively. From right to left, the field decreases from 100 T to −100 T. The out-of-plane (z) component is not shown, so what is drawn here is the projection of the moments into the film plane.

can actually be viewed as a process of domain wall penetration. Further decrease of field will switch the hard phase to the direction of the applied field, at which point both the soft and the hard phases are parallel again. This simulated picture is qualitatively consistent with the experimental results. The simulated demagnetization curves are given in Fig. 5.6. The whole demagnetization process is easily understood on the basis of the anisotropy energy surface for $DyFe_2$ at 100 K (Fig. 5.7), including both the crystalline and magneto-elastic terms. The small step at −55.6 T is caused by the switching of the bottom hard, $DyFe_2$, layer and the gradual change of magnetization around 0 T is due to the rotation of the top soft layer of the hard/soft stack of moments, used to model our system. The simulated coercivity at 100 K is −1.8 T. A schematic spin configuration is given in Fig. 5.8.

Note that for this structure, simulation shows that the unwinding of the exchange spring is almost reversible, only at the (negative) coercive field does an irreversible switching event occur. At the coercive field, the moments in the middle of the soft phase is almost perpendicular to, in the (001) plane and parallel to [010], those of the hard layers, which still remain parallel to one another. But practically, this irreversibility is too small to be observed; it is easily smeared out by thermal effects. This irreversibility arises from the finite anisotropy constants for the soft phase used in our simulation.

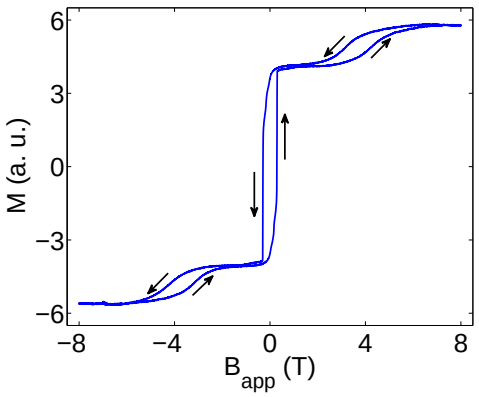

Figure 5.9: Hysteresis loop for [$DyFe_2$ 40 Å/YFe_2 160 Å] × 20 at 250 K with field along the [$\bar{1}$10] direction. Small arrows denote the field sweeping sequence.

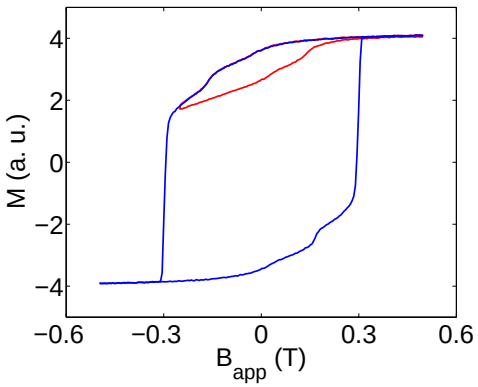

Figure 5.10: Major (blue) and minor (red) loops of [$DyFe_2$ 40 Å/YFe_2 160 Å] × 20 at 250 K with field along the [$\bar{1}$10] direction.

If we decrease those values, the irreversibility disappears. This argument has been verified by decreasing the soft anisotropy constants to 1/1000 of those of the hard phase, where the whole unwinding process is then completely reversible. According to the simulation, the out-of-plane component, z component, is not small during the unwinding, because the demagnetization field is not included in our 1D model. But even if it is included, in the current case, there is no observable difference due to the 1D character of our model.

At temperatures higher than 100 K, the easy axis for $DyFe_2$ films is close to [$\bar{1}$10]. Indeed, our reference sample does exhibit easy axis behaviour when we applied the field along the [$\bar{1}$10] direction, as can be seen in Fig. 5.9 for a hysteresis loop at 250 K. The corresponding coercivity at this temperature is 0.294 T, which is of the same order of the coercivity as of a pure $DyFe_2$ film. Note that the minor loops (Fig. 5.10) around zero field show that the exchange spring is irreversible, similar to the hysteresis loop shown in Fig. 5.1. Given the presence of such irreversibility even in a pure $DyFe_2$ film, its origin may be contributed to domain wall pinning. The feature at a higher field value, around 3.5 T, is similar to a spin-flop transition [102, 103].

When the temperature is lowered, the easy axis of $DyFe_2$ will rotate away from [$\bar{1}$10] to [00$\bar{1}$], due to the magneto-elastic anisotropy. So the [$\bar{1}$10] demagnetization behaviour of our superlattice sample is expected to show some hard axis character. But surprisingly, the [$\bar{1}$10] demagnetization curves still show easy axis behaviour, as demonstrated by a typical low temperature curve in Fig. 5.11, down to even 50 K. The reversibility of the exchange spring unwinding is supported by the minor-loop

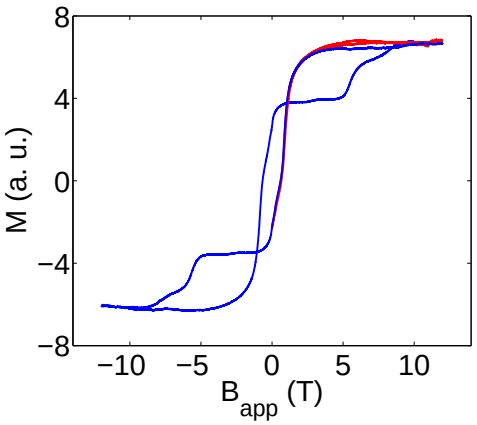

Figure 5.11: Major (blue) and minor (red) hysteresis loops for [$DyFe_2$ 40 Å/YFe_2 160 Å] × 20 at 100 K with field along the [$\bar{1}10$] direction.

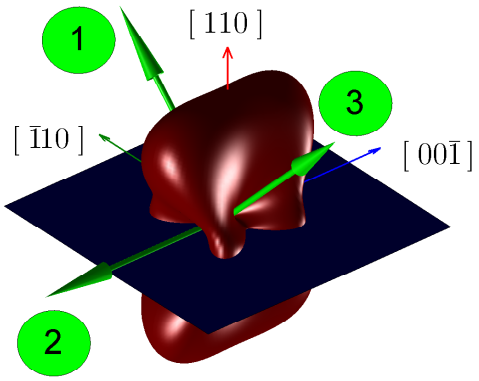

Figure 5.12: Energy surface for $DyFe_2$ at 200 K. Notations are the same as in Fig. 5.7.

measurements. The coercivity at 100 K is −0.603 T. The reason for this unexpected phenomenon can be seen from the energy surface of the cubic anisotropy (Fig. 5.12). Actually, [$\bar{1}10$] axis corresponds to a metastable state at low temperatures [2].

At 380 K, OOMMF simulation gives the following spin configurations at different stages of the demagnetization process. This temperature is higher than the actual experimental temperature (250 K) in an attempt to accommodate thermal effects to some extent. At the largest simulated field, 20 T, the system is still not saturated: the soft magnetization is parallel to the applied field, but that of the hard phase is perpendicular to the field, parallel to the [001] direction in the film plane. Tight domain walls form at the interfaces. Upon decreasing the field, the soft phase remains unchanged, while the hard phase rotates further away from the applied field direction, forming an obtuse angle with respect to the soft magnetization just above the first switching field, 10.3 T. This picture is consistent qualitatively with the neutron scattering analysis of the same system at 250 K [104]. At the same time, the tightly wound domain walls are relaxed. After the switching, the soft phase is mainly parallel to the field, with only small deviation at the interfaces, whereas the hard phase is antiparallel to the field, with a small component out of the film plane, towards [$0\bar{1}0$]. The moments at the interfaces are perfectly antiparallel to each other.

Actually, the two directions for $DyFe_2$ magnetization at 20 T, [001] and [$00\bar{1}$], are degenerate: the direction of the $DyFe_2$ magnetization can point to either direction. This degeneracy is lifted by the small components of the applied field along x axis. As stated before in Chapter 1, small x and z components are used to initiate the

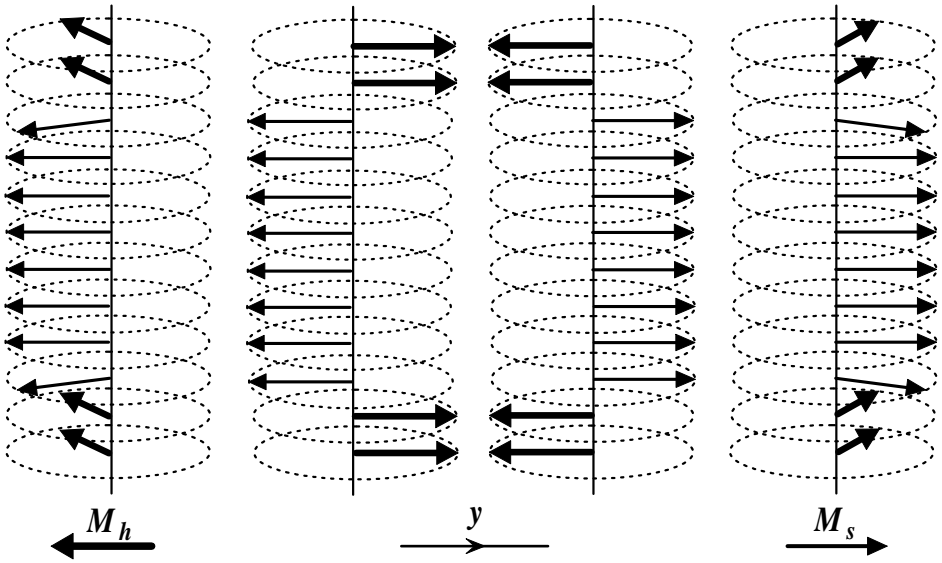

Figure 5.13: A schematic representation of the spin configuration for the demagnetization process of [$DyFe_2$ 40 Å/YFe_2 160 Å] × 20 at 380 K with field along the $[\bar{1}10]$ (y) direction. Thick and thin arrows denote the magnetic moments of $DyFe_2$ and YFe_2, respectively. The applied magnetic field decreases from 20 T to −20T from right to left. As in Fig. 5.8, only the projection of the moments into the film plane is drawn here.

dynamic evolution of magnetization. The orientation of the hard phase can be switched from [001] to $[00\bar{1}]$ by a negative x component of the applied field. The spin-flop [105, 106, 107] switching here can be viewed as the irreversible switching mediated by domain wall formation in the hard phase, where the dominant soft phase cannot support domain wall due to the stabilization affected by the applied field. Of course, given the large anisotropy of the hard phase, the domain walls will centre mostly at the interfaces and penetrate into the soft phase. The same mechanism in the soft phase is responsible for the irreversible exchange springs to be discussed below. The complete antiparallel configuration is only achieved when the field is decreased to 9.8 T, except the bottom hard/soft bilayer, where a 90° domain wall was formed in the soft layer due to the tilting along [010] of the bottom hard layer. At the interface of this soft layer to the bottom hard layer, the soft spin is perpendicular to the film plane, parallel to $[\bar{1}\bar{1}0]$. Decreasing the field to zero, the 90° domain wall penetrates progressively towards the centre of the stack of spins, causing the adjacent hard layer to tilt to [100]. During this process, the configuration of the bottom hard layer remains the same. The central part of the domain wall, now in the middle of the soft layer rather than at the interface, is still parallel to $[\bar{1}\bar{1}0]$.

Applying a negative field will move the moments out of plane, with the soft mag-

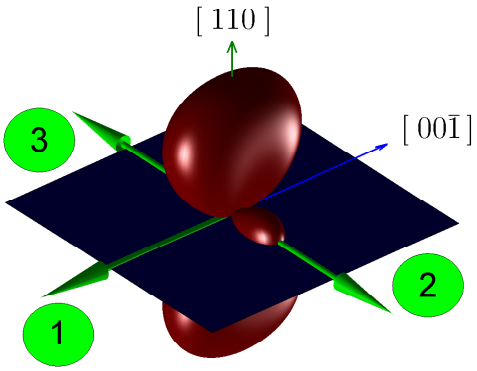

Figure 5.14: Energy surface for $DyFe_2$ at 380 K. Notations are the same as in Fig. 5.7.

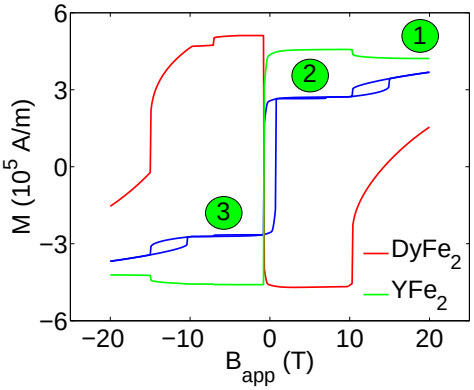

Figure 5.15: Simulated hysteresis loop for [$DyFe_2$ 40 Å/YFe_2 160 Å] × 20 at 380 K with the field along [$\bar{1}$10] direction. The total hysteresis loop is given by the blue curve. The circled numbers correspond to those in Fig. 5.14.

netization tilting towards [010] direction, but they still remain perfectly antiparallel. The boundary of the region with a 90° domain wall in the soft layer of the hard/soft bilayers from the bottom hard layer penetrates further into several bilayer structures, with only the bottom hard layer is parallel to [010] while all the other hard layers are parallel to [100]. A 90° domain wall is also formed in the top soft layer. The abrupt switching at −0.7 T corresponds to the simultaneous 180° rotation of the two phases, so after that switching, the configuration is still antiparallel. The only change is that now it is the soft phase that is parallel with the applied negative field, along [1$\bar{1}$0]. At the same time, all domain walls are relaxed and a perfect antiparallel configuration is obtained.

A larger negative field will pull the magnetization of the hard layer out of the film plane, towards [010] direction. If the out of plane angle is too large, further decreasing the field induces the switching observed at 15 T, after which the perpendicular configuration is restored, with magnetization in plane and the hard magnetization parallel to [001] again. In the above simulations, sometimes the z component of each phase can be very large, but the average out-of-plane component is always very small, due to the AFM coupling. A sketch of the spin configuration at different stages of the whole demagnetization process is illustrated in Fig. 5.13. To put it into a simple picture, the $DyFe_2$ moments follow the following path, [001] → [1$\bar{1}$0] → [$\bar{1}$10] → [001], as shown in Fig. 5.14. Except for the switching transitions at the high field, all the moments are in

the (001) plane. The small step at -7 T is due to the premature switching to [001] of the bottom hard layer after rotating from $[\bar{1}10]$ to [010], forming an almost 90° domain wall in the adjacent soft layer. The simulated results are shown in Fig. 5.15.

At 200K, the temperature used to simulate the low temperature demagnetization processes, the picture is slightly different. Starting from 40 T, the system is already frustrated. Due to the large cubic anisotropy for $DyFe_2$, the magnetization of $DyFe_2$ is tilted out of plane, towards [010] direction, while that of YFe_2 is parallel to the field, in the plane. This leads to a frustrated configuration at the interfaces, with the spins almost perpendicular to each other. The out-of-plane angle of the hard layer keeps growing with the decreased field, followed by the relaxation of the frustrated, single atomic layer 90° domain walls into the whole soft layer, although the middle of the soft layers are still parallel to the field, until the plateau of the $DyFe_2$ response in Fig. 5.16 is reached. Proceeding from that point, the hard layer out-of-plane angle decreases a little, but the soft layer out-of-plane angle increases towards 90°, so the net effect is still a decrease of magnetization along y axis. At 1.5 T, the spins in the middle of the soft layer are parallel to $[\bar{1}\bar{1}0]$, then they rotate towards $[0\bar{1}0]$. The remanent state at zero field is a perfect antiparallel state, with the hard layer moments forming a finite out-of-plane angle, pointing towards [010].

On decreasing the field further, the soft layer magnetization aligns itself to the field direction, but the hard layer magnetization only moves towards the film normal ([110]) slowly. All those processes occur in the (001) plane. This increase of the hard layer out-of-plane angle stops at -14.8 T, where the hard layer moments are almost perpendicular to the film plane and a magnetic switching event occurs. After the switching, an almost perpendicular configuration appears: the YFe_2 moments are parallel to $[1\bar{1}0]$ and the $DyFe_2$ moments are close to [001], with the moments at the interfaces forming an obtuse angle. The slow convergence of the curve following that switching is due to the gradual rotating of the $DyFe_2$ moments in the film plane towards $[1\bar{1}0]$. The rotation is completed at -21 T, followed by a switching of the hard layers to [100]. Now all the moments are in (001) plane again, with the $DyFe_2$ moments pointing towards [100] and the YFe_2 moments parallel to $[1\bar{1}0]$. This configuration results in the frustrated domain walls, as in the case of a very large positive field. The whole switching process for $DyFe_2$ can be summarized as $[010] \rightarrow [001] \rightarrow [100]$. The simulated coercivity at this temperature is -1.1 T. Those switching modes can be understood from the energy surface of $DyFe_2$ at 200 K, as shown in Fig. 5.12.

The OOMMF simulation demonstrates that, at low temperature, the cubic anisotropy is the dominant term for the determination of the switching mode. Under this condition, the hard $DyFe_2$ phase is stabilized by the strong crystal field, and exchange

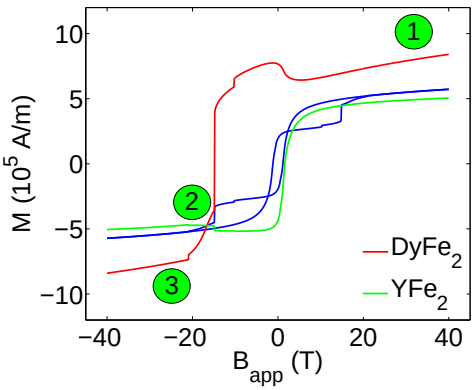

Figure 5.16: Simulated hysteresis loop for [$DyFe_2$ 40 Å/YFe_2 160 Å] × 20 at 200 K with field along the [$\bar{1}$10] direction. The circled numbers correspond to those in Fig. 5.12.

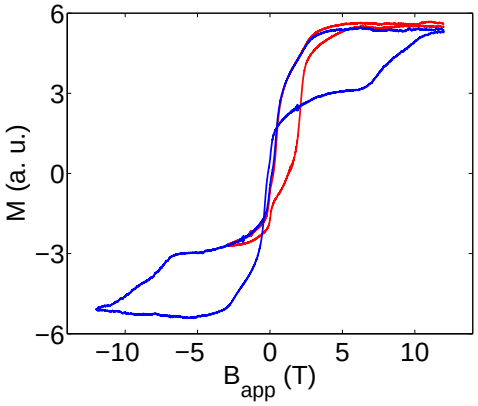

Figure 5.17: Hysteresis loop (blue) and minor loops (red) for [$DyFe_2$ 40 Å/YFe_2 80 Å/$DyFe_2$ 8 Å/YFe_2 80 Å] × 20 at 60 K with field along the [00$\bar{1}$] direction.

springs will always nucleate first in the soft YFe_2 phase. For field along both [00$\bar{1}$] and [$\bar{1}$10] directions, nucleation of exchange springs in the soft phase gives rise to negative coercivity, for soft dominant samples considered here. When temperature is increased, the cubic anisotropy decreases rapidly, resulting in a more and more important contribution from the magneto-elastic interaction. The magnetization of $DyFe_2$ is also a rapid varying function of temperature. The reduced magnetization of $DyFe_2$ at room temperature will make the Zeeman energy less effective to align the magnetization vector to the applied field. Combining those two effects, a spin-flop transition appears for field along the [$\bar{1}$10] direction at temperatures higher than $\sim$ 100 K. In this configuration, the $DyFe_2$ moments are perpendicular to the applied field and parallel to [001], which corresponds to a local minimum of the anisotropy energy functional. After the spin-flop transition, the hard and soft phases are antiparallel to each other. The antiparallel configuration is determined by the exchange interaction, which is not sensitive to temperature, as far as the temperature is not very close to the Curie temperature. A negative field flips the magnetization direction of both the hard and soft phases, so they are still antiparallel after the simultaneous flipping. This is caused by the minimization of the Zeeman energy. Minimization of the Zeeman and the exchange energies finally moves the $DyFe_2$ moments perpendicular to the applied field at a higher, negative, field value.

5.3 Exchange spring collapse

5.3.1 $DyFe_2$ thin layers embedded in soft YFe_2 layers

For the purpose of investigating irreversible exchange springs, an 8 Å layer of $DyFe_2$ is inserted into the soft layer. The structure of the sample to be studied in this section is [$DyFe_2$ 40 Å/YFe_2 80 Å/$DyFe_2$ 8 Å/YFe_2 80 Å] × 20. This is similar to the reference 1:4 sample except for the thin inter-layer. Due to the inter-layer diffusion, $DyFe_2$ atoms can penetrate beyond the nominal thickness, 8 Å [108]. When the field is applied along the $[00\bar{1}]$ direction at a temperature higher than 100 K, a typical hard axis response results. Easy axis behaviour appears only at low temperature. A hysteresis loop measured at 60 K can be seen in Fig. 5.17. The corresponding coercivity is −0.134 T, i.e. the coercivity is still negative, as can be expected for soft dominant samples. But the spring unwinding part of the loop is more complex, when compared to the reference sample (Fig. 5.5). As mentioned at the start of this chapter, with anisotropy introduced into the soft phase, irreversibility should be expected in this sample. Indeed, we have performed the desired partial demagnetization measurements, and irreversibility was observed, as can be seen clearly in Fig. 5.17. This irreversibility is not observed in the reference sample, so it must be attributed to the thin inserted $DyFe_2$ mono-layers. Fig. 5.18 shows the hysteresis loop and minor loops for the same sample measured at 80 K. Similar irreversibility is observed. The non-coincidence of the major and minor loops is caused by the different values for the high field susceptibility used to subtract the background diamagnetic contribution. The measured coercivity at 80 K is −0.469 T.

For detailed knowledge of the whole demagnetization process, OOMMF simulation has to be invoked. The simulated structure is [$DyFe_2$ 40 Å/YFe_2 80 Å/$DyFe_2$ 10 Å/YFe_2 80 Å] × 20. The size of the hard inclusion has been increased to 10 Å, simply because the unit cell size in the simulation is 10 Å. The temperature used here is 150 K. Starting from the largest simulated field value 100 T, the resulted configuration is a parallel state of the hard and the soft phases. At 75 T, deviation from the parallel state can be observed, where the hard inclusion in the soft phase first relaxes, whose direction becomes tilted slightly towards $[1\bar{1}\bar{1}]$, in the (110) plane. Due to the exchange coupling, the soft spins adjacent to the hard spin are also pulled towards $[\bar{1}1\bar{1}]$, forming an acute angle with respect to the hard spin. Then the hard spin switches to an out-of-plane configuration, close to $[9\bar{2}\bar{5}]$, at 72.4 T. Following the switching, the single hard spin rotates to [100]. At approximately 45.4 T, the out-of-plane angle reaches its maximum, now in (001) plane and close to [100] direction. From that point, the moments on both sides of the hard/soft interfaces start to relax in the (110) plane, with the hard spin

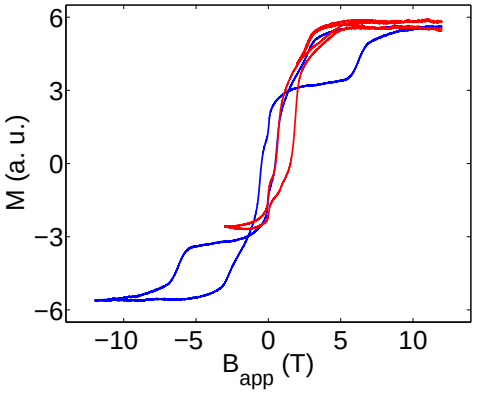

Figure 5.18: Hysteresis loop (blue) and minor loops (red) for [$DyFe_2$ 40 Å/YFe_2 80 Å/$DyFe_2$ 8 Å/YFe_2 80 Å] × 20 at 80 K with field along [$00\bar{1}$].

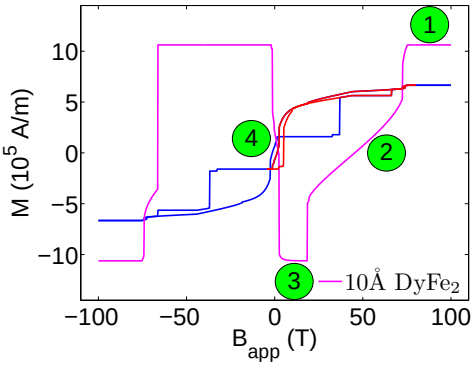

Figure 5.19: Simulated hysteresis loop (blue) and minor loop (red) for [$DyFe_2$ 40 Å/YFe_2 80 Å/$DyFe_2$ 10 Å/YFe_2 80 Å] × 20 at 150 K with field along the [$00\bar{1}$] direction.

rotating towards [$1\bar{1}\bar{1}$] and the soft spins to [$\bar{1}1\bar{1}$]. The resulted domain walls penetrate mostly into the soft phase, as in the case for the reference sample; while at the same time the out-of-plane angle of the hard inclusion spin decreases slowly. During the relaxation process, the hard inclusion switches to [001] at 18.4 T, where the soft domain walls propagate to the hard inclusion's position. This switching is caused by the pulling from the soft domain walls. And after the switching, the hard inclusion is antiparallel to its adjacent soft spins, dictated by the AFM coupling. At certain points of the following relaxation process, around 12.8 T, there are two 90° domain walls in a unit cell of the superlattice, which are located in the soft phase, separated by the hard inclusion, whose direction remains parallel to [001]. The direction of the hard inclusion's neighboring spins is still parallel to [$00\bar{1}$]. Due to the relaxation of the hard inclusion to [001], the springs in the soft phase are not as tight as before and the penetration depth of domain walls into the hard phase is reduced, resulting in a decrease of the non-uniformity in the hard phase. Finally, when the hard inclusion is tilted away from [001] and the obtuse angles of the soft spins at the interfaces are large enough, with respect to the [$00\bar{1}$] direction, the whole system collapses into another energetically more favorable state. In that state, the hard phase is perfectly parallel to [$00\bar{1}$] direction, while the hard inclusion spin is in the (001) plane, close to [$0\bar{1}0$]. The soft phase accommodates this configuration by rotating from [001] to [010] continuously. Then the hard spin is pulled away from the [$0\bar{1}0$] direction, into the film plane towards [$1\bar{1}0$], if the field is decreased further. The simulated coercivity is −1.2 T.

At −1.4 T, the stable state switches to the antiparallel configuration with all hard

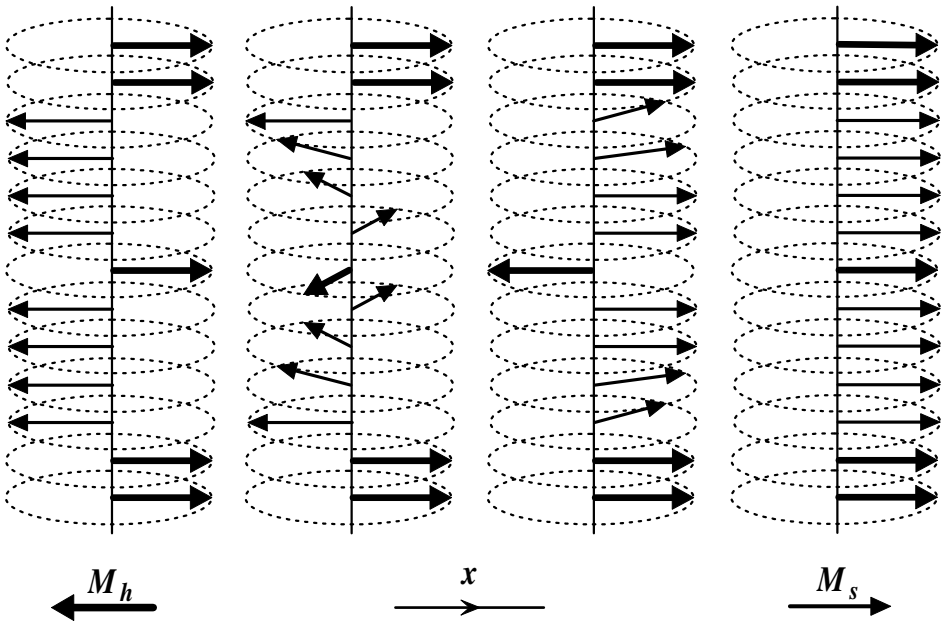

Figure 5.20: A schematic representation of the spin configuration for the demagnetization process of [$DyFe_2$ 40 Å/YFe_2 80 Å/$DyFe_2$ 8 Å/YFe_2 80 Å] × 20 at 150 K with field along the [00$\bar{1}$] direction. Thick and thin arrows denote the magnetic moments of $DyFe_2$ and YFe_2, respectively. H is the applied magnetic field. Only the projection of the moments into the film plane is drawn. The configurations shown here correspond to field down to −3 T, and the remaining configurations are similar to those shown in Fig. 5.8.

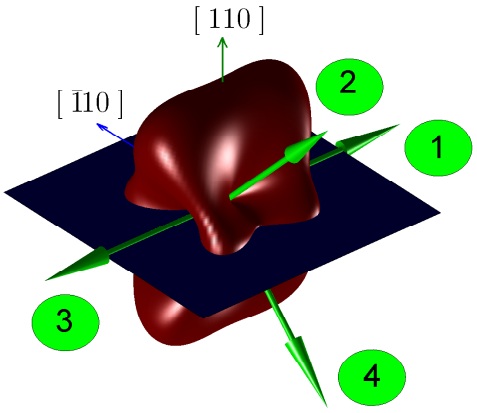

Figure 5.21: Energy surface for $DyFe_2$ at 150 K. Notations are the same as in Fig. 5.7.

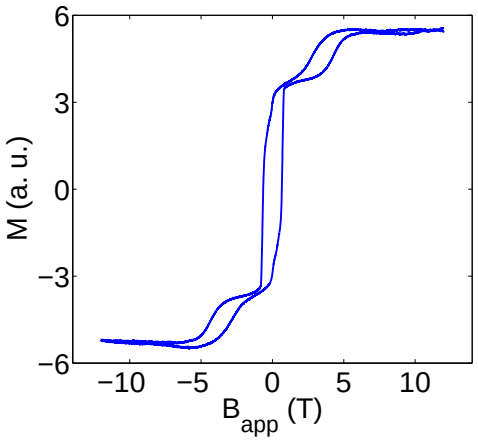

Figure 5.22: Hysteresis loop for [$DyFe_2$ 40 Å/YFe_2 80 Å/$DyFe_2$ 8 Å/YFe_2 80 Å] × 20 at 200 K for field along the [$\bar{1}$10] direction.

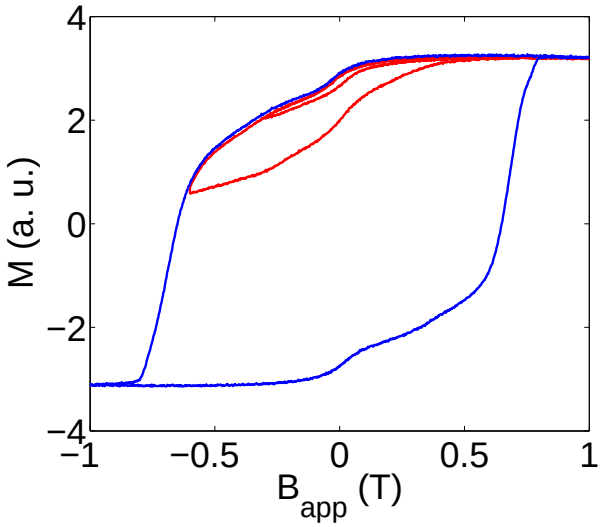

Figure 5.23: Major (blue) and minor (red) hysteresis loops for [$DyFe_2$ 40 Å/YFe_2 80 Å/$DyFe_2$ 8 Å/YFe_2 80 Å] × 20 at 200 K with field along the [$\bar{1}10$] direction.

moments pointing to [$00\bar{1}$] and all soft moments to [001]. This configuration remains stable until −37 T. At −37 T, the hard phase switches to the [001] direction, but the hard inclusion in the soft phase is still antiparallel to the soft magnetization, which is parallel to [001]. The hard inclusion switches at −66.4 T to [$1\bar{9}3$] again, without destroying the parallel configuration of both the soft and hard phases. From that point, the magnetization of the hard inclusion will rotate progressively towards [001], and switches to [001] at −74.2 T. Roughly, the switching mode for the hard phase is the same as that for the standard soft dominant sample, [$00\bar{1}$] → [001], whereas the switching mode of the hard inclusion, which determines the exchange spring irreversibility, is [$00\bar{1}$] → [100] → [001] → [$0\bar{1}0$] → [$00\bar{1}$] → [001]. The simulated demagnetization curves can be seen in Fig. 5.19. The role of the hard insertion in the soft layer can be seen in Fig. 5.20. The compound specific curves for $DyFe_2$ and YFe_2 are not shown, because they are almost identical to those of the reference sample. The whole demagnetization behaviour can be understood from the energy surface at 150 K (Fig. 5.21).

For the [$\bar{1}10$] direction, at high temperature, the qualitative behaviour does not change, i.e., the spin-flop like transition is still there, as shown in Fig. 5.22. The corresponding small field major and minor loops are given in Fig. 5.23. It can be seen that the irreversibility is still present. Actually, the whole demagnetization process is almost exactly the same. The OOMMF simulations at 380 K can be seen in Fig. 5.24. The only change is that the hard inclusion always remains antiparallel to the local soft magnetization, which is uniform in the vicinity of the hard inclusion. The coercivity increases to 1.1 T, due to the hard inclusion, which stabilizes the soft phase. In this case the applied field is opposing to the soft phase, not the hard phase as in

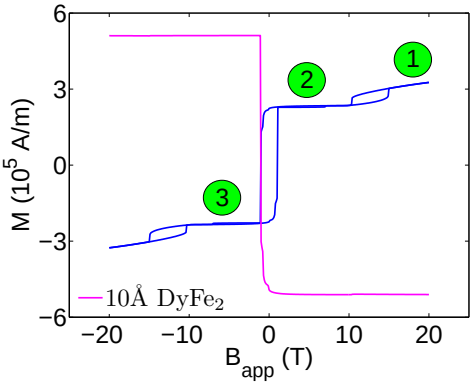

Figure 5.24: Simulated hysteresis loop for [$DyFe_2$ 40 Å/YFe_2 80 Å/$DyFe_2$ 10 Å/YFe_2 80 Å] × 20 at 380 K with field along the [$\bar{1}$10] direction. The circled numbers correspond to those shown in Fig. 5.14.

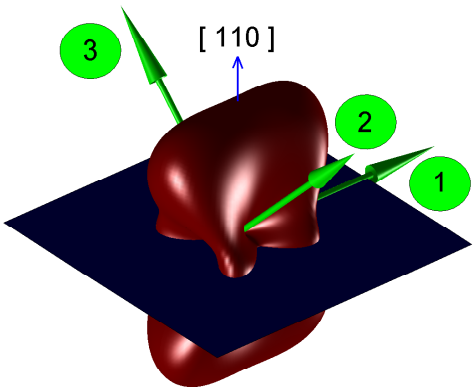

Figure 5.25: Energy surface for $DyFe_2$ at 200 K, showing the switching of the hard inclusion. Notations are the same as in Fig. 5.7.

the case of field applied along the [00$\bar{1}$] axis. Qualitatively, the only difference induced by the hard inclusion in the soft phase is the switching at −0.8 T, as compared to the continuous rotation found in the reference sample. But this switching only corresponds to the switching of the top hard/soft bilayer to [1$\bar{1}$0], including the hard inclusion in it. Both before and after switching, the hard inclusion is always parallel to the local soft magnetization. The natural consequence of the switching of the top soft layer before the switching of the whole structure is the introduction of two domain walls, one in the top and the other in the bottom, though the bottom domain wall is already there as in the reference sample. The switching of the top layer induced by the increased soft layer anisotropy is reminiscent of the uniaxial result shown in Fig. 5.1. The two domain walls relax when the whole structure switches. The predicted difference in degree of irreversibility is qualitatively in agreement with experiment, if Fig. 5.9 and Fig. 5.22 are compared.

At 200 K, simulation gives a different picture from that of the reference sample geometry. At 40 T, the soft phase is mostly parallel to the applied field direction, [$\bar{1}$10], and the hard phase is tilted towards [010], in the [001] plane. But the hard inclusion is not antiparallel to the soft magnetization anymore. This is due to the large cubic anisotropy, which dominates over the magneto-elastic term. Actually, the direction of the hard inclusion is almost parallel to [00$\bar{1}$], tilted slightly towards [1$\bar{1}\bar{1}$] in the film plane. On decreasing the field, the whole structure starts to relax: after

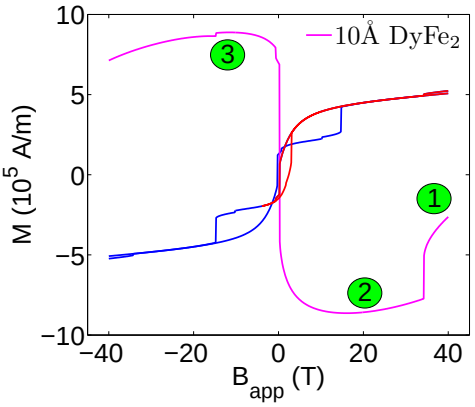

Figure 5.26: Simulated hysteresis (blue) and minor (red) loops for [$DyFe_2$ 40 Å/YFe_2 80 Å/$DyFe_2$ 10 Å/YFe_2 80 Å] × 20 at 200 K with field along the [$\bar{1}$10] direction. The circled numbers correspond to those shown in Fig. 5.25.

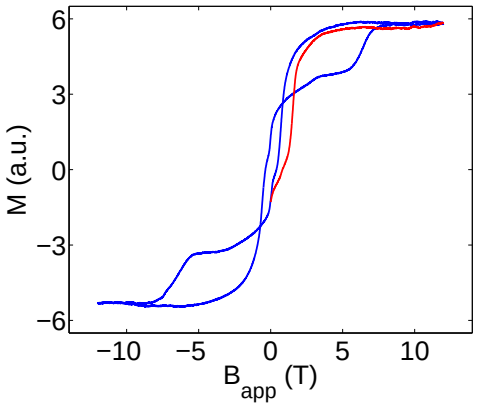

Figure 5.27: Hysteresis (blue) and minor (red) loops for [$DyFe_2$ 40 Å/YFe_2 80 Å/$DyFe_2$ 8 Å/YFe_2 80 Å] × 20 at 100 K with field along the [$\bar{1}$10] direction.

rotating towards [$1\bar{1}\bar{2}$] in plane with the decreasing field, the hard inclusion switches to [100] at 34.2 T, and the domain walls at hard/soft interfaces relax, as done in the reference sample. What is different here is that this relaxation process takes two steps: first, the relaxation is mainly in the hard phase, tilting it to [010] and the hard inclusion to [$1\bar{1}0$]. At 16.2 T, the out-of-plane angle of the hard inclusion reaches its minimum. Then relaxation takes place in both the hard and soft phases. During the relaxation process, the soft phase rotates away from [$\bar{1}$10] to [$\bar{1}\bar{1}$0] to relax the interface domain walls, while the hard phase behaves exactly the same as in the reference sample, gradually tilting out of plane in the (001) plane. At the same time, the hard inclusion rotates to [100] again, with an increasing out-of-plane angle. The soft phase keeps rotating towards [$\bar{1}\bar{1}$0] until the field reaches 0.2 T, where the middle of the soft phase is parallel to [$\bar{1}\bar{1}$0] and a switching event occurs.

After this switching, the perfect antiparallel configuration is achieved, with the soft phase parallel to [$0\bar{1}0$] and the hard phase and the hard inclusion parallel to [010]. Further decreasing the field tilts the hard magnetization towards [110], and a switching of the hard phase happens at −14.8 T, where the hard magnetization rotates to the [100] axis, simultaneously introducing tight domain walls at the interfaces. All of the above mentioned transitions occur in the (001) plane, except for the first one for the hard inclusion, which is like a spin-flop transition from [$00\bar{1}$] to [100]. The switching path for the hard phase is very simple, [010] → [100], while that of the hard inclusion

is $[00\bar{1}] \rightarrow [100] \rightarrow [010]$ (Fig. 5.25). The missing stage for the hard phase at [001] is caused by the induced anisotropy in the soft phase, hence a increased domain wall energy $\propto \sqrt{AK}$. Fig. 5.26 shows the simulated hysteresis curve, which can be compared to the experimental hysteresis loops at 100 K, Fig. 5.27. According to the simulation, the absolute value of the negative coercivity is decreased as compared to the reference sample, which is a result of the increased effective anisotropy of the soft phase. The increased anisotropy can stabilize the spring and hence postpone the completion of spring winding, thus decreasing the absolute value of the negative coercivity. The experimental coercivity at 100 K is -0.384 T, whose magnitude is less than that for the reference sample. Hence the same trend is actually reproduced by the simulation.

As can be seen from the simulation, the main effect of the hard inclusion here is to increase the effective anisotropy of the soft phase, even though it is only 8Å thick. With this enhanced anisotropy, irreversibility is then clearly observable.

Minor loops can also be simulated. At low temperatures, the unwinding starts from the soft phase. But due to the hard inclusion, an effective pinning centre, with cubic anisotropy, is introduced. So the resultant relaxation path of the exchange spring is different from that of the standard sample. At 150 K, field along $[00\bar{1}]$, the jump at 2.4 T corresponds to the switching of the hard inclusion from [001] to $[0\bar{1}0]$, thus perpendicular to the hard phase, which is still parallel to $[00\bar{1}]$. From that point, the whole soft phase, including the antiparallel hard inclusion, relaxes towards [001] with the decreasing field. At -1.4 T, the complete antiparallel configuration is achieved. Increasing the field from the antiparallel state, the configuration remains unchanged until 5.2 T, where the configuration with the hard inclusion parallel to $[0\bar{1}0]$ reappears. From this picture, it can be concluded that the irreversibility is derived from the anisotropy of the hard inclusion, i.e. the energy barrier between the easy axes [001] and $[0\bar{1}0]$. The small hysteresis around 50 T is caused purely by the hard inclusion switching from [001] to [100].

The irreversibility at 200 K for field parallel to $[\bar{1}10]$ can be analyzed using the same method. Starting from the partially unwound phase, where the hard phase is parallel to [010] and the hard inclusion parallel to [100], all moments are in the (001) plane. This phase will evolve until the magnetization in the middle of the soft phase is almost perpendicular to the film plane. Subsequently the antiparallel configuration sets in at 0.2 T, with the hard moments parallel and the soft moments antiparallel to [010]. Increasing the applied field from this geometry, the magnetization of the soft phase will move towards $[\bar{1}\bar{1}0]$, leaving the hard magnetization still parallel to [010]. The switching at 3.1 T leads to the configuration where the hard magnetization is parallel to [010], but the hard inclusion is parallel to [100]. Before this switching, the

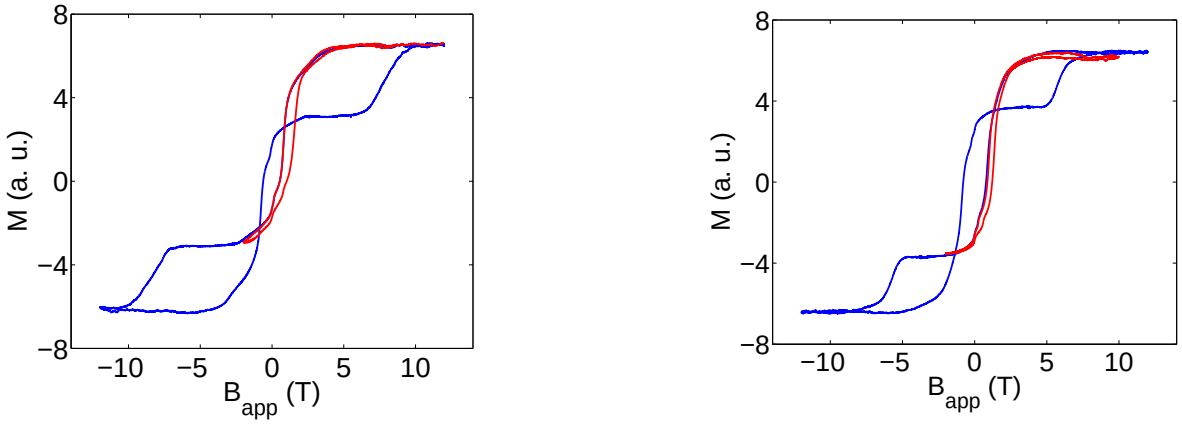

Figure 5.28: Major (blue) and minor (red) loops for [$DyFe_2$ 40 Å/YFe_2 80 Å/$DyFe_2$ 4 Å/YFe_2 80 Å] × 20 at 60 K (left, field along [00$\bar{1}$]) and 100 K (right, field along [$\bar{1}$10]).

whole system is characterized by the almost perpendicular to the film plane (parallel to [$\bar{1}\bar{1}$0]) magnetization direction in the middle of the soft layers. The whole process for this field direction occurs in the (001) plane. Following the above analysis, it is obvious that the irreversibility for [$\bar{1}$10] field results from the energy barrier between the [010] and [100] axes.

To proceed further, another sample with a thinner (4 Å, instead of 8 Å) $DyFe_2$ layer embedded in the middle of soft layers was investigated. Due to the reduced thickness of the hard inclusion, it should be expected that the induced effective anisotropy in soft layers should also be decreased. In turn, this results in a reduced degree of irreversibility. Actually, this is consistent with the experiment, with the applied field along both [00$\bar{1}$] and [$\bar{1}$10] (Fig. 5.28). The qualitative behaviour is similar to the exchange spring collapse sample with 8 Å $DyFe_2$ hard inclusion. A decreased degree of irreversibility is the only detectable difference between those two samples, as can be expected. Those results indicate that the induced irreversibility is quite robust against the variation in the hard inclusion thickness. A reduction in the hard inclusion thickness by a factor of two only decreases the widths of corresponding minor loops by almost the same factor, which can be seen from a comparison between Fig. 5.17 and Fig. 5.28. However, it should be reminded that 4 Å is only the nominal thickness, the actual thickness can be larger than 4 Å.

5.3.2 Doping soft YFe_2 layers with $DyFe_2$

In the original theoretical prediction for irreversible exchange springs, increased anisotropy for the soft layers was used to introduce the irreversible behaviour. To testify this idea, an alloy sample [$DyFe_2$ 40 Å/$Y_{1-x}Dy_xFe_2$ 160 Å] × 20 ($x = 0.025$) was studied. By

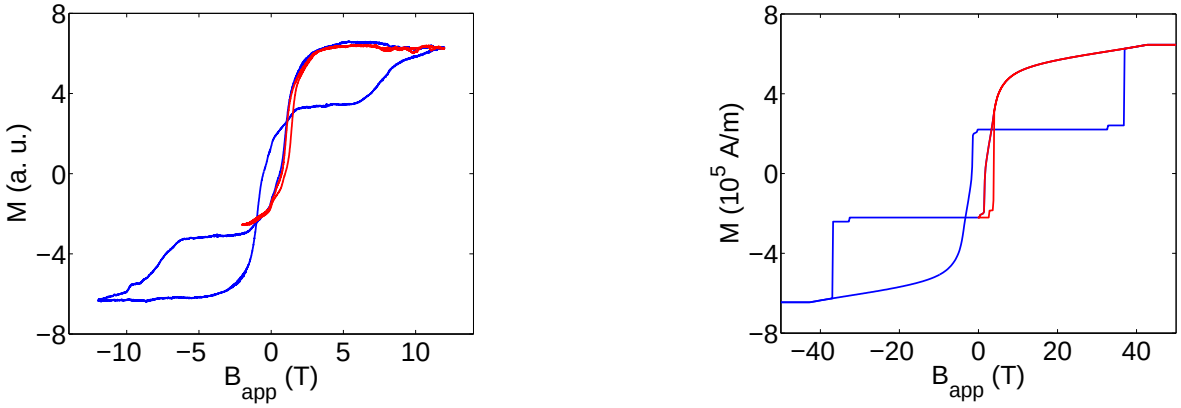

Figure 5.29: Measured (left, 60 K) and simulated (right, 150 K) major (blue) and minor (red) loops for [$DyFe_2$ 40 Å/$Y_{1-x}Dy_xFe_2$ 160 Å] × 20 ($x = 0.025$) with field along [$00\bar{1}$].

doping with hard $DyFe_2$, the anisotropy of the soft YFe_2 increases, similar to what was observed in $Dy_{1-x}Tb_xFe_2$ [2]. The concentration of $DyFe_2$ is chosen to match that of [$DyFe_2$ 40 Å/YFe_2 80 Å/$DyFe_2$ 4 Å/YFe_2 80 Å] × 20. VSM measurements (Fig. 5.29) show that the exchange spring unwinding is irreversible. But the width of the minor loops is significantly reduced as compared to the sample with 4 Å $DyFe_2$ inclusion. Similar reduction in the width of the minor loop can be observed in the OOMMF simulated results (Fig. 5.29). To take into account of the increased anisotropy in doped YFe_2, the crystalline anisotropy constants in the simulation were taken as the concentration average of the anisotropy constants of bulk $DyFe_2$ and YFe_2. This increases the anisotropy constants for the doped YFe_2 by a factor of 3.5, as compared to the undoped values. The simulated hysteresis corresponds to the energy barrier between the two axes, [001] and [$\bar{1}$00]. The qualitative agreement between experiment and simulation concerning minor loops, i.e. the reduction in width, indicates that local pinning through insertion of a thin $DyFe_2$ layer is more effective than uniform doping, for introduction of irreversible exchange springs. This difference between local pinning and uniform doping can be understood on the fact that, in the case of local pinning, formation of exchange springs requires more exchange energy. The step at 1.4 T in the simulated minor loop corresponds to the transition of the soft phase from [010] to [001], while the corresponding step at 4 T signifies the transition from [001] to [$\bar{1}$00].

5.4 Summary

Irreversibility of exchange spring unwinding has been studied experimentally using a VSM. OOMMF simulation has also been employed to understand the detailed switch-

ing modes. A soft-dominant sample, [$DyFe_2$ 40 Å/YFe_2 160 Å] × 20, is used as a reference sample. Low temperature exchange spring unwinding is reversible for field along the $[00\bar{1}]$ direction with negative coercivity. However, spin-flop transition of the hard phase is observed at room temperature for field applied along the $[\bar{1}10]$ direction, even though the low temperature hysteresis loops show behaviour similar to that of the $[00\bar{1}]$ axis. Irreversibility is observed in room temperature $[\bar{1}10]$ measurements, during the simultaneous rotation process of the whole spin structure. The different transition modes observed in the reference sample, i.e. negative coercivity and spin-flop, are caused by the interplay between the temperature dependent magnetization and anisotropy of $DyFe_2$ and YFe_2 [38]. At low temperature, both the magnetization and anisotropy of $DyFe_2$ are dominant over those for YFe_2, so the Zeeman energy and the anisotropy energy work together to provide the stabilizing force for $DyFe_2$. In this case, exchange springs form in the soft phase. If the composition of the superlattce is soft dominant, a negative coercivity will result. At high temperature, the crystalline anisotropy of $DyFe_2$ decreases so rapidly that the magneto-elastic anisotropy becomes significant. In addition to that, the magnetization of $DyFe_2$ varies more rapidly than that of YFe_2 with respect to temperature. Actually, at room temperature their magnetization values are almost equal. Hence, for a soft dominant superlattice sample in an applied, large magnetic field, it is now the soft phase that is parallel to the field, instead of the hard phase as at low temperature. The increased ratio of magnetization between YFe_2 and $DyFe_2$ and the increased importance of the magneto-elastic anisotropy for $DyFe_2$ are the main causes. The resulted configuration gives to the observed spin-flop transition at high field.

To demonstrate exchange spring collapse more clearly, we have investigated the sample [$DyFe_2$ 40 Å/YFe_2 80 Å/$DyFe_2$ 8 Å/YFe_2 80 Å] × 20. In contrast to the reference sample, at temperatures lower than 100 K, irreversibility caused by the increased anisotropy in the soft phase is observable for field applied along the $[00\bar{1}]$ direction. The irreversibility at room temperature for field along $[\bar{1}10]$ is also observed, where the spin-flop transition persists. For hysteresis loops measured along $[\bar{1}10]$ at low temperature, additional irreversible character can be verified by minor loops, as can be expected. Irreversible exchange springs are present in two other samples, one with a thinner hard layer in the middle of soft layers and the other being an alloy sample.

The OOMMF simulations provide insight into the different switching modes responsible for varied hysteretic characters. The negative coercivity is always due to the soft exchange spring unwinding, which results in a negative magnetization value at zero applied field, due to the soft-dominant structure of samples. The spin-flop transition at room temperature is a result of the increased magneto-elastic contribution to the

anisotropy, which favors a perpendicular configuration between the hard and the soft phases. In addition, for the exchange spring collapse samples, OOMMF simulation reveals that the main effect of the hard inclusion or doping in the soft phase is to increase the effective anisotropy of the soft phase, as intended. The observed and theoretically predicted irreversible behaviour agree well, displaying the usefulness of a simple 1D model of a chain of spins to model exchange spring systems.

Chapter 6

Summary

Nano-technology was first proposed by Feynman almost half a decade ago. Now after nearly 50 years development, it has begun to step into many areas of our everyday life. By way of contrast, magnetism is a very different phenomenon. It has been known to mankind for thousands of years and magnetic materials now have many applications in modern industry. The combination of both the nano-technology and magnetism offers the auspicious prospect of improvements and opportunities [109, 110], particularly in the development of novel devices, such as magnetic read heads.

In the pursuit of high energy permanent magnets, Kneller and Hawig [1] initiated the idea of exchange spring magnets, composed of alternating hard and soft magnetic layers coupled ferromagnetically. Subsequently, it was shown that antiferromagnetically coupled exchange spring systems could provide a solution to the superparamagnetic limit in information storage technology. Our molecular beam epitaxy grown $DyFe_2/YFe_2$ superlattice samples serve as a good model system to study antiferromagnetically coupled exchange spring physics, providing insight both to fundamental physics and application. Previous studies have demonstrated many novel features, such as domain wall giant magnetoresistance and negative coercivity, in $DyFe_2/YFe_2$ superlattices. Thus providing the prospect for potential applications in spintronics. However, all earlier discussions have been based on the concept of ideal exchange springs, i.e. the hard component is infinitely hard and the soft counterpart is infinitely soft. Within this paradigm, the exchange spring winding or unwinding is always reversible. However, it should be expected that this feature of exchange spring formation is not always true. In this thesis, non-ideal exchange spring behaviour has been highlighted, in the hope of offering more insight into the magnetization process of realistic exchange springs. To this end, a multilayered exchange spring structure, composed of antiferromagnetically coupled alternating $DyFe_2$ (hard) and YFe_2 (soft) layers, each with a characteristic thickness of the order of a few nanometers, was adopted.

Magneto-optic Kerr effect (MOKE) is sensitive to surface magnetism, given the finite penetration depth of light in magnetic materials. So it is an ideal technique for characterization of magnetic nano-structures. It manifests itself as a change in polarization for polarized light reflected from a ferromagnetic material. To first order, the change is proportional to the net magnetization, so it can be used to characterize the magnetization process. MOKE is more suitable for the observation of exchange springs, which are not uniformly distributed through the whole sample and tend to nucleate from the topmost soft layer. However, the MOKE setup used in this work is limited by the fact that it can only operate at room temperature and the maximal field available is only about 0.35 T. So for large field or low temperature measurements, a vibrating sample magnetometer (VSM) was used instead.

The first deviation from the ideal spring behaviour was then observed using MOKE. The effect was traced to a decrease in the anisotropy of the hard layer, due to an elevated temperature of 300 K. Room temperature MOKE measurements were performed on two soft dominant 1:4 superlattice samples, which showed reversible exchange spring winding for fields below ~ 0.2 T. VSM measurements at 300 K on one of the two samples confirmed the MOKE results. In addition, 1D computer simulations were employed to obtain further understanding on the switching process, by numerically solving the Landau-Lifshitz-Gilbert equation. Using reasonable parameters, the simulated MOKE loops agree qualitatively with the experimental ones. Contradictory to the conventional picture, computer simulation showed that the remanent state is antiparallel to that in the ideal case, even though the spring is still formed in the soft phase. On increasing the magnitude of the applied negative field, it is the soft phase, instead of the hard phase as in the ideal case, which opposes the coercive field. Consequently, as a result of this change of switching mode, the well established $1/t_s^2$ law for the bending field is not obeyed. The change of switching mode can be traced back to a change in the pinning mechanism: at low temperature, the exchange springs are pinned by the hard magnetic layers through the large magnetic anisotropy, whereas at high temperature, the pinning is provided by the Zeeman energy and the anisotropy at large fields and small fields, respectively. The $1/t_s^2$ law is valid for the case of exchange springs pinned by the hard layer anisotropy, so the transition from the low temperature switching mode to the high temperature one will violate the $1/t_s^2$ law for the bending field.

Further studies of non-ideal spring behaviours were obtained using $DyFe_2/YFe_2$ superlattices, with an additional thin layer of $DyFe_2$ inserted into the middle of the soft YFe_2 layers. The inclusion of $DyFe_2$ results in an effective increase in the YFe_2 anisotropy. Due to the induced anisotropy in the soft phase, the exchange spring unwinding should be irreversible.

Before investigating the sought-after irreversible exchange spring behaviour, a standard 1:4 soft dominant sample, serving as a reference sample, was characterized using a VSM at various temperatures from 10 K to 300 K. For field along the $[00\bar{1}]$ axis, hysteresis loops below $\sim$ 100 K show typical easy axis character, with negative coercivity. The hysteresis loops at temperatures $>$ 100 K confirm that $[00\bar{1}]$ is the hard axis. However, what is more interesting is the response of the 1:4 sample to magnetic fields applied along the $[\bar{1}10]$ (hard-in-plane-axis). For temperatures below $\sim$ 100 K, the resultant magnetic loops looked almost identical to those obtained with fields applied along a $[00\bar{1}]$ easy axis. Loops with a negative coercivity were still obtained, despite a different magnetization reversal process. At still higher temperatures, a spin-flop transition was identified. To understand these phenomena, OOMMF simulations were employed. As can be expected, for those loops showing negative coercivity, exchange springs unwind first in the soft phase. However, for the spin-flop like loops, the hard phase first switches from a perpendicular configuration to a antiparallel configuration with respect to the applied field, while the soft phase remains parallel to the applied field. The qualitative agreement between simulation and experiment is good. The OOMMF simulations confirm that the transition of switching mode is mainly responsible for the deviation from the $1/t_s^2$ law for the bending field, as observed earlier. The formation of exchange springs is reversible, except for a small irreversibility in hysteresis at 300 K, with field along $[\bar{1}10]$. This small irreversibility can be attributed to a small anisotropy in the soft phase, in addition to domain wall pinning.

It should be emphasized that both experiment and simulation demonstrate that the two directions, $[00\bar{1}]$ and $[\bar{1}10]$, are similar at low temperatures. Both directions are characterized by negative coercivity, which is due to the unwinding of exchange springs in the soft layers for soft-dominant superlattices. This similarity between $[00\bar{1}]$ and $[\bar{1}10]$ is understandable from the low temperature energy surfaces for $DyFe_2$. Actually, $[\bar{1}10]$ is a metastable direction at low temperatures. In addition, another important feature of $[\bar{1}10]$ high temperature exchange spring formation is that the nucleation tends to start in the top soft layers of the whole stack of hard/soft bilayers, as shown by the simulation. In small fields, exchange springs only penetrate about 2 bilayers from the top surface of the whole structure.

For the sample with 8 Å hard $DyFe_2$ inclusion in the soft YFe_2 phase, additional irreversibility was observed for both axes at low temperature. For field along $[00\bar{1}]$, there are even two irreversible exchange springs present in the whole demagnetization process measured by VSM. OOMMF simulations show that the induced anisotropy in the soft phase gives rise to the observed irreversibility. As compared to the reference sample at 380 K with field along $[\bar{1}10]$, a small additional small jump was observed in

the simulated loops, which can be attributed to an increase in the soft-phase anisotropy. Similar behaviour was confirmed in two additional samples, one with a thinner (4 Å) $DyFe_2$ inclusion and the other being an alloy sample. Qualitatively, the consequence of changing from 8 Å $DyFe_2$ inclusion to 4 Å $DyFe_2$ inclusion is a reduced degree of irreversibility, due to the less $DyFe_2$ inserted. In the alloy sample, the soft YFe_2 layers are doped uniformly with $DyFe_2$, resulting in an increased anisotropy. Irreversible exchange springs were still observable, but the degree of irreversibility was further decreased. OOMMF simulations give the same qualitative behaviour. The reduced effect of uniform doping on introducing irreversible exchange springs, as compared to local pinning through insertion of a thin $DyFe_2$ layer in the middle of soft layers, is understandable based on the consideration of exchange energy cost.

Appendix A

Temperature dependent parameters

The temperature dependent parameters needed in OOMMF simulation will be given below, from 100 K to 400 K in 10 K steps. The temperature dependence of magnetization is given in terms of the ratio $r = M(T)/M_0$, as measured from Mössbauer spectrum measurements [16]. M_0 is the zero temperature saturation magnetization, which is

$$8(\mu_{Dy} - 2\mu_{Fe})/a^3$$

for $DyFe_2$. Here $\mu_{Dy} = 10\mu_B$ and $\mu_{Fe} = 1.5\mu_B$ [24] are the magnetic moments of Dy and Fe in $DyFe_2$, respectively. μ_B denotes the Bohr magneton. $a = 7.325$ Å is the lattice constant of $DyFe_2$ [11]. The prefactor 8 reflects the fact that there are 8 Dy atoms in a unit cell. The same formulation is also valid for YFe_2. The only difference is that now the moment of YFe_2 is almost completely determined by the moment of Fe atoms, with Y being nonmagnetic except for a small induced 4d moment [111]. The relevant lattice constant for YFe_2 is $a = 7.363$ Å [11]. The values given for the multipolar anisotropy constants $\tilde{A}_l$ are calculated using the single-ion model for $DyFe_2$ [22, 26]. Those values are given in terms of temperature (K) per formula unit in the table. But the usual unit used in OOMMF simulation is J/m^3. Bearing in mind that there are 8 formula units in a unit cell, the conversion between those two units is very simple

$$\tilde{K}_l = 8k_B\tilde{A}_l/a^3$$

with k_B as the Boltzmann constant. The multipolar anisotropy constants $\tilde{K}_l$ are then related to the usual anisotropy coefficients through Eq. 1.10. The anisotropy and the magneto-elastic terms of YFe_2 are negligible, and are taken as 1/100 of those values for $DyFe_2$ given here, in the OOMMF simulation. This simplification results in temperature dependent easy directions, as in $DyFe_2$, which is contrary to the actual temperature-independent easy axis for YFe_2. But due to the small anisotropy and

magneto-elastic interaction constants for YFe_2 used in the simulation, changing to the actual easy axis $[\bar{1}11]$ does not change the hysteretic loops qualitatively.

T(K)	$r(YFe_2)$	$r(DyFe_2)$	$\tilde{A}_4$(K)	$\tilde{A}_6$(K)	$\tilde{A}_8$(K)	$\tilde{A}_2$(K)	$\tilde{A}_{242}$(K)
100	0.98	0.92	-29.53	-1.08	0.77	4.97	-0.58
110	0.98	0.91	-25.87	-0.86	0.55	4.76	-0.53
120	0.98	0.89	-22.64	-0.68	0.39	4.57	-0.49
130	0.98	0.88	-19.79	-0.54	0.28	4.37	-0.45
140	0.97	0.87	-17.30	-0.43	0.20	4.18	-0.41
150	0.97	0.85	-15.13	-0.34	0.15	4.00	-0.38
160	0.97	0.84	-13.23	-0.27	0.11	3.82	-0.35
170	0.96	0.83	-11.57	-0.22	0.08	3.64	-0.32
180	0.96	0.81	-10.13	-0.18	0.06	3.48	-0.29
190	0.96	0.80	-8.87	-0.14	0.04	3.31	-0.27
200	0.95	0.78	-7.77	-0.12	0.03	3.16	-0.25
210	0.95	0.77	-6.82	-0.09	0.02	3.00	-0.22
220	0.94	0.75	-5.98	-0.08	0.02	2.86	-0.21
230	0.94	0.74	-5.25	-0.06	0.01	2.72	-0.19
240	0.93	0.72	-4.61	-0.05	0.01	2.58	-0.17
250	0.93	0.71	-4.05	-0.04	0.01	2.45	-0.16
260	0.92	0.69	-3.56	-0.03	0.01	2.33	-0.15
270	0.92	0.68	-3.13	-0.03	0.00	2.21	-0.14
280	0.91	0.66	-2.75	-0.02	0.00	2.09	-0.12
290	0.90	0.65	-2.42	-0.02	0.00	1.99	-0.11
300	0.90	0.64	-2.13	-0.02	0.00	1.88	-0.10
310	0.89	0.62	-1.87	-0.01	0.00	1.78	-0.10
320	0.88	0.61	-1.65	-0.01	0.00	1.68	-0.09
330	0.87	0.59	-1.45	-0.01	0.00	1.59	-0.08
340	0.86	0.58	-1.27	-0.01	0.00	1.50	-0.07
350	0.85	0.56	-1.11	-0.01	0.00	1.42	-0.07
360	0.84	0.55	-0.98	-0.00	0.00	1.34	-0.06
370	0.83	0.53	-0.85	-0.00	0.00	1.26	-0.06
380	0.82	0.52	-0.75	-0.00	0.00	1.19	-0.05
390	0.81	0.50	-0.65	-0.00	0.00	1.11	-0.05
400	0.80	0.49	-0.57	-0.00	0.00	1.05	-0.04

Table A.1: Temperature dependent parameters for $DyFe_2$ used in the OOMMF simulation.

Bibliography

[1] E.F. Kneller and R. Hawig. The exchang-spring magnet: A new material principle for permanent magnets. *IEEE Trans. Magn.*, 27:3588–3600, 1991.

[2] J.-M. L. Beaujour. *Engineering the magnetic properties of epitaxial RE-Fe_2 Laves phase alloy and multilayer films.* PhD thesis, University of Southampton, 2003.

[3] R. Skomski and J.M.D. Coey. Giant energy product in nanostructured two-phase magnets. *Phys. Rev. B*, 48:15812–15816, 1993.

[4] R. Skomski and J.M.D. Coey. Nucleation field and energy product of aligned two-phase magnets-progress towards the 1 MJ/m^3 magnet. *IEEE Trans. Magn.*, 29:2860–2862, 1993.

[5] E.E. Fullerton, J.S. Jiang, and S.D. Bader. Hard/soft magnetic heterostructures: model exchange-spring magnets. *J. Magn. Magn. Mater.*, 200:392–404, 1999.

[6] D. Suess, T. Schrefl, S. Fahler, M. Kirschner, G. Hrkac, F. Dorfbauer, and J. Fidler. Exchange spring media for perpendicular recording. *Appl. Phys. Lett.*, 87:012504, 2005.

[7] D. Suess, T. Schrefl, M. Kirschner, G. Hrkac, F. Dorfbauer, O. Ertl, and J.Fidler. Optimization of exchange spring perpendicular recording media. *IEEE Trans. Magn.*, 41:3166–3168, 2005.

[8] D. Suess. Micromagnetics of exchange spring media: Optimization and limits. *J. Magn. Magn. Mater.*, 308:183–197, 2007.

[9] J. Dean, M. A. Bashir, A. Goncharov, G. Hrkac, S. Bance, T. Schrefl, A. Cazacu, M. Gubbins, R. W. Lamberton, and D. Suess. Thermally induced adjacent track erasure in exchange spring media. *Appl. Phys. Lett.*, 92:142505, 2008.

[10] A. Baker, M. Billard, K. Brown, A. Goadsby, S. Green, C. Howard, S. Kodippili, A. Newton, X. Ning, M. Stead, L. Vallance, L. Zang, D. A. Allwood, M. T.

Bryan, and J. Dean. A study of hard:soft layer ratios and angular switching in exchange coupled media. *J. Appl. Phys.*, 106:053902, 2009.

[11] M.J. Bentall, R.C.C. Ward, E.J. Grier, and M.R. Wells. Structure of $DyFe_2/YFe_2$ laves phase superlattices grown by molecular beam epitaxy. *J. Phys.: Condens. Matter*, 15:6493–6512, 2003.

[12] K.H.J. Buschow and R.P. van Stapele. Magnetic properties of some cubic rare-earth-iron compounds of the type RFe_2 and $R_xY_{1-x}Fe_2$. *J. Appl. Phys.*, 41:4066–4069, 1970.

[13] K.H.J. Buschow. Intermetallic compounds of rare-earth and 3d transition metals. *Rep. Prog. Phys.*, 40:1179–1256, 1977.

[14] A.R. Wildes, J. Mayerb, and K. Theis-Bröhl. The growth and structure of epitaxial niobium on sapphire. *Thin Solid Films*, 401:7–34, 2001.

[15] V. Oderno, C. Dufour, K. Dumesnil, Ph. Mangin, and G. Marchal. Epitaxial growth of (110) $DyFe_2$, $TbFe_2$ and $Dy_{0.7}Tb_{0.3}Fe_2$ thin films by molecular beam epitaxy. *J. Cryst. Growth*, 165:175–178, 1996.

[16] G.J. Bowden, D.St.P. Bunbury, A.P. GuimarÀes, and R.E. Snyder. Mössbauer studies of the cubic Laves iron-rare-earth intermetallic compounds. *J. Phys. C: Solid State Phys.*, 1:1376–1387, 1968.

[17] E. Burzo. Paramagnetic behavior of some rare-earth cobalt compounds. *Phys. Rev. B*, 6:2882–2887, 1972.

[18] M. Sawicki, G.J. Bowden, P.A.J. de Groot, B.D. Rainford, J.M.L. Beaujour, R.C.C. Ward, and M.R. Wells. Engineering coercivity in epitaxially grown (110) films of $DyFe_2$–YFe_2 superlattices. *Appl. Phys. Lett.*, 77:573–575, 2000.

[19] J.-M.L. Beaujour, S.N. Gordeev, G.J. Bowden, P.A.J. de Groot, B.D. Rainford, R.C.C. Ward, and M.R. Wells. Negative coercivity in epitaxially grown (110) $DyFe_2/YFe_2$ superlattices. *Appl. Phys. Lett.*, 78:964–966, 2001.

[20] S.N. Gordeev, J.-M.L. Beaujour, G.J. Bowden, P.A.J. de Groot, R.C.C. Ward, M.R. Wells, and A.G.M. Jansen. Giant magnetoresistance by exchange springs in $DyFe_2/YFe_2$ superlattices. *Phys. Rev. Lett.*, 87:186808, 2001.

[21] C.H. Marrows. Spin-polarised currents and magnetic domain walls. *Adv. in Phys.*, 54:585–713, 2005.

[22] K.N. Martin, P.A.J. de Groot, B.D. Rainford, K. Wang, G.J. Bowden, J.P. Zimmermann, and H. Fangohr. Magnetic anisotropy in the cubic laves $REFe_2$ intermetallic compounds. *J. Phys.: Condens. Matter*, 18:459–478, 2006.

[23] U. Atzmony and M.P. Dariel. Nonmajor cubic symmetry axes of easy magnetization in rare-earth-iron laves compounds. *Phys. Rev. B*, 13:4006–4014, 1976.

[24] J. Zimmermann. *Micromagnetic simulations of magnetic exchange spring systems*. PhD thesis, University of Southampton, 2007.

[25] A. Mougin, C. Dufour, K. Dumesnil, N. Maloufi, Ph. Mangin, and G. Patrat. Strain in single-crystal RFe_2 (110) thin films (R=Y, Sm, Gd, Tb, $Dy_{0.7}Tb_{0.3}$,Dy, Er, Lu). *Phys. Rev. B*, 59:5950–5959, 1999.

[26] G.J. Bowden, P.A.J. de Groot, B.D. Rainford, K. Wang, K.N. Martin, J.P. Zimmermann, and H. Fangohr. Magnetic anisotropy terms in [110] mbe-grown $REFe_2$ films involving the strain term ϵ_{xy}. *J. Phys.: Condens. Matter*, 18:5861–5871, 2006.

[27] V. Oderno, C. Dufour, K. Dumesnil, Ph. Bauer, Ph. Mangin, and G. Marchal. Magnetic anisotropy in (110) epitaxial $DyFe_2$ laves phase. *Phys. Rev. B*, 54:R17375–R17378, 1996.

[28] A. Mougin, C. Dufour, K. Dumesnil, and Ph. Mangin. Strain-induced magnetic anisotropy in single-crystal RFe_2 (110) thin films (R=Dy, Er, Tb, $Dy_{0.7}Tb_{0.3}$, Sm, Y). *Phys. Rev. B*, 62:9517–9531, 2000.

[29] G.J. Bowden, A.A. Zhukov, J.-M.L. Beaujour, J.D. O'Neill, B.D. Rainford, P.A.J. de Groot, R.C.C. Ward, M.R. Wells, and H. Küpfer. Field-dependent easy magnetic axes in epitaxially grown (110) $DyFe_2$ film. *J. Magn. Magn. Mater.*, 272-276:E1591–E1592, 2004.

[30] A.A. Zhukov, G.J. Bowden, J.-M.L. Beaujour, B.D. Rainford, P.A.J. de Groot, R.C.C. Ward, M.R. Wells, and H. Küpfer. Vector magnetometer studies of the easy magnetisation direction in epitaxially grown $DyFe_2$ film. *J. Magn. Magn. Mater.*, 270:312 – 320, 2004.

[31] D. Craik. *Magnetism: principles and applications*. John Wiley & Sons, Chichester, 1995.

[32] H.B. Callen and T.A. Welton. Irreversibility and generalized noise. *Phys. Rev.*, 83:34–40, 1951.

[33] Z. Li and S. Zhang. Thermally assisted magnetization reversal in the presence of a spin-transfer torque. *Phys. Rev. B*, 69:134416, 2004.

[34] J. Foros, A. Brataas, Y. Tserkovnyak, and G.E.W. Bauer. Current-induced noise and damping in nonuniform ferromagnets. *Phys. Rev. B*, 78:140402, 2008.

[35] R.A. Duine and C.M. Smith. Creep of current-driven domain-wall lines: Effects of intrinsic versus extrinsic pinning. *Phys. Rev. B*, 77:094434, 2008.

[36] W.F. Brown. Thermal fluctuations of a single-domain particle. *Phys. Rev.*, 130:1677–1686, 1963.

[37] J.L. García-Palacios and F.J. Lázaro. Langevin-dynamics study of the dynamical properties of small magnetic particles. *Phys. Rev. B*, 58:14937–14958, 1998.

[38] J.P. Zimmermann, G. Bordignon, R.P. Boardman, T. Fischbacher, H. Fangohr, K.N. Martin, G.J. Bowden, A.A. Zhukov, and P.A.J. de Groot. Micromagnetic simulation of the magnetic exchange spring system $DyFe_2/YFe_2$. *J. Appl. Phys.*, 99:08B904, 2006.

[39] M.J. Donahue and D.G. Porter. Oommf user's guide, version 1.0. Interagency Report NISTIR 6376. Technical report, National Institute of Standards and Technology, 1999.

[40] M. Sawicki, G.J. Bowden, P.A.J. de Groot, B.D. Rainford, J.-M.L. Beaujour, R.C.C. Ward, and M.R. Wells. Exchange springs in antiferromagnetically coupled $DyFe_2$-YFe_2 superlattices. *Phys. Rev. B*, 62:5817–5820, 2000.

[41] E.R. Moog and S.D. Bader. Smoke signals from ferromagnetic monolayers: p(1×1) Fe/Au (100). *Superlattices Microstruct.*, 1:543 – 552, 1985.

[42] S.D. Bader, E.R. Moog, and P. Grünberg. Magnetic hysteresis of epitaxially-deposited iron in the monolayer range: A Kerr effect experiment in surface magnetism. *J. Magn. Magn. Mater.*, 53:L295 – L298, 1986.

[43] P. Vavassori, R.M. Osgood III, M. Grimsditch, U. Welp, G. Crabtree, W. Fan, S.R.J. Brueck, B. Ilic, and P.J. Hesketh. Magnetic information in the light diffracted by a negative dot array of Fe. *Phys. Rev. B*, 59:6337–6343, 1999.

[44] T. Schmitte, K. Westerholt, and H. Zabel. Magneto-optical Kerr effect in the diffracted light of Fe gratings. *J. Appl. Phys.*, 92:4524–4530, 2002.

[45] T. Schmitte, A. Westphalen, K. Theis-Bröhl, and H. Zabel. The Bragg-MOKE: magnetic domains in Fourier space. *Superlattices Microstruct.*, 34:127–136, 1999.

[46] W.G. Stirling and M.J. Cooper. X-ray magnetic scattering. *J. Magn. Magn. Mater.*, 200:755–773, 1999.

[47] J.B. Kortright, D.D. Awschalom, J. Stöhr, S.D. Bader, Y.U. Idzerda, S.S.P. Parkin, I. K. Schuller, and H.-C. Siegmann. Research frontiers in magnetic materials at soft X-ray synchrotron radiation facilities. *J. Magn. Magn. Mater.*, 207:7–44, 1999.

[48] M.R. Freeman and J.F. Smyth. Picosecond time-resolved magnetization dynamics of thin-film heads. *J. Appl. Phys.*, 79:5898–5900, 1996.

[49] A.Y. Elezzabi, M.R. Freeman, and M. Johnson. Direct measurement of the conduction electron spin-lattice relaxation time t_1 in gold. *Phys. Rev. Lett.*, 77:3220–3223, 1996.

[50] K.H. Bennemann. Theory for nonlinear magnetooptics in metals. *J. Magn. Magn. Mater.*, 200:679–705, 1999.

[51] T.M. Crawford, C.T. Rogers, T.J. Silva, and Y.K. Kim. Observation of the transverse second-harmonic magneto-optic Kerr effect from $Ni_{81}Fe_{19}$ thin film structures. *Appl. Phys. Lett.*, 68:1573–1575, 1996.

[52] T.M. Crawford, T.J. Silva, C.W. Teplin, and C.T. Rogers. Subnanosecond magnetization dynamics measured by the second-harmonic magneto-optic Kerr effect. *Appl. Phys. Lett.*, 74:3386–3388, 1999.

[53] V. Talghader, M.T. Kief, and G. Al-Jumaily. On the use of x-ray reflectivity and the second-harmonic magneto-optic Kerr effect for characterizing buried magnetic interfaces. *J. Appl. Phys.*, 85:4586–4588, 1999.

[54] A.V. Kimel, A. Kirilyuk, P.A. Usachev, R.V. Pisarev, A.M. Balbashov, and Th. Rasing. Ultrafast non-thermal control of magnetization by instantaneous photomagnetic pulses. *Nature*, 435:655–657, 2005.

[55] M.I. Kurkin, N.B. Bakulina, and R.V. Pisarev. Transient inverse Faraday effect and ultrafast optical switching of magnetization. *Phys. Rev. B*, 78:134430, 2008.

[56] S.R. Woodford. Conservation of angular momentum and the inverse Faraday effect. *Phys. Rev. B*, 79:212412, 2009.

[57] K. Vahaplar, A.M. Kalashnikova, A.V. Kimel, D. Hinzke, U. Nowak, R. Chantrell, A. Tsukamoto, A. Itoh, A. Kirilyuk, and Th. Rasing. Ultrafast path for optical magnetization reversal via a strongly nonequilibrium state. *Phys. Rev. Lett.*, 103:117201, 2009.

[58] G. Malinowski, F.D. Longa, J.H.H. Rietjens, P.V. Paluskar, R. Huijink, H.J.M. Swagten, and B. Koopmans. Control of speed and efficiency of ultrafast demagnetization by direct transfer of spin angular momentum. *Nature Phys.*, 4:855–858, 2008.

[59] A.V. Sokolov. *Optical properties of metals*. Blackie and Son Ltd., London and Glasgow, 1967.

[60] P.N. Argyres. Theory of the Faraday and Kerr effects in ferromagnetics. *Phys. Rev.*, 97:334–345, 1955.

[61] L.M. Roth. Theory of the Faraday effect in solids. *Phys. Rev.*, 133:A542–A553, 1964.

[62] H.S. Bennett and E.A. Stern. Faraday effect in solids. *Phys. Rev.*, 137:A448 – A461, 1965.

[63] T. Huhne and H. Ebert. Fully relativistic descritption of the magneto-optical properties of arbitrary layered systems. *Phys. Rev. B*, 60:12982–12989, 1999.

[64] V.N. Antonov, A.N. Yaresko, A. Ya. Perlov, V.V. Nemoshkalenko, P.M. Oppeneer, and H. Eschrig. Magneto-optical spectroscopy of d- and f-ferromagnetic materials: recent theoretical progress. *Low Temp. Phys.*, 25:387–406, 1999.

[65] A. Perlov, S. Chadov, and H. Ebert. Green function approach for the *ab initio* calculation of the optical and magneto-optical properties of solids: Accouting for dynamical many-body effects. *Phys. Rev. B*, 68:245112, 2003.

[66] Z.Q. Qiu and S.D. Bader. Surface magneto-optic Kerr effect. *Rev. Sci. Instrum.*, 71:1243–1255, 2000.

[67] J. Zak, E.R. Moog, C. Liu, and S.D. Bader. Universal approach to magneto-optics. *J. Magn. Magn. Mater.*, 89:107–123, 1990.

[68] J. Zak, E.R. Moog, C. Liu, and S.D. Bader. Fundamental magneto-optics. *J. Appl. Phys.*, 68:4203–4207, 1990.

[69] Z.J. Yang and M.R. Scheinfein. Combined three-axis surface magneto-optical Kerr effects in the study of surface and ultrathin-film magnetism. *J. Appl. Phys.*, 74:6810–6823, 1993.

[70] D.A. Allwood, G. Xiong, M.D. Cooke, and R.P. Cowburn. Magneto-optical Kerr effect analysis of magnetic nanostructures. *J. Phys. D: Appl. Phys.*, 36:2175–2182, 2003.

[71] E.P. Wohlfarth and K.H.J. Buschow. *Ferromagnetic materials: a handbook on the properties of magnetically ordered substances*, volume 4. North Holland Publishing Company, Amsterdam, 1988.

[72] P. Horowitz and W. Hill. *The art of electronics*. Cambridge University Press, Cambridge, 1980.

[73] H.E. Edens. *Construction and characterization of a magneto-optical Kerr-effect instrument for studies of ferromagnetic GdFe films*. Master thesis, University of Amsterdam, 2002.

[74] J.M. Florczak and E.D. Dahlberg. Detecting two magnetization components by the magneto-optical Kerr effect. *J. Appl. Phys.*, 67:7520–7525, 1990.

[75] H.F. Ding, S. Pütter, H.P. Oepen, and J. Kirschner. Experimental method for separating longitudinal and polar Kerr signals. *J. Magn. Magn. Mater.*, 212:5 – 11, 2000.

[76] S. Foner. Versatile and sensitive vibrating-sample magnetometer. *Rev. Sci. Instr.*, 30:548–557, 1959.

[77] J. Mallinson. Magnetometer coils and reciprocity. *J. Appl. Phys.*, 37:2514–2515, 1966.

[78] A. Zieba and S. Foner. Detection coil, sensitivity function, and sample geometry effects for vibrating sample magnetometers. *Rev. Sci. Instrum.*, 53:1344–1354, 1982.

[79] M. Springford, J.R. Stockton, and W.R. Wampler. A vibrating sample magnetometer for use with a superconducting magnet. *J. Phys. E: Sci. Instrum.*, 4:1036–1040, 1971.

[80] G.J. Bowden. Detection coil systems for vibrating sample magnetometers. *J. Phys. E: Sci. Instrum.*, 5:1115–1119, 1972.

[81] S. Foner. Sensitivity of vibrating sample magnetometers–and how to increase sensitivity if needed. *Rev. Sci. Instrum.*, 45:1181–1183, 1974.

[82] S. Foner. Further improvements in vibrating sample magnetometer sensitivity. *Rev. Sci. Instrum.*, 46:1425–1426, 1975.

[83] K. Mibu, T. Nagahama, and T. Shinjo. Reversible magnetization process and magnetoresistance of soft-magnetic (NiFe)/hard-magnetic (CoSm) bilayers. *J. Magn. Mang. Mater.*, 163:75–79, 1996.

[84] S. Wüchner, J.C. Toussaint, and J. Voiron. Magnetic properties of exchange-coupled trilayers of amorphous rare-earth-cobalt alloys. *Phys. Rev. B*, 55:11576–11585, 1997.

[85] E.E. Fullerton, J.S. Jiang, M. Grimsditch, C.H. Sowers, and S.D. Bader. Exchange-spring behavior in epitaxial hard/soft magnetic bilayers. *Phys. Rev. B*, 58:12193–12200, 1998.

[86] R.J. Astalos and R.E. Camley. Magnetic permeability for exchange-spring magnets: Application to Fe/Sm-Co. *Phys. Rev. B*, 58:8646–8653, 1998.

[87] M. Grimsditch, R. Camley, E.E. Fullerton, S. Jiang, S.D. Bader, and C.H. Sowers. Exchange-spring systems: Coupling of hard and soft ferromagnets as measured by magnetization and brillouin light scattering (invited). *J. Appl. Phys.*, 85:5901–5904, 1999.

[88] E. Goto, N. Hayashi, T. Miyashita, and K. Nakagawa. Magnetizaton and switching characteristics of composite thin magnetic films. *J. Appl. Phys.*, 36:2951–2958, 1965.

[89] G. Asti, M. Solzi, M. Ghidini, and F.M. Neri. Micromagnetic analysis of exchange-coupled hard-soft planar nanocomposites. *Phys. Rev. B*, 69:174401, 2004.

[90] K. Yu. Guslienko, O. Chubykalo-Fesenko, O. Mryasov, R. Chantrell, and D. Weller. Magnetization reversal via perpendicular exchange spring in FePt/FeRh bilayer films. *Phys. Rev. B*, 70:104405, 2004.

[91] G. Asti, M. Ghidini, C. Pernechele R. Pellicelli, M. Solzi, F. Albertini, F. Casoli, S. Fabbrici, and L. Pareti. Magnetic phase diagram and demagnetization processes in perpendicular exchange-spring multilayers. *Phys. Rev. B*, 73:094406, 2006.

[92] R.C. O'Handley. Magnetization process. In *Modern magnetic materials: Principles and applications*, chapter 9. John Wiley & Sons, Inc., 2000.

[93] S. Nieber and H. Kronmller. Nucleation fields in periodic multilayers. *Phys. Stat. Sol. B*, 153:367–375, 1989.

[94] R. Skomski. Nucleation in inhomogeneous permanent magnets. *Phys. Stat. Sol. B*, 174:K77–K80, 1992.

[95] R.J. Lange, I.R. Fisher, P.C. Canfield, V.P. Antropov, S.J. Lee, B.N. Harmon, and D.W. Lynch. Observation of a metamagnetic phase transition in an itinerant $4f$ system via the magneto-optic Kerr effect: $Ce(Fe_{1-x}Co_x)_2$. *Phys. Rev. B*, 62:7084–7092, 2000.

[96] E. Hairer, S.P. Norsett, and G. Wanner. *Solving ordinary differential equations*. Springer series in computational mathematics, Springer-Verlag, 1987.

[97] G.J. Bowden, J.M.L. Beaujour, S. Gordeev, P.A.J. de Groot, B.D. Rainford, and M. Sawicki. Discrete exchange-springs in magnetic multilayer samples. *J. Phys.: Condens. Matter*, 12:9335–9346, 2000.

[98] V. Sokalski, D.E. Laughlin, and J.-G. Zhu. Experimental modeling of intergranular exchange coupling for perpendicular thin film media. *Appl. Phys. Lett.*, 95:102507, 2009.

[99] G. Guo, G. Zhang, S. Song, D.W. Wang, G.J. Bowden, and P.A.J. de Groot. Irreversible magnetic exchange-spring processes in antiferromagnetic exchange-coupled bilayer systems. *Appl. Phys. Lett.*, 93:102505, 2008.

[100] M. Abramowitz and I. A. Stegun. *Handbook of mathematical functions*. National Bureau of Standards, 10th edition, 1972.

[101] A. Hubert and R. Schäfer. *Magnetic domains: the analysis of magnetic microstructures*. Springer, Berlin, 1998.

[102] K. Dumesnil, C. Dufour, Ph. Mangin, F. Wilhelm, and A. Rogalev. Thermal dependence of magnetic springs location in a $DyFe_2/YFe_2$ superlattice. *J. Appl. Phys.*, 95:6843–6845, 2004.

[103] K. Dumesnil, C. Dufour, Ph. Mangin, A. Rogalev, and F. Wilhelm. Temperature dependence in the magnetization reversal process of $DyFe_2/YFe_2$ exchange-coupled superlattices. *J. Phys.: Condens. Matter*, 17:L215–L222, 2005.

[104] M.R. Fitzsimmons, S. Park, K. Dumesnil, C. Dufour, R. Pynn, J.A. Borchers, J.J. Rhyne, and Ph. Mangin. Vector magnetization depth profile of a Laves-phase exchange-coupled superlattice obtained using a combined approach of micromagnetic simulation and neutron reflectometry. *Phys. Rev. B*, 73:134413, 2006.

[105] D.L. Mills. Surface spin-flop state in a simple antiferromagnet. *Phys. Rev. Lett.*, 20:18–21, 1968.

[106] F. Keffer and H. Chow. Dynamics of the antiferromagnetic spin-flop transition. *Phys. Rev. Lett.*, 31:1061–1063, 1973.

[107] S.G.E. te Velthuis, J.S. Jiang, S.D. Bader, and G.P. Felcher. Spin flop transition in a finite antiferromagnetic superlattice: Evolution of the magnetic structure. *Phys. Rev. Lett.*, 89:127203, 2002.

[108] G.J. Bowden, K.N. Martin, A. Fox, B.D. Rainford, R.C.C. Ward, and P.A.J. de Groot. The effect of inter-layer diffusion on magnetic exchange spring behaviour. *J. Phys.: Condens. Matter*, 20:125223, 2008.

[109] G. Srajer, L.H. Lewis, S.D. Bader, A.J. Epstein, C.S. Fadley, E.E. Fullerton, A. Hoffmann, J.B. Kortright, K.M. Krishnan, S.A. Majetich, T.S. Rahman, C.A. Ross, M.B. Salamon, I.K. Schuller, T.C. Schulthess, and J.Z. Sun. Advances in nanomagnetism via x-ray techniques. *J. Magn. Magn. Mater.*, 307:1–31, 2006.

[110] S.D. Bader. Colloquium: Opportunities in nanomagnetism. *Rev. Mod. Phys.*, 78:1–15, 2006.

[111] R. Coehoorn. Calculated electronic structure and magnetic properties of Y-Fe compounds. *Phys. Rev. B*, 39:13072–13085, 1989.